Springer Theses
Recognizing Outstanding Ph.D. Research

Manabu Moritsu

Search for the Pentaquark Θ^+ via the $\pi^- p \longrightarrow K^- X$ Reaction at J-PARC

Springer

Springer Theses

Recognizing Outstanding Ph.D. Research

Aims and Scope

The series "Springer Theses" brings together a selection of the very best Ph.D. theses from around the world and across the physical sciences. Nominated and endorsed by two recognized specialists, each published volume has been selected for its scientific excellence and the high impact of its contents for the pertinent field of research. For greater accessibility to non-specialists, the published versions include an extended introduction, as well as a foreword by the student's supervisor explaining the special relevance of the work for the field. As a whole, the series will provide a valuable resource both for newcomers to the research fields described, and for other scientists seeking detailed background information on special questions. Finally, it provides an accredited documentation of the valuable contributions made by today's younger generation of scientists.

Theses are accepted into the series by invited nomination only and must fulfill all of the following criteria

- They must be written in good English.
- The topic should fall within the confines of Chemistry, Physics, Earth Sciences, Engineering and related interdisciplinary fields such as Materials, Nanoscience, Chemical Engineering, Complex Systems and Biophysics.
- The work reported in the thesis must represent a significant scientific advance.
- If the thesis includes previously published material, permission to reproduce this must be gained from the respective copyright holder.
- They must have been examined and passed during the 12 months prior to nomination.
- Each thesis should include a foreword by the supervisor outlining the significance of its content.
- The theses should have a clearly defined structure including an introduction accessible to scientists not expert in that particular field.

More information about this series at http://www.springer.com/series/8790

Manabu Moritsu

Search for the Pentaquark Θ^+ via the $\pi^- p \to K^- X$ Reaction at J-PARC

Doctoral Thesis accepted by
Kyoto University, Kyoto, Japan

Springer

Author
Dr. Manabu Moritsu
Department of Physics
Kyoto University
Kyoto
Japan

Supervisor
Prof. Tomofumi Nagae
Department of Physics
Kyoto University
Kyoto
Japan

ISSN 2190-5053 ISSN 2190-5061 (electronic)
Springer Theses
ISBN 978-981-10-0010-2 ISBN 978-981-10-0012-6 (eBook)
DOI 10.1007/978-981-10-0012-6

Library of Congress Control Number: 2015960816

Printed on acid-free paper

This Springer imprint is published by SpringerNature
The registered company is Springer Science+Business Media Singapore Pte Ltd.

Parts of this thesis have been published in the following journal article:

M. Moritsu *et al.* (J-PARC E19 Collaboration), "High-resolution search for the Θ^+ pentaquark via a pion-induced reaction at J-PARC", Phys. Rev. C **90**, 035205 (2014).

Supervisor's Foreword

There are no particular physics laws to prohibit the existence of exotic hadrons; they are quark many-body systems other than baryons (qqq) and mesons ($q\bar{q}$). Pentaquark particles ($qqqq\bar{q}$), tetraquark particles ($qq\bar{q}\bar{q}$), and dibaryons ($qqqqqq$) are such examples. Quantum chromodynamics (QCD) requires only that the systems should be colorless. A pentaquark particle Θ^+ was first claimed to exist at a mass of about 1540 MeV/c^2 with a narrow width of several MeV or less by the SPring-8/LEPS Collaboration in 2003. Soon after that, there followed many experimental reports supporting its existence. However, many negative results were later reported in various reactions. At this moment, the experimental situation on the Θ^+ is still controversial. On the other hand there is increasing evidence for the existence of tetraquark states observed in charmonium-like and bottomonium-like particles at B-Factories and other facilities. As for the Θ^+, therefore, a high-statistics and high-resolution experiment is definitely needed.

As the first physics data-taking experiment at the hadron experimental hall of J-PARC, we set up the SKS spectrometer system at the new K1.8 beam line in order to search for the Θ^+ with the best energy resolution of 2.13 MeV (FWHM). The differential cross sections of the $\pi^- p \to K^- X$ reaction at two incident momenta of 1.92 GeV/c and 2.01 GeV/c have been measured in the forward directions between 2 and 15° in the laboratory system. The two measurements at two incident momenta were separated in two periods because of the big earthquake in the east part of Japan in March 2011.

In this thesis by Manabu Moritsu, the details of the data analyses in the second data taking at 2.01 GeV/c in 2012 is described. There were several improvements in the analysis methods compared with that in the first data analysis. Further, Manabu Moritsu carried out a combined analysis of the two data sets to draw a conclusion from the experiment.

A high-intensity pion beam with a typical intensity of 1.7×10^6 for the 6s beam cycle was incident on a liquid hydrogen target of 0.85 g/cm^2. The beam momentum was analyzed with a beam line spectrometer in the last part of the K1.8 beam line. The outgoing kaons were measured with the SKS spectrometer with a momentum

resolution of 2×10^{-3} (FWHM). The relative momentum between the two spectrometers was calibrated with beam-through data and the charged Σ hyperon production in the $\pi^{\pm} p \to K^{+} \Sigma^{\pm}$ reactions. With the elaborative work by Manabu Moritsu, the absolute missing-mass energy scale was calibrated with an uncertainty of 1.4 MeV/c^2, and the missing-mass resolution for the Θ^{+} production was estimated to be 2.13 ± 0.15 MeV (FWHM). Thus, if the Θ^{+} were produced, a clear peak as narrow as 2 MeV should be observed at the right mass. There was no sharp peak observed in the missing-mass spectrum. The upper limit of the Θ^{+} production cross section in the forward angles was obtained to be less than 0.28 μb/sr at the 90 % C.L. in the mass region of 1500–1560 MeV/c^2, which is as small as the value obtained in the first data taking at 1.92 GeV/c in 2010.

With help of a theoretical calculation by Hyodo et al using the effective Lagrangian approach, the upper limit of the Θ^{+} width was estimated as a function of the Θ^{+} mass by fitting two data sets with one common parameter. The theoretical model uncertainties were considered as much as possible. It was found that the width should be less than 0.36 and 1.9 MeV for the Θ^{+} spin-parity of $1/2^{+}$ and $1/2^{-}$, respectively. As for the upper limit of the width for the case of $1/2^{+}$, it is more stringent than the so-far best upper limit of 0.64 MeV reported from the Belle Collaboration. Although it is still comparable to the width of 0.34 ± 0.10 MeV reported from the DIANA Collaboration, this limit set the significant tighter limit which is a remarkable achievement in this field of exotic hadron searches obtained by Manabu Moritsu in this thesis.

Kyoto
June 2015

Prof. Tomofumi Nagae

Acknowledgments

I would like to express my sincere gratitude to my supervisor, Prof. Tomofumi Nagae. He guided me to an exciting world of experimental hadronic physics. He always encouraged me and provided me with invaluable experience in detector development and experiments at many places. I learned the proper attitude of physicists from him.

I am deeply indebted to Prof. Megumi Naruki, who is the spokesperson of the J-PARC E19 experiment. She gave me an opportunity to join the experiment and write this doctoral thesis.

I would like to express my thanks to Dr. Masayuki Niiyama and Dr. Hiroyuki Fujioka for useful discussions and advice. They often helped me when I was in trouble. I was deeply impressed with their sharp insight into analysis and physics.

I would like to address my thanks to all the members of the J-PARC E19 Collaboration. In particular, I am grateful to Dr. Kotaro Shirotori and Dr. Tomonori Takahashi, who are my colleagues from the construction phase of the K1.8 experimental area. They always led me and gave me a lot of advice. I acknowledge Mr. S. Adachi, Mr. H. Ekawa, Mr. S. Hayakawa, Dr. R. Honda, Mr. Y. Ichikawa, Ms. R. Iwasaki, Mr. S. Kanatsuki, Dr. R. Kiuchi, Ms. M. Sato, Dr. H. Sugimura, Dr. M. Ukai, Mr. T.O. Yamamoto, Mr. S.B. Yang, and Mr. Y. Yonemoto for their outstanding efforts in construction of the experimental setup. I spent an enjoyable time at J-PARC, thanks to their warm hospitality. Dr. K. Miwa, Prof. A. Sakaguchi, Prof. T. Takahashi, and Prof. K. Tanida gave me helpful advice based on their profound knowledge and experience. I also acknowledge Dr. M. Agnello, Dr. K. Aoki, Prof. B. Bassalleck, Dr. E. Botta, Dr. S. Bufalino, Dr. A. Feliciello, Dr. K. Hosomi, Dr. Y. Igarashi, Prof. K. Imai, Mr. N. Ishibashi, Prof. S. Ishimoto, Prof. K. Itahashi, Dr. M.J. Kim, Prof. T. Koike, Prof. V.V. Kulikov, Prof. S. Marcello, Mr. Y. Matsumoto, Mr. K. Matsuoka, Prof. H. Noumi, Mr. Y. Nozawa, Mr. R. Ota, Dr. S. Suzuki, Prof. H. Takahashi, Prof. H. Tamura, Mr. T. Tanaka, Dr. A.O. Tokiyasu, Ms. N. Tomida, Mr. K. Yagi, and Mr. K. Yoshida. The experiment could not have been carried out without their great contributions. It is my great pleasure to have worked with them.

I would like to express my thanks to Dr. Tetsuo Hyodo for helpful discussions about the experimental results from a theoretical point of view. He kindly provided us a theoretical calculation without which we could not have extracted the constraint of the width.

I would like to thank members of the Experimental Nuclear and Hadronic Physics Laboratory, Kyoto University. I love the spirit of academic freedom. I was happy to spend my graduate-school life in this laboratory.

Last but not least, I express my deep appreciation to my parents for their continuous support and encouragement.

Manabu Moritsu

Contents

Chapter 1
Introduction to Pentaquark Search

1.1 Pentaquark Θ^+

The strong interaction is described by quantum chromodynamics (QCD) as the fundamental theory. It has been tested quantitatively in hundreds of experiments at high-momentum transfer, where asymptotic freedom justifies the use of perturbation theory. Hadrons are clearly bound states of quarks held together by gluon-mediated interactions. However, we still fail to put our hands on a quantitative and predictive theory of confined states of quarks and gluons. Hadron spectroscopy is a laboratory in which our understanding of the low-energy dynamics of quarks and gluons is tested.

The concept of "quark" as a fundamental particle was advocated just 50 years ago [1]. Since then, the constituent quark model is very successful in classification of light baryons and mesons consisting of u, d, and s quarks. Mesons are assigned to quark-antiquark pairs ($q\bar{q}$), and baryons are assigned to three-quark configurations (qqq). In particular, the lowest baryon configuration gives two irreducible representations of the flavor SU(3) symmetry: spin-1/2 octet **8** and spin-3/2 decuplet **10**. It is reminded that the constituent quark model is a phenomenological model and not derived from the first principle of QCD; therefore, the existence of exotic states beyond its classification is not precluded. QCD requires only that hadrons are formed in color singlet and does not limit the number of quarks. Multiquark hadrons, interpreted as the configurations of more than three quarks, e.g., "tetraquark ($qq\bar{q}\bar{q}$)", "pentaquark ($qqqq\bar{q}$)", and "dibaryon ($qqqqqq$)", have been discussed ever since the appearance of the quark model [2–5].

In the past decade, many charmonium-like and bottomonium-like resonances, so called X, Y, and Z, have been observed in the B-factories and many other experiments [6]. They are difficult to fit in the conventional quark model, and thus are considered as candidates of exotic hadrons, such as tetraquarks, meson molecules, and hybrid states. Since most of these states are experimentally established, there is no doubt that exotics do exist at least in the heavy flavor sector.

Pentaquarks are defined as particles with a valence structure of four quarks and one antiquark. In a naive sense, since a pentaquark decays into a three-quark baryon and a

M. Moritsu, *Search for the Pentaquark Θ^+ via the $\pi^- p \to K^- X$ Reaction at J-PARC*, Springer Theses, DOI 10.1007/978-981-10-0012-6_1

quark-antiquark meson, it was expected to have a wide width [2, 5]; this would make the experimental observation difficult. After decades, however, a possible existence of a pentaquark with a narrow width was suggested by Diakonov et al. in 1997 [7]. They predicted an exotic positive-strangeness baryon, later called Θ^+, having spin-parity $1/2^+$ and isospin 0, with a light mass of about 1530 MeV/c^2 and a width of less than 15 MeV. The narrow width is a great advantage for experiments to detect the Θ^+ with a good signal-to-noise ratio. The Θ^+ has a strangeness quantum number $S = +1$ with its minimal quark configuration of $uudd\bar{s}$; hence, it is manifestly exotic. The problem whether the pentaquark with such a light mass and a narrow width really exists (or not) could be a good testbed for the current understanding of hadron physics.

The first experimental evidence of the Θ^+ was reported in 2003 by the LEPS Collaboration [8]. A sharp resonance decaying into K^+n was observed in the $\gamma n \to K^+K^-n$ reaction on ^{12}C at a mass of 1540 ± 10 MeV/c^2 with a width smaller than 25 MeV. The resonance has a strangeness $+1$ and its mass and width are consistent with the Θ^+ predicted by Diakonov et al. Soon after the first evidence was presented, several experimental groups published supporting evidence for the Θ^+. The Θ^+ has received enthusiastic attention and numerous papers have been published [9, 10]. In a conference in 2003, Wilczek noted *"Although the discoveries are striking, I don't think they are so peculiar as to require introducing new interaction or modifying QCD…On the other hand these discoveries do offer us a golden opportunity to sharpen and expand our understanding of QCD itself"* [11]. However, the evidences were followed by a number of experiments with no evidence and the experimental situation became controversial.

In this thesis, a search for the Θ^+ pentaquark via the $\pi^- p \to K^- X$ reaction conducted at J-PARC is presented. In the subsequent sections, a discussion about the Θ^+ width based on K^+d scattering data is given in Sect. 1.2, followed by theoretical and experimental reviews in Sects. 1.3 and 1.4, respectively. The production mechanism of the Θ^+ via meson-induced reactions is discussed in Sect. 1.5, which is relevant to the present experiment. Finally, a goal and outline of the present experiment is described in Sect. 1.6.

1.2 Width of Θ^+ from K^+d Scattering Data

Since the pentaquark Θ^+ has the same quark contents as the combination of a K^+ meson together with a neutron, the K^+d scattering is the most straightforward way to search for the resonance. However, there is no clear evidence of the resonance in the region around 1540 MeV from past K^+d scattering data. A question why the Θ^+ was missed in the past experiments is raised. The answer to the question probably lies, at least partly, in the very small width of the Θ^+. If the step size of beam momenta was much sparser than the width, the existence of the Θ^+ might be passed over. Shortly after the experimental evidence for the Θ^+ appeared, consistency of the Θ^+ with the

past K^+d scattering data was discussed vigorously in connection with the width of the Θ^+. Here, study in this direction is reviewed.

The K^+N scatterings such as K^+p and K^+d scattering were measured mostly with bubble chambers in the 1960s and 1970s. Assuming that the mass of the Θ^+ is 1540 MeV, the momentum of K^+ on the resonance in the K^+n scattering is 440 MeV/c. Such a low momentum K^+ beam was provided by degrading an initial beam of higher momenta. The resulting beam energy can have significant momentum spread of typically 6 % (FWHM). Because there is no neutron target, the isospin $I = 0$ amplitude must be extracted from the K^+d scattering data, containing a mixture of $I = 0$ and $I = 1$ amplitudes. This can be done only after correcting the data for the Fermi motion of the target nucleons and the momentum spread of the K^+ beam. Owing to the difficulty of treatment of these unfolding procedures, there was disagreement between the cross sections measured in different experiments. Hence, one must be careful when drawing any conclusions from the past database of K^+d scattering.

One of the first discussion using the past K^+d scattering data was made by Nussinov [12]. If the Θ^+ is narrow, it could escape detection if there is a gap in the database at the resonant energy, but the deuteron Fermi motion will spread it out so that it should be noticeable. Using these estimates and a cursory examination of the database, he concludes that the width of the Θ^+ must be less than 6 MeV for $I = 0$ and $J^P = 1/2^+$.

Arndt, Strakovsky, and Workman reanalyzed the existing K^+N data based on the phase shift analysis focusing on the energy region around 1540 MeV [13]. They checked the change of χ^2 in fitting the database associated with additional resonances in the s, p and d waves with some widths. They conclude that the Θ^+ widths beyond the few-MeV level are excluded.

Haidenbauer and Krein examined the K^+N elastic cross section and the phase shift in $I = 0$ and $J^P = 1/2^+$ partial wave using the Jülich KN meson-exchange model [14]. They conclude that there is no way to reconcile the existing KN cross section data with the existence of the Θ^+ with a width of 5 MeV or more. A similar method was applied to the $K^+d \to K^0pp$ reaction by Sibirtsev et al. [15]. They conclude that the Θ^+ width is constrained to be less than 1 MeV.

Cahn and Trilling illustrated the extraction of the Θ^+ width from the charge exchange reaction cross section [16]. They deduced the width $\Gamma = 0.9 \pm 0.3$ MeV from the DIANA result reported in 2003 [17]. They also estimated the upper limit of the width of 1–4 MeV from the past K^+d data.

Gibbs [18] showed a possible existence of a narrow resonance using the K^+d total cross section data measured by Bowen et al. [19]. On the basis of a weak scattering approximation, and taking account of the Fermi motion in the deuteron, the total cross section was calculated with a resonance with an assumed width and mass. An experimental bump structure was well reproduced by the assumption of a resonance at 1559 ± 3 MeV with a width of 0.9 ± 0.3 MeV for the $J^P = 1/2^+$ case, as shown in Fig. 1.1.

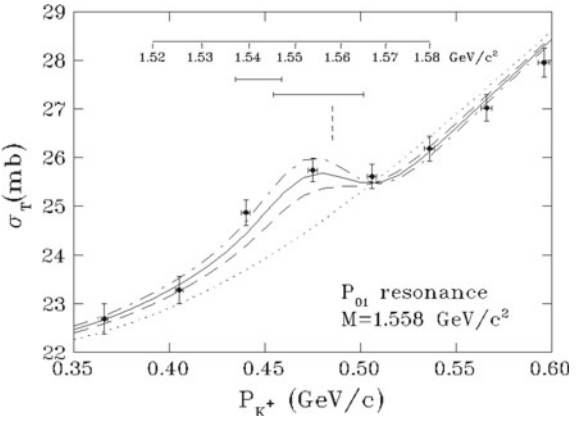

Fig. 1.1 Total cross section of K^+d scattering measured by Bowen et al. [19], together with the fitting results by Gibbs [18] using a weak scattering approximation for a p-wave resonance. The *dashed-dotted*, *solid*, and *dashed curves* correspond to widths of 1.2, 0.9, and 0.6 MeV, respectively. The *dotted curve* is the background fit

As reviewed above, according to the reanalyses of the K^+d scattering data, there is a consensus that the width should be less than a few MeV, if the Θ^+ exists. The width is quite narrower than those of ordinary strongly decaying hadrons, and the narrowness is peculiar to the Θ^+.

1.3 Theoretical Works

Theoretical studies for the Θ^+ pentaquark are introduced in this section. A point of the discussion is whether the pentaquark with a light mass and a narrow width could be explained theoretically, i.e., what structure the pentaquark has. Since the structure of a hadron is often reflect in its parity as well as spin, which parity and spin theoretical models predict is also interesting.

1.3.1 Naive Insight into the Narrowness of Θ^+

The narrow width of the Θ^+ is a challenge for any theoretical interpretation. Since the mass of Θ^+ is about 100 MeV above the KN threshold, the Θ^+ decays into KN (pK^0 or nK^+) by the strong interaction. The Θ^+ is unique in that its valence quark configuration ($uudd\bar{s}$) already contains all the quarks needed for the decay into KN. Non-exotic hadrons can only couple to their decay channels by creating quark pairs; e.g., $\Lambda(1520) \to \bar{K}N$ needs creating a $u\bar{u}$ or $d\bar{d}$ pair. The suppression of quark pair creation, known as the OZI rule, is often invoked as an explanation for narrow widths. For the narrowness of Θ^+, some other unknown mechanism would have to be responsible.

1.3.2 Conventional Quark Model

The constituent quark model is the most traditional way to understand hadron properties. Since quarks have positive parity and antiquarks have negative parity, ground states of pentaquarks without orbital excitation would have negative parity: namely, $1/2^-$. Although the quark model contains some variations, in a naive quark model approach, $1/2^-$ pentaquark states give the lowest mass. Haung, Zhang, Yu, and Zou calculated the Θ^+ mass in the chiral SU(3) quark model, and found it 200–300 MeV higher than the experimental value [20]. Furthermore, it is obviously difficult for the $1/2^-$ state to realize the narrow width of Θ^+ (without any novel mechanism) because it decays into $K(0^-)$ and $N(1/2^+)$ in s wave.

1.3.3 Chiral Soliton Model

The first prediction of the light and narrow pentaquark was provided using the chiral soliton model by Diakonov, Petrov, and Polyakov in 1997 [7]. The model was briefly reviewed in [21]. The chiral soliton model is a model of baryons based on the large-N_c (number of color) limit. The "soliton" is another word for the self-consistent pion field in the nucleon in which quarks move. Baryons are regarded as rotational states in the ordinary space and flavor SU(3) space. The baryon octet $(1/2^+)$ and decuplet $(3/2^+)$ states are well reproduced as the two lowest rotational states of the chiral solitons. The next lowest is the antidecuplet with $1/2^+$ as shown in Fig. 1.2, where the corners of the diagram are manifestly exotic. Diakonov et al. assumed the known nucleon resonance $N^*(1710, 1/2^+)$ a member of the antidecuplet, and estimated the properties of the other members. The positive strangeness exotic baryon, later called Θ^+, was predicted at a mass of about 1530 MeV with a width of 15 MeV or less. In their model, the narrowness follows from a cancellation of different contributions in the decay operator.

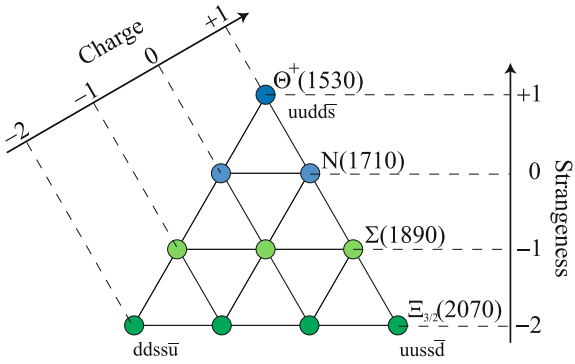

Fig. 1.2 Antidecuplet of baryons with $J^P = 1/2^+$ predicted by Diakonov et al. using the chiral soliton model [7]. The corners of this diagram are manifestly exotic: Θ^+, $\Xi^+_{3/2}$, $\Xi^{--}_{3/2}$. Their quark content and the predicted masses are shown

1.3.4 Diquark Correlation

The models that are often called "correlated quark models" are a kind of extended quark models introducing specific inter-quark correlations, called "diquark" correlations. Various effective quark interactions as well as phenomenological analyses predict the strong correlation between quarks [22]; i.e., the color antitriplet $\bar{\mathbf{3}}_c$, flavor antitriplet $\bar{\mathbf{3}}_f$, and spin singlet with even parity: $[qq]^{\bar{3}_c \bar{3}_f 0^+}$. This channel is favored by one-gluon exchange.

Jaffe and Wilczek proposed a $[ud][ud]\bar{s}$ picture, where two ud diquarks are coupled with an $\bar{s}$ antiquark [23]. To satisfy the total color singlet, two diquarks must combine into $\mathbf{3}_c$, which is the antisymmetric part of $\bar{\mathbf{3}}_c \otimes \bar{\mathbf{3}}_c$; therefore, the space wave function of the two diquarks must be antisymmetric, i.e., negative space parity; the two diquarks must have a relative angular momentum $L = 1$ at least. Combining with $\bar{s}$, the Θ^+ spin-parity of $1/2^+$ was predicted.

Karliner and Lipkin proposed a diquark-triquark model giving a $[ud][ud\bar{s}]$ picture, where a ud diquark are coupled with a $ud\bar{s}$ triquark in a relative p wave [24]. The $ud\bar{s}$ triquark belongs to $\mathbf{3}_c$, where the ud spins are parallel and each one is antiparallel to the $\bar{s}$ antiquark. They also predicted the Θ^+ spin-parity of $1/2^+$.

In both the models above, the spin-parity of $1/2^+$ with finite relative angular momentum was predicted, which is significantly different from the naive quark model prediction of $1/2^-$. Furthermore, in their pictures, the initial and final states in the $\Theta^+ \to KN$ decay have different configurations in terms of the color, spin, and space; i.e., the overlap of the wave function between the initial and final states is small. They suggested that the narrow width might be explained with the rearrangement of the color, spin, and spatial wave functions.

1.3.5 Lattice QCD Calculation

If pentaquarks exist, such states must emerge directly from the first principle, QCD; practically through lattice QCD calculation. It is not so easy to deal with pentaquarks rather than usual baryons or mesons in lattice QCD, because the $qqqq\bar{q}$ state can be decomposed into qqq and $q\bar{q}$ even in the quenched approximation, in which quark pair creations and annihilations do not occur. Since the Θ^+ mass is slightly above the threshold of KN, the presence of the KN scattering state complicates the exploration of the Θ^+ pentaquark (see Ref. [25] for an early review). Several lattice calculations were published to search for the Θ^+ in the quenched approximation. Some positive signals were reported whereas negative results were also reported. The results are summarized in Table 1.1. Notice that the positive results tend to favor the spin-parity $1/2^-$, which is against either predictions from the chiral soliton model or the diquark approach. However, the results are diverging and seem to be inconclusive so far.

Table 1.1 Summary of the results from the lattice QCD calculations searching for the Θ^+

Author(s)	Signal	Spin-parity	Ref(s).
Csikor et al.	Yes→No	~~$1/2^+$~~, $1/2^- \rightarrow$ ~~$1/2^-$~~	[26, 27]
Sasaki	Yes	~~$1/2^+$~~, $1/2^-$	[28]
Chiu-Hsieh	Yes	$1/2^+$, ~~$1/2^-$~~	[29]
Mathur et al.	No	~~$1/2^+$~~, ~~$1/2^-$~~	[30]
Ishii et al.	No	~~$1/2^+$~~, ~~$1/2^-$~~, ~~$3/2^+$~~, ~~$3/2^-$~~	[31, 32]
Lasscock et al.	No/Yes	~~$1/2^+$~~, ~~$1/2^-$~~, $3/2^+$, ~~$3/2^-$~~	[33, 34]
Takahashi et al.	Yes	~~$1/2^+$~~, $1/2^-$	[35]
Alexandrou-Tsapalis	(Yes)	~~$1/2^+$~~, $(1/2^-)$	[36]
Holland-Juge	No	~~$1/2^-$~~	[37]

The third column shows the examined spin-parities, which are lined in the case of no signal obtained

1.4 Experimental Review

After the fist evidence of Θ^+ was presented, considerable numbers of experimental results were published. The experimental status of the Θ^+ has a complicated history with vicissitudes. One can find experimental and historical reviews by Hicks in Refs. [9, 10] and by Danilov and Mizuk in Ref. [38], and also reviews of Particle Data Group, written by Trilling in 2004 [39] and 2006 [40], and by Wohl in 2008 [41], after which no update is given. Here, I review the experiments classifying them under the production processes.

1.4.1 Low-Energy Photoproduction Experiments

The photoproduction of the Θ^+ has been intensively studied by the LEPS, SAPHIR and CLAS Collaborations using photon beams around 1–5 GeV, as summarized in Table 1.2. Most of the experiments used the photoproduction on a neuron or proton, i.e., $\gamma n \rightarrow K^- \Theta^+$, or $\gamma p \rightarrow \bar{K}^0 \Theta^+$, where n stands for a neutron in a nucleus.

1.4.1.1 $\gamma n \rightarrow K^- \Theta^+$

The LEPS Collaboration reported the first experimental evidence for the Θ^+ in the γC $\rightarrow$ K^+K^-X reaction in 2003 [8]. A sharp peak was observed at a mass of 1540 $\pm$ 10 MeV with a width less than 25 MeV, which is compatible with the experimental resolution, as shown in Fig. 1.3 (top left). LEPS reported the further

Table 1.2 Summary of the photoproduction experiments for the Θ^+

Group	Reaction	Signal	Result		Ref(s).
			Mass	Width	
LEPS	$\gamma C \to K^+K^-X$	Yes	1540 ± 10	<25	[8]
SAPHIR	$\gamma p \to \bar{K}^0K^+n$	(Yes)[a]	$(1540 \pm 4 \pm 2)$	(<25)	[42]
CLAS	$\gamma d \to K^+K^-p\,n$	~~Yes~~ [b]	~~1542 ± 5~~	~~< 21~~	[43]
CLAS	$\gamma p \to \pi^+K^+K^-n$	Yes	1555 ± 10	<26	[44]
CLAS	$\gamma p \to \bar{K}^0K^+n/\bar{K}^0K^0p$	No	$\sigma<0.7$ nb		[45, 46]
CLAS	$\gamma d \to K^+K^-p\,n$	No	$\sigma_{\gamma n} < 3$ nb		[47]
CLAS	$\gamma d \to \Lambda K^+n$	No	$\sigma < 5$–25 nb		[48]
LEPS	$\gamma d \to K^+K^-p\,n$	Yes	$1524 \pm 2 + 3$	<26	[49]
Amaryan et al.	$\gamma p \to K^0_SK^0_Lp$	Yes	1543	<14	[50]

The forth column shows the experimental results for the mass and width in a unit of MeV in case of positive results, or the upper limit in case of negative results

[a]This SAPHIR result is inconsistent with the high-statistics CLAS result [45, 46] (see text)

[b]This earlier CLAS result was disproved by themselves with the 30 times higher statistics data [47]

evidence in the $\gamma d \to K^+K^-p\,n$ reaction with improved statistics in 2009 [49]. Since they detected only the K^+K^- pair at forward angles and expected a quasifree reaction on a neutron, a Fermi motion correction was necessary. Figure 1.3 (top right) shows the Fermi-motion-corrected nK^+ invariant mass spectrum, which shows a narrow peak at $1524 \pm 2 + 3$ MeV with a statistical significance of 5.1σ. The cross section of the $\gamma n \to K^-\Theta^+$ reaction was estimated to be 12 ± 2 nb/sr in the LEPS angular range.

An alternative interpretation for the LEPS result was proposed by Martínez Torres and Oset [51]. Using their theoretical model of the $\gamma d \to K^+K^-p\,n$ reaction without the Θ^+ production, they suggested that the analysis method used in the experiment, together with the chosen cut, might create an artificial broad peak in the nK^+ invariant mass spectrum, and claimed that the observed peak is compatible with a statistical fluctuation of the 2σ significance.

The CLAS Collaboration also searched for the Θ^+ in the $\gamma d \to K^+K^-p\,n$ reaction with high statistics data of 38 pb^{-1}, but observed no peak [47]. The upper limit of the cross section for the elementary $\gamma n \to K^-\Theta^+$ reaction was estimated to be 3 nb. In contrast to LEPS, since they required all the charged particles, K^+K^-p, the reaction is not a simple quasifree reaction but the rescattering of the spectator proton should be needed. Moreover, the discrepancy between the LEPS and CLAS results might be attributed to the different angular acceptances of these two experiments. The LEPS spectrometer has the acceptance of $\theta_{K^-} < 20°$, whereas the CLAS spectrometer has the acceptance of $\theta_{K^-} > 20°$. If the Θ^+ production cross section has a strong angular dependence peaked forward, there is still a room to explain the positive result of LEPS.

Recently, a preliminary result from the LEPS Collaboration with improved statistics of 2.6 times higher than the previous paper [49] was presented at a conference in 2012 [52]. The same analysis did not show a strong narrow peak and resulted in

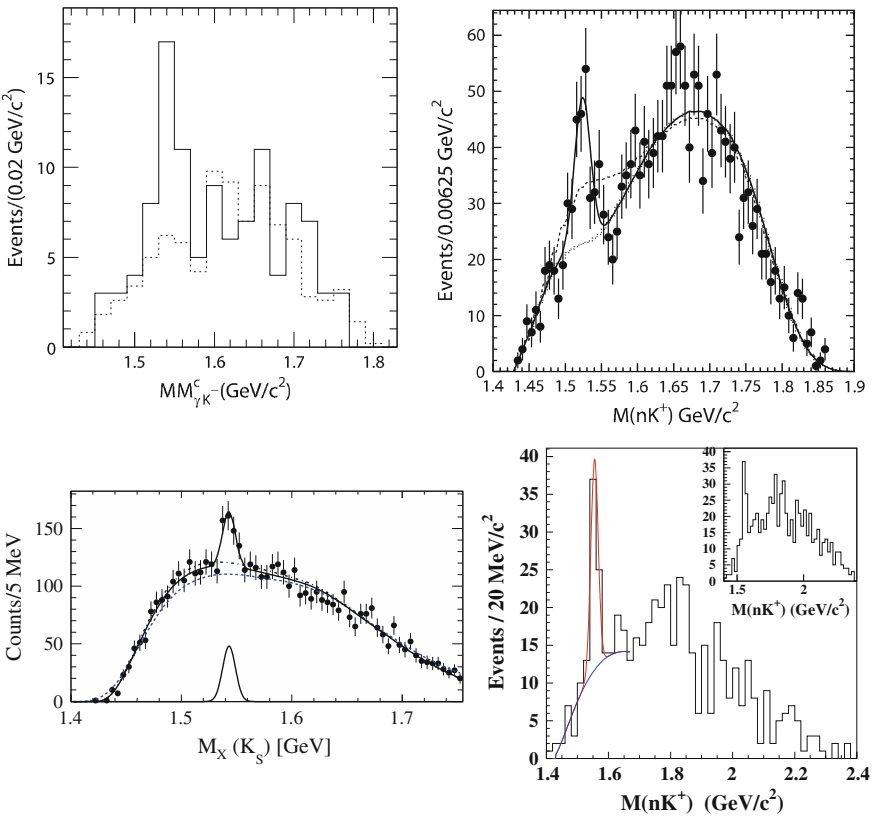

Fig. 1.3 Positive results from the photoproduction experiments. (*Top left*) Fermi-motion-corrected missing mass spectrum of the (γ, K^-) reaction for a signal sample (*solid line*) and events from LH_2 (*dotted line*) reported by the LEPS Collaboration in 2003 [8]. (*Top right*) Fermi-motion-corrected nK^+ invariant mass spectrum reported by the LEPS Collaboration in 2009 [49]. (*Bottom left*) (γ, K_S) missing mass spectrum obtained by Amaryan et al. with a cut $-t_\Theta < 0.45\,\mathrm{GeV}^2$, where t_Θ represents a four momentum transfer [50]. (*Bottom right*) nK^+ invariant mass spectrum in the $\gamma p \to \pi^+ K^+ K^- n$ reaction reported by the CLAS Collaboration in 2004 [44]. The *inset* shows a different cut condition

decrease of the significance. However, an enhancement still remained in data enriching the quasifree γn reaction on the basis of a new analysis. They continue data taking with an improved setup optimized for the analysis.

1.4.1.2 $\gamma p \to \bar{K}^0 \Theta^+$

The $\gamma p \to \bar{K}^0 \Theta^+$ reaction was studied by the SAPHIR [42] and CLAS [45, 46] Collaborations. There is an apparent contradiction in their results: SAPHIR found the evidence of the Θ^+ with the cross section of 300 nb [42],[1] whereas CLAS found

[1] The reanalysis of SAPHIR is found in [53] leading the same result.

no evidence using much higher statistics data of $70\,\mathrm{pb}^{-1}$ and estimated the cross section upper limit of 0.7 nb [46]. Because the quality of the CLAS data is much better than that of SAPHIR, it is hard to believe the result reported by the SAPHIR Collaboration.

The cross section difference between the $\gamma n \to K^- \Theta^+$ and $\gamma p \to \bar{K}^0 \Theta^+$ reactions was studied by Nam et al. using the effective Lagrangian method [54]. They suggested that the Θ^+ photoproduction from a proton could be strongly suppressed as compared with that from a neutron assuming the Θ^+ spin-parity of $3/2^{\pm}$, owing to a large contribution from the contact term of $\gamma \bar{K} N \Theta$, which exists only in the $\gamma n \to K^- \Theta^+$ reaction diagram. They remarked that the CLAS result [45, 46] does not immediately lead to the absence of Θ^+.

Recently, Amaryan et al. [50], a break-off group of the CLAS Collaboration, reported an observation of a narrow peak in the missing mass of K^0_S in the $\gamma p \to p K^0_S K^0_L$ reaction using the CLAS data, as shown in Fig. 1.3 (bottom left). Since the ϕ-meson photoproduction predominates in this photon energy, it was usually cut out by excluding the $K\bar{K}$ invariant mass near the ϕ mass; however, they did not apply the cut to utilize an interference effect. They claimed that the peak may be due to the interference between the Θ^+ and ϕ leading to the same final state. On the other hand, the CLAS Collaboration itself was not convinced of the evidence [55]. Their primary concern is the lack of justification for the kinematic cuts used in the analysis, without which the narrow peak does not appear. Amaryan et al. are indeed aware of the concern and remarked the necessity of additional data to understand the details of the interference.

1.4.1.3 Others

The CLAS Collaboration published the positive evidence for the Θ^+ in the $\gamma p \to \pi^+ K^+ K^- n$ reaction using a relatively higher energy photon beam of 3–5.47 GeV early in 2004, as shown in Fig. 1.3 (bottom right) [44]. They suggested that the reaction might be mediated through an N^* resonance decaying into $K^- \Theta^+$ around 2.4 GeV, such as $\gamma p \to \pi^+ N^* \to \pi^+ K^- \Theta^+$. Note that, although the other early CLAS results were later examined by the dedicated experiments with higher statistics data, the confirmation of this result by high statistics data has not been performed yet.

1.4.2 Formation Experiments

The formation reaction, $K^+ n \to \Theta^+$, which is a reverse reaction of the decay, is particularly important. In this reaction, the Θ^+ width can be derived from the cross section, as explained in [16]. The resonant cross section is determined entirely by the width of the resonance, Γ, and its branching ratios B_i and B_f into the initial and final channels according to the Breit-Wigner form:

$$\sigma(m) = B_i B_f \sigma_0 \left[\frac{\Gamma^2/4}{(m - m_0)^2 + \Gamma^2/4} \right], \tag{1.1}$$

where m_0 is the resonance mass, and

$$\sigma_0 \equiv \frac{2J+1}{(2s_1+1)(2s_2+1)} \frac{4\pi}{k^2} = 68\,\text{mb}, \tag{1.2}$$

where J is the spin of the resonance, s_1 and s_2 are the spins of incident particles, and k is the breakup momentum at the resonance rest frame. For the $K^+n \to \Theta^+$ reaction, σ_0 is 68 mb assuming that the Θ^+ mass is 1540 MeV and the spin $J = 1/2$. Then, the total cross section is calculated as

$$\sigma_{\text{tot}} = \int_{-\infty}^{\infty} \sigma(m) dm = \frac{\pi\Gamma}{2} B_i B_f \sigma_0 = (27\,\text{mb/MeV})\ \Gamma, \tag{1.3}$$

where $B_i = B_f = 1/2$, which is appropriate for either isospin $I = 0$ or 1, was used.

The $K^+n \to \Theta^+$ formation reaction was investigated by the DIANA and Belle Collaborations, as summarized in Table 1.3. Both groups searched for the Θ^+ as an intermediate resonance in the charge-exchange reaction $K^+n \to \Theta^+ \to K^0_S p$ on nuclei.

The DIANA Collaboration reanalyzed the 1970s xenon bubble chamber data irradiated by a 0.85-GeV/c K^+ beam, and found the evidence for the Θ^+ produced in the $K^+\text{Xe} \to K^0_S p\,\text{Xe}'$ reaction [17, 56]. They observed a narrow peak in the pK_S invariant mass spectrum at 1538 ± 2 MeV with a width consistent with the experimental resolution, as shown in Fig. 1.4 (left). The intrinsic width of the Θ^+ was estimated by comparing the signal magnitude with the level of nonresonant charge-exchange background under the peak. To obtain the original nonresonant background distribution prior to the rescattering of the K^0 and proton in nuclear medium, they used a Monte Carlo simulation using the intranuclear cascade medel. They assumed that the bulk of produced Θ^+ baryons decay upon leaving the Xe nucleus because of its possible width of 1 MeV or less. The Θ^+ width was estimated to be 0.34 ± 0.10 MeV, where the error does not include the systematic uncertainties of the simulation procedure. This is currently the only information about a finite experimental value for the Θ^+ width.

The Belle Collaboration also searched for the Θ^+ using kaon secondary interactions in the materials of the Belle detector [57]. The kaons produced in e^+e^- annihilation have quite low momenta peaking at 0.6 GeV/c. They found no evidence

Table 1.3 Summary of the formation experiments for the Θ^+

Group	Reaction	Signal	Result		Ref(s).
			(Mass)	(Width)	
DIANA	$K^+\text{Xe} \to K^0_S p\,\text{Xe}'$	Yes	1538 ± 2	0.34 ± 0.10	[17, 56]
Belle	$K^+A \to K^0_S pA'$	No		<0.64	[57]

The forth column shows the experimental results for the mass and width in a unit of MeV

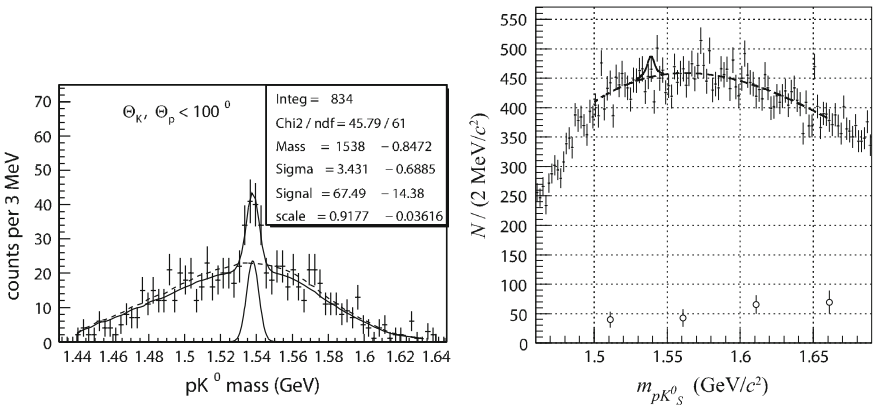

Fig. 1.4 Results of the DIANA and Belle experiments. (*Left*) pK_S invariant mass spectrum under a cut condition reported by the DIANA Collaboration [56]. (*Right*) Invariant mass spectrum for secondary pK_S^0 pairs reported by the Belle Collaboration [57]

in the pK_S invariant mass spectrum shown in Fig. 1.4 (right). In the same manner as DIANA, comparing with the nonresonant charge-exchange background yield, the upper limit of the Θ^+ width was estimated to be $\Gamma_\Theta < 0.64\,\text{MeV}$ at the 90 % C.L. at a mass of 1539 MeV. Note that the limit does not contradict the DIANA result.

1.4.3 Experiments Using High-Energy Beams

Following the low-energy experiments, many experimental results using high-energy beams, e.g., 10–100 GeV or much higher, were reported one after another. To begin with, the following three points should be noticed:

Fragmentation In the high-energy reaction in which quarks or partons rather than hadrons are involved, hadrons are produced in fragmentation or "string breaking" as the quark-antiquark separation. In order to form the Θ^+, there must be four quarks and one antiquark localized in space with small relative volocity. It seems to be unlikely to achieve such a situation in a naive sense. One should examine closely wheter the reaction is sensitive to the Θ^+ production from the viewpoint of the reaction mechanism.

Strangeness tag Almost all the following experiments in this subsection measured the pK_S^0 invariant mass spectra from inclusive production. Since the K_S^0 is not an eigenstate of flavors, one cannot distinguish the strangeness $S = +1$ or -1; therefore, the invariant mass spectra include both Σ^{*+} and possible Θ^+ peaks. Since there is no sharp Σ^* resonance established in 1500–1600 MeV [58], it is practically regarded as the Θ^+ if the sharp peak is observed.

Production ratio The production ratio of Θ^+ to $\Lambda(1520)$, R_{Λ^*}, is often used for an indicator of the cross section, because $\Lambda(1520)$ is narrow (15.6 MeV) and easily

Table 1.4 Summary of the Θ^+ search experiments using high-energy lepton beams or decay processes

Group	Reaction	Signal	Result	Ref.
νBC	$\nu A \to K^0_S p X$	Yes	$M = 1533 \pm 5\,\mathrm{MeV}$	[59]
HERMES	$e^+ d \to K^0_S p X$	Yes	$M = 1528 \pm 2.6 \pm 2.1\,\mathrm{MeV}$	[60]
ZEUS	$ep \to eK^0_S p X / eK^0_S \bar{p} X$	Yes	$M = 1521.5 \pm 1.5^{+2.8}_{-1.7}\,\mathrm{MeV}$	[61]
H1	$ep \to eK^0_S p X / eK^0_S \bar{p} X$	No	$\sigma < 30$–$90\,\mathrm{pb}$	[62]
BES	$e^+e^- \to J/\psi \to \Theta^+ \bar{\Theta}^-$	No[a]	$\mathcal{B} < 1.1 \times 10^{-5}$	[63]
ALEPH	$e^+e^- \to Z \to K^0_S p X$	No	$\mathcal{B} < 6.2 \times 10^{-4}$	[64]
DELPHI	$e^+e^- \to Z \to K^0_S p X$	No	$\mathcal{B} < 5.1 \times 10^{-4}$	[65]
BaBar	$e^+e^- \to q\bar{q}/\Upsilon(4S) \to K^0_S p X$	No	$\mathcal{B} < 5.0 \times 10^{-5} / 1.8 \times 10^{-4}$	[66]
Belle	$B^0 \to K^0_S p \bar{p}$	No	$\mathcal{B} < 2.3 \times 10^{-7}$	[67]
BaBar	$B^0 \to K^0_S p \bar{p}$	No	$\mathcal{B} < 2.0 \times 10^{-7}$	[68]
L3	$\gamma^*\gamma^* \to K^0_S p X / K^0_S \bar{p} X$	No	$\sigma < 1.8\,\mathrm{nb}$	[69]
FOCUS	$\gamma\mathrm{BeO} \to K^0_S p X / K^0_S \bar{p} X$	No	$R_{\Sigma^*} < 2.3\,\%$	[70]
NOMAD	$\nu A \to K^0_S p X$	No	$<2.13 \times 10^{-3}/\nu$ interaction	[71]
BaBar	$e^{\pm}\mathrm{Be} \to K^0_S p X$	No	Not given	[72]

The forth column shows the experimental results. $\mathcal{B}$ denotes a branching ratio for a corresponding decay producing Θ^+

[a] Azimov and Strakovsky suggest that this reaction is not sensitive enough to produce the Θ^+ [73]

reconstructed, and the mass is close to that of the Θ^+. In the same manner, R_{Σ^*} is also defined as the production ratio of Θ^+ to $\Sigma(1385)$.

Table 1.4 shows a summary of the Θ^+ search experiments using high-energy lepton beams or decay processes.

In 2003, Asratyan et al., an ITEP group, analyzed past experimental data with big bubble chambers (νBC) irradiated by 30–140 GeV neutrino beams, and observed a peak in the invariant mass of the pK^0_S system at $1533 \pm 5\,\mathrm{MeV}$ [59]. Three years later, the NOMAD Collaboration reported no evidence in the νA interactions, and set an upper limit of the Θ^+ production rate as shown in Fig. 1.5 [71]. They claimed

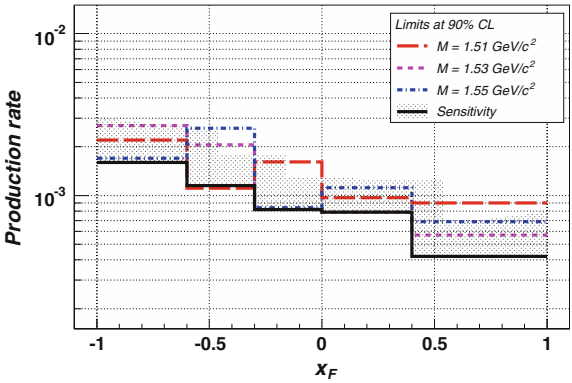

Fig. 1.5 Sensitivity and upper limits at 90 % C.L. for Θ^+ production rates in the νA interactions as a function of x_F, for masses of 1510, 1530, and 1550 MeV/c^2, reported by the NOMAD Collaboration [71]

that the production rate of $\sim 10^{-3}$ reported by Asratyan et al. is excluded for a large fraction of the x_F range, except for the region $x_F \approx -1$.

In 2004, the HERMES [60] and ZEUS [61] Collaborations reported the evidence of Θ^+ in the *ed* and *ep* collision data, respectively. It is noted that, in the ZEUS data, they required the momentum transfer $Q^2 > 20\,\mathrm{GeV}^2$, without which the peak was not observed; no justification is given on this criterion. Furthermore, the H1 Collaboration reported no evidence in the same reaction for either Q^2 region between 5 and $100\,\mathrm{GeV}^2$ [62]. Later, in 2007, the BaBar Collaboration presented the result obtained from the $e^{\pm}\mathrm{Be} \to K^0_S\, p\, X$ reaction using the events from the beam halo hitting the beryllium beampipe [72]. The obtained pK^0_S spectra were compared with the HERMES and ZEUS results in Fig. 1.6. The high-statistics of the BaBar result shows smooth spectra with no hint of a Θ^+ peak, and hence disagree with the previous two results. Note that the center-of-mass energy of 9.4 GeV and the Q^2 region ($\sim$0) of BaBar are almost the same as those of HERMES but different from those of ZEUS.

Table 1.5 shows a summary of the Θ^+ search experiments using high-energy hadron beams. The SVD Collaboration studied the $pA \to K^0_S\, p\, X$ reaction using a 70-GeV proton beam, and observed a peak at $M = 1523 \pm 2 \pm 3\,\mathrm{MeV}$ for a region

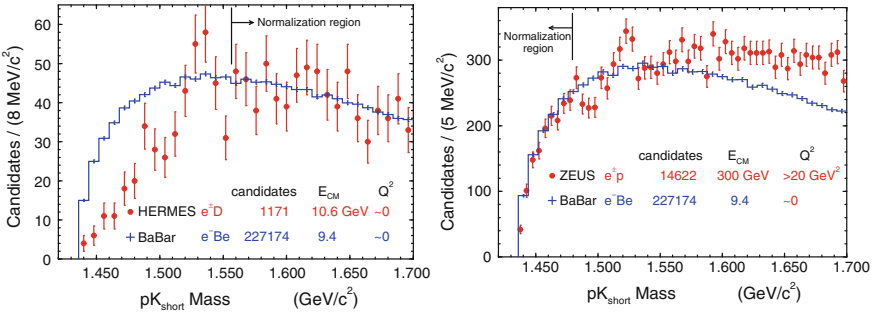

Fig. 1.6 (*Left*) The HERMES pK^0_S mass distribution [60] compared to the corresponding BaBar distribution [72] normalized to the HERMES data for the region above $1.58\,\mathrm{GeV}/c^2$. (*Right*) The ZEUS pK^0_S mass distribution [61] compared to the corresponding BaBar distribution [72] normalized to the ZEUS data for the region below $1.48\,\mathrm{GeV}/c^2$. Both figures are taken from [72]

Table 1.5 Summary of the Θ^+ search experiments using high-energy hadron beams

Group	Reaction	Signal	Result	Ref(s).
SVD	$pA \to K^0_S\, p\, X$	Yes	$M = 1523 \pm 2 \pm 3\,\mathrm{MeV}$	[74, 75]
SPHINX	$pA \to \bar{K}^0 NKA$	No	$R_{\Lambda^*} < 2\,\%$	[76]
HERA-B	$pA \to K^0_S\, p\, X$	No	$R_{\Lambda^*} < 2.7\,\%$	[77]
HyperCP	$p(\pi/K)\mathrm{Cu} \to K^0_S\, p\, X$	No	$<0.3\,\%/K^0_S p$ candidate	[78]
PHENIX	$d\mathrm{Au} \to K^- \bar{n} X$	No	Not given	[79]
CDF	$p\bar{p} \to K^0_S\, p\, X / K^0_S\, \bar{p}\, X$	No	$R_{\Lambda^*} < 3\,\%$	[80]
WA89	$\Sigma^- A \to K^0_S\, p\, X$	No	$<1.8\,\mu$b/nucleon	[81]

The forth column shows the experimental results

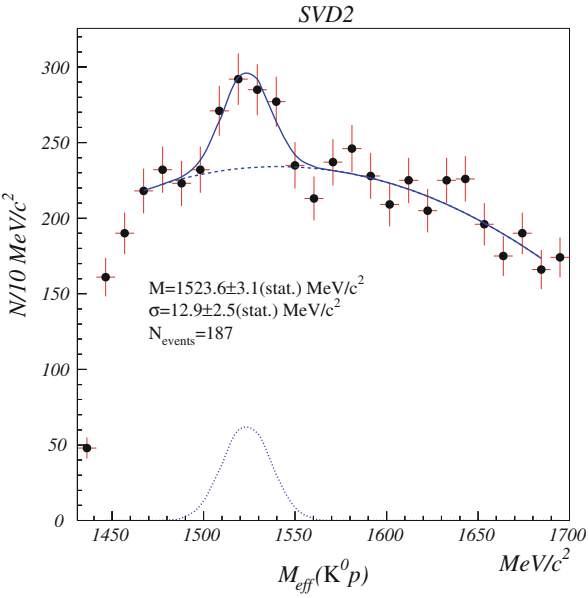

Fig. 1.7 pK_S^0 invariant mass spectrum for events with K_S^0 decaying outside a vertex detector, reported by the SVD Collaboration [75]

$x_F \geq 0$, as shown in Fig. 1.7 [75]. The SPHINX Collaboration also studied the $pA \to \bar{K}^0 NKA$ reaction using a 70-GeV proton beam, but found a null result [76]. It was claimed, however, that the Θ^+ was produced with very small x_F at SVD, whereas SPHINX has no acceptance in this region. Still, it is not clear how to reconcile the SVD positive result with the null result of the HERA-B Collaboration [77], which was obtained from the same reaction with the same acceptance of x_F but with a higher center-of-mass energy of 41.6 GeV instead of 11.5 GeV. The production ratio $R_{\Lambda^*} = 8$–$12\,\%$ estimated from the SVD result is in marked disagreement with the HERA-B upper limit, $R_{\Lambda^*} < 2.7\,\%$.

As described above, the production of Θ^+ may be suppressed in high-energy reactions. This was studied by Titov et al. [82] based on energy dependence of the Regge trajectories and the scaling behavior of the hadronic amplitudes. They found distinct decreasing of the Θ^+ production fraction in fragmentation at high energy, although there is no suppression in the central rapidity region in inclusive reactions. They suggested that the threshold region with the initial energy of a few GeV or less seems to be more favorable for the Θ^+ production.

1.4.4 Low-Energy Hadron-Induced Experiments

Experiments using low-energy hadron beams are a good probe to study the Θ^+. The hadron-induced cross section ought to be rather larger than the photoproduction. Furthermore, hadron-induced reactions are complementary to the photo-induced ones in

Table 1.6 Summary of the low-energy hadron-induced experiments for the Θ^+

Group	Reaction	Signal	Result	Ref.
COSY-TOF	$pp \to K^0_S\, p\, \Sigma^+$	~~Yes~~ [a]	~~$M = 1530 \pm 5$ MeV~~	[83]
COSY-TOF	$pp \to K^0_S\, p\, \Sigma^+$	No	$\sigma < 0.15\,\mu$b	[84]
COSY-ANKE	$pp \to \pi^+ K^0_S\, p\, \Lambda$	No	$\sigma < 58$ nb	[85]
KEK E522	$\pi^- p \to K^- X$	No	$\sigma < 1.8,\ 3.9\,\mu$b	[86]
KEK E559	$K^+ p \to \pi^+ X$	No	$d\sigma/d\Omega < 3.5\,\mu$b/sr	[87]

The forth column shows the experimental results

[a] This earlier COSY-TOF result was disproved by themselves with the 4–8 times higher statistics data [84]

terms of the Θ^+ production mechanism in the low energy region. Comparing various types of reactions, it is possible to discuss the Θ^+ properties through the reaction mechanism. The experimental aspect is described in this subsection, and interpretation of the results is given in Sect. 1.5. Table 1.6 shows a summary of the low-energy hadron-induced experiments. Since the KEK-PS E522 and E559 experiments are particularly related to the present experiment, they are reviewed in the following.

1.4.4.1 KEK-PS E522 Experiment

The E522 experiment [86] was performed to search for the Θ^+ via the $\pi^- p \to K^- X$ reaction with beam momenta of 1.87 and 1.92 GeV/c ($\sqrt{s} = 2.10$ and 2.12 GeV, respectively) at KEK-PS. Both the incident π^- and outgoing K^- were measured using the K2 beam line and the forward spectrometer, KURAMA. Since a scintillation fiber or a bulk polyethylene was used as a target, the missing mass spectra included the contribution from the carbon nuclei. No clear peak was found in the missing mass spectrum obtained at 1.87 GeV/c, while, in the spectrum obtained at 1.92 GeV/c, a bump was observed at 1530.6 MeV with a width compatible to the experimental resolution of 13.4 MeV (FWHM), as shown in Fig. 1.8 (left). The statistical significance of this bump, however, is only 2.5–2.7σ, which is not sufficient to claim the bump as the evidence of Θ^+. The upper limits of the differential cross section at scattering angles of 0–20° in the laboratory frame were estimated to be 1.6 and 2.9 μb/sr at the 90 % C.L. for the 1.87- and 1.92-GeV/c data, respectively. Assuming that Θ^+ is produced isotropically in the center-of-mass system, the upper limits of the total cross section were also estimated to be 1.8 and 3.9 μb at the 90 % C.L., respectively.

1.4.4.2 KEK-PS E559 Experiment

The E559 experiment [87] was performed to search for the Θ^+ via the $K^+ p \to \pi^+ X$ reaction with a beam momentum of 1.2 GeV/c ($\sqrt{s} = 1.89$ GeV) at KEK-PS. Both the incident K^+ and outgoing π^+ were measured using the K6 beam line and the forward spectrometer, Superconducting Kaon Spectrometer (SKS), leading to a good mass

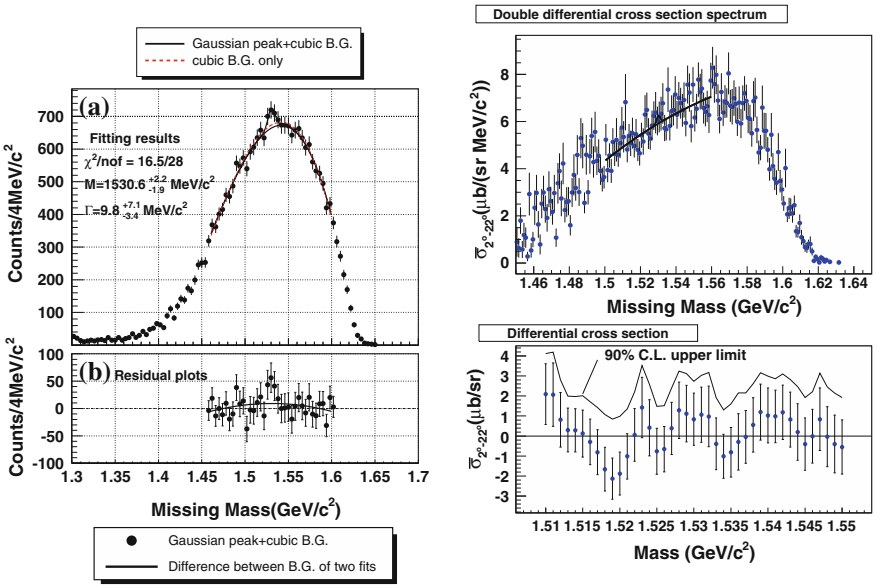

Fig. 1.8 Results of the KEK-PS E522 and E559 experiments. (*Left*) (**a**) Missing mass spectrum of the $\pi^- p \rightarrow K^- X$ reaction at 1.92 GeV/c obtained in the E522 experiment [86]. The *solid line* represents the fitting result with third-order polynomial background and a Gaussian peak. The *red dashed line* represents the fitting result with only the background. (**b**) Residual plot from the background function obtained from the fitting with third-order polynomial background and a Gaussian peak. (*Right*) (*Top*) Missing mass spectrum of the $K^+ p \rightarrow \pi^+ X$ reaction at 1.2 GeV/c obtained in the E559 experiment [87]. The spectrum was fitted using a second-order polynomial function and a Gaussian peak with a fixed width of 2.4 MeV (FWHM). (*Bottom*) The upper limits of the differential cross section of the $K^+ p \rightarrow \pi^+ \Theta^+$ reaction averaged over 2° to 22° in the laboratory frame as a function of the mass of Θ^+

resolution of 2.4 MeV (FWHM). Since the low-momentum kaon beam was used, the missing mass spectrum includes the background originating from the beam K^+ decay. As shown in Fig. 1.8 (right), no clear peak was observed in the missing mass spectrum. The upper limit of the differential cross section averaged over 2–22° in the laboratory frame was estimated to be 3.5 μb/sr at the 90 % C.L.

1.4.5 Isospin of Θ^+

If the Θ^+ belongs to the antidecuplet as shown in Fig. 1.2, the isospin is 0 by definition. Nevertheless, this should be confirmed experimentally. If it was an isovector ($I = 1$), one might expect to observe its isospin partners, Θ^0 and Θ^{++}. The Θ^{++} was searched for in the pK^+ decay channel, but no evidence was observed in the SAPHIR [42], HERMES [60], ZEUS [61], and CLAS [88] experiments, even though each reported positive evidence for Θ^+. No observation was also reported in the

DELPHI [65] and JLab Hall A [89] experiments. These results indicate that possibility of the isovector was excluded. The Θ^+ is likely to be isoscalar ($I = 0$).

1.4.6 Other Pentaquarks

If the Θ^+ exists and is a member of the antidecuplet, other members of the antidecuplet should exist, and a charmed analog of Θ^+ may exist. In 2004, a doubly strange pentaquark $\Xi_{3/2}^{--}$ (also denoted as Φ^{--}), which is positioned at the bottom left corner of the antidecuplet shown in Fig. 1.2, was observed at 1862 MeV in the $\Xi^-\pi^-$ and $\bar{\Xi}^+\pi^+$ invariant mass spectra in proton-proton collisions at $\sqrt{s} = 17.2$ GeV by the NA49 Collaboration [90]. An anticharmed pentaquark Θ_c^0 ($uudd\bar{c}$) was observed at 3099 MeV in the $D^{*-}p$ and $D^{*+}\bar{p}$ invariant mass spectra in electron-proton collisions at $\sqrt{s} = 300$ and 320 GeV by the H1 Collaboration [91]. These evidences had encouraged the study of pentaquarks more vigorously at that time. However, these evidences were not supported by any other subsequent experiments; the $\Xi_{3/2}^{--}$ was not observed in the HERA-B [77], WA89 [92], ALEPH [64], HERMES [93], COMPASS [94], ZEUS [95], BaBar [66], E690 [96], EXCHARM [97], CDF [98], DELPHI [65], H1 [99], FOCUS [100], and CLAS [101] experiments; the Θ_c^0 was not observed in the ZEUS [102], ALEPH [64], CDF [80], BaBar [103], CHORUS [104], and DELPHI [65] experiments. At present, the evidence for either $\Xi_{3/2}^{--}$ or Θ_c^0 is hardly credible unless further evidences are reported.

1.4.7 Summary of Experimental Results

As described above, the experimental situation for the Θ^+ pentaquark is controversial. The followings are the current situation of Θ^+ from an experimental point of view:

- The mass of Θ^+ reported in the experiments with positive evidence ranged from 1520 to 1550 MeV/c^2. The Θ^+ is generally denoted as $\Theta(1540)^+$, or sometimes $\Theta(1530)^+$.
- The width of Θ^+ measured in the experiments is usually limited by the experimental resolution of 10–25 MeV. Only the DIANA Collaboration reported a finite width of 0.34 ± 0.10 MeV estimated from the production cross section [56]. At least, the width should be less than a few MeV from the reanalyses of the past K^+d scattering data.
- Non-existence of the Θ^{++} resonance indicates that the isospin of Θ^+ is 0.
- The spin and parity of Θ^+ have not been determined yet experimentally.

One of the problems on the Θ^+ is that the positive evidences were usually reported with limited statistics. The statistical significance of the Θ^+ peaks were questioned due to uncertainty of the shape of the background under the peaks. Figure 1.9 shows a

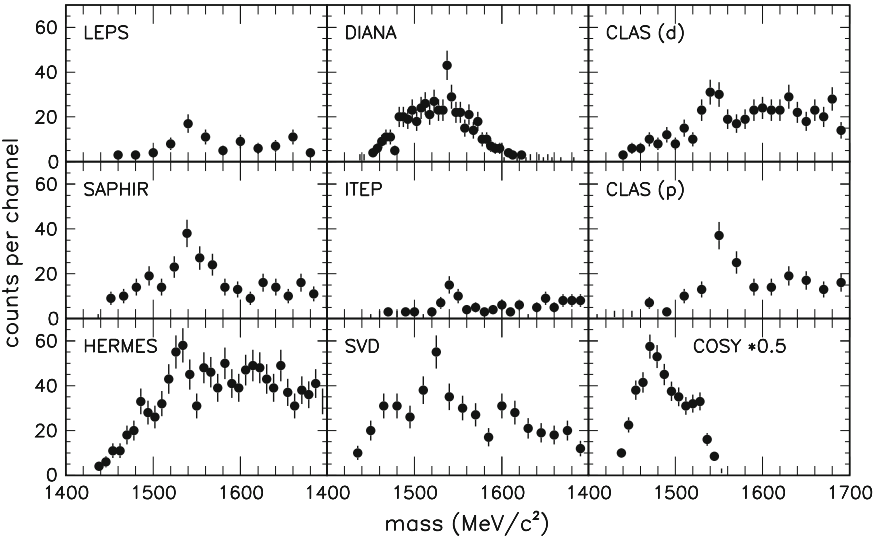

Fig. 1.9 Summary of early experiments reporting the Θ^+ evidence, presented without fitted curves, taken form [105]

summary of early experiments reporting the Θ^+ evidence, presented by Pochodzalla [105], where the data were plotted with statistical error bars and without fitted curves. He suggested that obviously a common drawback of the individual observation is the limited statistics and hence limited confidence of the peaks. As described so far, some of these positive results were later disproved by the higher statistics data by the collaboration itself, or criticized by other experiments; the LEPS and DIANA Collaborations, however, confirmed the evidence by further analysis using improved statistics data.

In addition, the problem of arbitrary selection criteria was pointed out by several authors, e.g., [10, 38, 105]. Because of the low statistics, it is important to note that any cuts applied during the search process can modify the statistical significance of an a priori unknown peak, unless the cuts are justified with an independent data sample or Monte Carlo data.

Anyway, the solution that convinces everyone of the existence of Θ^+ could be obtained from confirming the evidence by various independent experiments with high statistics.

1.5 Θ^+ Production Via Meson-Induced Reactions

On the basis of the previous experimental results, the production mechanism of the Θ^+ via meson-induced reactions at low energy is discussed in this section. As described in Sect. 1.4.4, the Θ^+ was not observed in both the π^- and K^+ induced reactions. What can we learn from this?

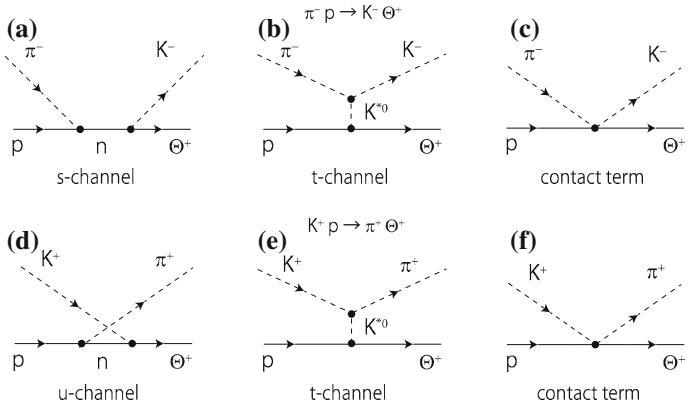

Fig. 1.10 Diagrams for the $\pi^- p \to K^- \Theta^+$ (**a**, **b**, **c**) and $K^+ p \to \pi^+ \Theta^+$ (**d**, **e**, **f**) reactions at the tree level for the isosinglet Θ^+

Theoretical calculations for the meson-induced Θ^+ productions have been studied in Refs. [106–113], where the authors adopted the effective interaction Lagrangian approach with several reaction mechanisms and different frameworks. Figure 1.10 shows possible diagrams for the $\pi^- p \to K^- \Theta^+$ and $K^+ p \to \pi^+ \Theta^+$ reactions at the tree level for the isosinglet Θ^+. For the $\pi^- p \to K^- \Theta^+$ reaction, s- and t-channel diagrams together with the contact term are allowed. Because $I = 0$ is assumed for Θ, the u-channel is precluded, where an isospin partner Θ^{++} is needed as an intermediate state. In the s-channel diagram, only a neutron is considered as an intermediate state for simplicity. In the t-channel diagram, a K^{*0} vector meson is exchanged, whereas a K^0 pseudoscalar meson exchange is forbidden due to the parity conservation at the three-meson vertex. The diagrams for the $K^+ p \to \pi^+ \Theta^+$ reaction are obtained crossing the π and K.

In the theoretical calculations published so far [106–113], the authors considered all or part of diagrams in Fig. 1.10, adopted the pseudoscalar and/or pseudovector coupling scheme for the Yukawa couplings, and often introduced phenomenological form factors to reflect the finite size of hadrons. (See the recent paper [113] for detailed formalism.) The results can be different depending on details of the model employed; nevertheless, qualitative understanding of the experimental results is important. Although some of theoretical parameters can be determined from known hadronic reactions (e.g., $K^* \to K\pi$ and πN scattering), the $KN\Theta$, $K^*N\Theta$ and $N\pi K\Theta$ couplings are unknown. Note that the $KN\Theta$ coupling constant, $g_{KN\Theta}$, is directly related to the width of Θ^+, Γ_Θ.

Figure 1.11 (left) shows the differential cross sections of the $K^+ p \to \pi^+ \Theta^+$ reaction at $\sqrt{s} = 2.4\,\text{GeV}$ calculated by Oh et al. [109], taking account of the t- and u-channels for the spin-parity of $1/2^+$. Their calculation is controlled by two coupling constants, $g_{KN\Theta}$ and $g_{K^*N\Theta}$. They assumed that $g_{KN\Theta} = 1.0$ which corresponds to $\Gamma_\Theta = 1.03\,\text{MeV}$. In case of hyperons ($Y$), $|g_{K^*NY}|$ is usually smaller than $|g_{KNY}|$; therefore, they assumed the following three cases: $g_{K^*N\Theta} = g_{KN\Theta}$, $g_{K^*N\Theta} = -g_{KN\Theta}$,

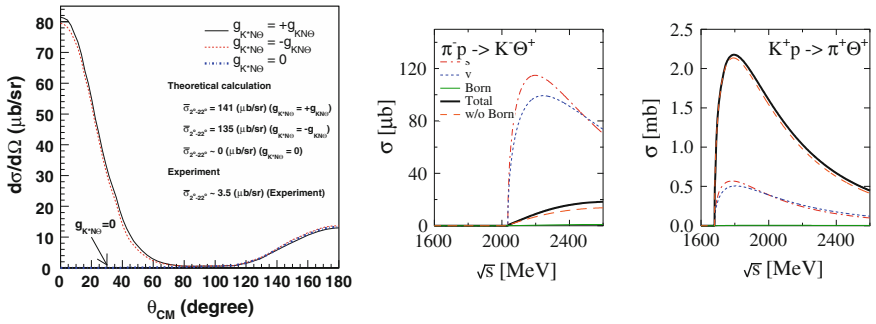

Fig. 1.11 (*Left*) Differential cross sections of the $K^+p \to \pi^+\Theta^+$ reaction calculated by Oh et al. [109] at $\sqrt{s} = 2.4\,\text{GeV}$ (the E559 experiment [87] was carried out at $\sqrt{s} = 1.9\,\text{GeV}$). The *solid*, *dashed*, and *dashed-dotted lines* represent $g_{K^*N\Theta} = g_{KN\Theta}$, $g_{K^*N\Theta} = -g_{KN\Theta}$, and $g_{K^*N\Theta} = 0$, respectively. This figure is taken from [87]. (*Middle and right*) Total cross sections of the $\pi^-p \to K^-\Theta^+$ and $K^+p \to \pi^+\Theta^+$ reactions calculated by Hyodo and Hosaka [112] for $1/2^+$ with $g^s = 1.59$ and $g^v = -0.27$. "s" and "v" stand for the scalar and vector type amplitudes in the contact term, respectively (see text)

and $g_{K^*N\Theta} = 0$. If the t-channel process exists ($g_{K^*N\Theta} = \pm g_{KN\Theta}$), the differential cross section would have a forward peak distribution as shown by the solid and dashed lines in Fig. 1.11 (left). The calculated differential cross section averaged over 2°–22° in the laboratory frame, $\bar{\sigma}_{2^\circ-22^\circ}$, is about 140 μb/sr in this case. The upper limit of 3.5 μb/sr obtained from the E559 experiment [87] is much smaller than this value. Thus, the t-channel process is excluded by the E559 result; i.e., $g_{K^*N\Theta}$ must be very small. If only the u-channel process exists ($g_{K^*N\Theta} = 0$), the differential cross section shows a backward peak distribution as shown by the dashed-dotted line in Fig. 1.11 (left). In this case, $\bar{\sigma}_{2^\circ-22^\circ}$ is almost 0 μb/sr. Because the acceptance of E559 is limited to forward angles, it is not sensitive to the u-channel contribution.

The contribution of the contact term was studied by Hyodo and Hosaka [112]. The $N\pi K\Theta$ coupling constant was determined from N^* decay into $\pi\pi N$ channel, consisting of the $\pi\pi(I = 0, s\text{ wave})N$ and $\pi\pi(I = 1, p\text{ wave})N$ modes, referred to as "scalar" and "vector" types, respectively; therefore, two coupling constants g^s and g^v contribute to the contact term. They calculated the cross sections of both the $\pi^-p \to K^-\Theta^+$ and $K^+p \to \pi^+\Theta^+$ reactions for the spin-parity of $1/2^+$ and $3/2^-$, taking account of the s- and u-channels as well as the contact term. Figure 1.11 (middle and right) shows the calculated total cross sections for $1/2^+$ with $g^s = 1.59$ and $g^v = -0.27$. The s-channel contribution (labeled "Born" in the figure) is negligibly small owing to the small width assumed $\Gamma_\Theta = 1\,\text{MeV}$ in their calculation. As shown in Fig. 1.11 (middle), the total cross section of the $\pi^-p \to K^-\Theta^+$ reaction is suppressed due to the destructive interference between the scalar and vetor type amplitudes (labeled "s" and "v" in the figure), which can help to explain the small cross section of <3.9 μb obtained from the E522 experiment [86]. On the other hand, as shown in Fig. 1.11 (right), the total cross section of the $K^+p \to \pi^+\Theta^+$ reaction is enhanced due to the constructive interference between the two amplitudes,

which connot explain the small cross section of $<3.5\,\mu$b/sr obtained from the E559 experiment [87]. The $3/2^-$ case also shows a similar tentdency. Thus, the possible solution is that both g^s and g^v are quite small.

In summary, the theoretical calculations described above suggest that the contributions of the t-channel process and contact term must be very small from the E522 and E559 results.

1.6 Present Experiment: J-PARC E19

The experimental situation about the Θ^+ is controversial, and therefore it is important to confirm the existence of the Θ^+ in an unambiguous way. As described in Sect. 1.4.4, the KEK-E522 Collaboration reported the bump structure at 1530 MeV in the $\pi^- p \to K^- X$ reaction with an incident momentum of 1.92 GeV/c. Although the statistical significance was not sufficient to claim the evidence, it is suggestive of a possible signal of the Θ^+. The significance was limited by the poor mass resolution of 13.4 MeV (FWHM). We can improve the resolution by an order of magnitude with a good spectrometer system.

Under the current situation, the present experimental search should satisfy the following requirements. (i) High-statistics data are indispensable in order not to be disturbed by statistical fluctuation. (ii) High resolution of less than a few MeV is desirable to measure the potentially narrow Θ^+.

The present experiment (J-PARC E19 [114]) was proposed to search for the Θ^+ using the $\pi^- p \to K^- X$ reaction. It was timely to use high-intensity meson beams at the recently constructed J-PARC facility [115]. We have constructed a high-resolution spectrometer system in order to achieve a good mass resolution of 2 MeV (FWHM). Since we used the missing mass technique with a liquid hydrogen target, we could avoid corrections for the Fermi motion or rescattering effect. An order of magnitude higher sensitivity than the previous E522 experiment was expected.

As described in the previous section, the production mechanism of Θ^+ in the $\pi^- p \to K^- \Theta^+$ reaction was theoretically discussed on the basis of the KEK-E522 and E559 results. Knowing that the t-channel and contact term contributions are very small, the s-channel contribution is important in the $\pi^- p \to K^- \Theta^+$ reaction. Since the s-channel amplitude is related to the Θ^+ decay width through the coupling constant $g_{KN\Theta}$ (Fig. 1.10a), we are able to estimate the width, which is the most peculiar property of Θ^+, from the cross section measured in the experiment.

In 2010, the first physics run of the E19 experiment was carried out at the J-PARC K1.8 beam line using a beam momentum of 1.92 GeV/c in order to obtain a direct comparison with the E522 result. Figure 1.12 shows the missing mass spectrum obtained from the 2010 data [116]. No peak structure corresponding to the Θ^+ was observed. The upper limit of the production cross section averaged over scattering angles of 2–15° was estimated to be 0.26 μb/sr in a mass region of 1510–1550 MeV/c^2. This upper limit is an order of magnitude lower than the previous E522 experimental result of 2.9 μb/sr [86]. It was concluded that the bump structure

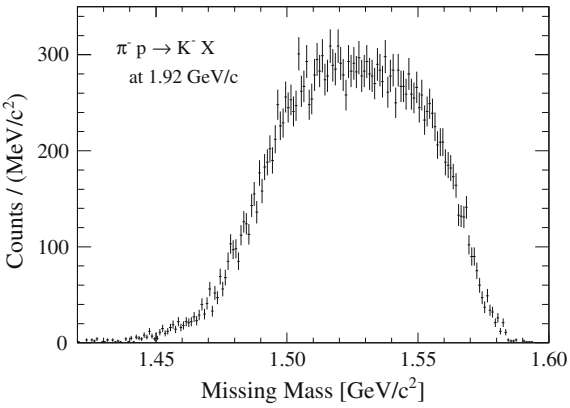

Fig. 1.12 Missing mass spectrum of the $\pi^- p \to K^- X$ reaction at 1.92 GeV/c obtained from the E19-2010 data [116]

observed in the E522 experiment was not a sign of Θ^+ (notably the E522 Collaboration did not claim so).

Comparing the above 2010 result with a theoretical calculation using the effective Lagrangian approach with the s-channel diagram [113], the upper limit of the Θ^+ width at the 90 % C.L. was estimated to be 0.72 and 3.1 MeV for the spin-parity of $1/2^+$ and $1/2^-$, respectively. This upper limit of the width could not exclude the DIANA result of $\Gamma_\Theta = 0.34 \pm 0.10$ MeV [56],[2] which is the only result reporting a finite width of Θ^+. Furthermore, it could not overcome even the upper limit of $\Gamma_\Theta < 0.64$ MeV reported by the Belle Collaboration [57]. Since the statistical uncertainty dominated in the determination of the upper limit in the 2010 data, 3 times more statistics are needed to improve the upper limit to 1/2, if we continue the data-taking at the 1.92-GeV/c momentum.

In theoretical calculations [108, 113], the cross section of the $\pi^- p \to K^- \Theta^+$ reaction was predicted to increase with higher energy. Figure 1.13 shows the total cross sections of the $\pi^- p \to K^- \Theta^+$ reaction calculated by Hyodo, Hosaka, and Oka [113] for $J^P = 1/2^+$, considering only the s-channel diagram. Each line represents a type of the coupling scheme and form factor, details of which are described in Sect. 5.1.1. The beam momentum of 1.92 GeV/c corresponds to $\sqrt{s} = 2124$ MeV. The cross section is predicted to increase except for the PS-Fc case. The maximum momentum available at the K1.8 beam line is 2 GeV/c, which corresponds to $\sqrt{s} = 2164$ MeV. Thus, we determined to perform the experiment using a beam momentum of 2 GeV/c in order to challenge the DIANA result. The data with different momenta must be more useful than the data with only increase of statistics.

The second physics run of the E19 experiment was carried out in 2012 using a beam momentum of 2 GeV/c. The experimental setup was slightly improved to cover a wider momentum acceptance, described in the next chapter. We expected to obtain more stringent constraint on the existence of Θ^+.

[2]The latest DIANA result before 2012 was $\Gamma_\Theta = 0.39 \pm 0.10$ MeV [17].

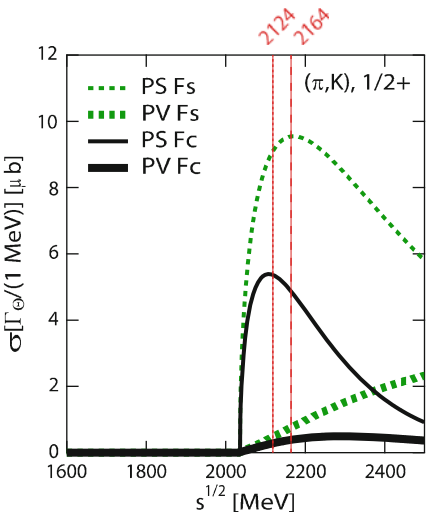

Fig. 1.13 Total cross sections of the $\pi^- p \to K^- \Theta^+$ reaction calculated by Hyodo et al. [113] for $J^P = 1/2^+$ in units of $\Gamma_\Theta/(1\,\mathrm{MeV})$ [μb], considering only the s-channel diagram. Each line represents a type of the coupling scheme and form factor (see text in Sect. 5.1.1). Beam momenta of 1.92 and 2.01 GeV/c correspond to $\sqrt{s} = 2124$ and 2164 MeV, respectively

In this thesis, the result of the 2012 data at 2 GeV/c is presented including details of the experimental apparatus and analysis procedures. Using both the 2010 and 2012 data together with a theoretical calculation, constraint on the Θ^+ width is discussed.

References

1. M. Gell-Mann, Phys. Lett. **8**, 214 (1964)
2. R.L. Jaffe, *Proceedings of Topical Conference on Baryon Resonances* (Oxford, 1976) SLAC-PUB-1774
3. R.L. Jaffe, Phys. Rev. D **15**, 267, 281 (1977)
4. R.L. Jaffe, Phys. Rev. Lett. **38**, 195, 617(E) (1977)
5. D. Strottman, Phys. Rev. D **20**, 748 (1979)
6. S. Godfrey, S.L. Olsen, Ann. Rev. Nucl. Part. Sci. **58**, 51 (2008)
7. D. Diakonov, V. Petrov, M. Polyakov, Z. Phys. A **359**, 305 (1997)
8. T. Nakano et al., LEPS Collaboration. Phys. Rev. Lett. **91**, 012002 (2003)
9. K.H. Hicks, Prog. Part. Nucl. Phys. **55**, 647 (2005)
10. K.H. Hicks, Eur. Phys. J. H **37**, 1 (2012)
11. R. Jaffe, F. Wilczek, Eur. Phys. J. C **33**, s38 (2004)
12. S. Nussinov, arXiv:hep-ph/0307357
13. R.A. Arndt, I.I. Strakovsky, R.L. Workman, Phys. Rev. C **68**, 042201(R) (2003); **69**, 019901(E) (2004)
14. J. Haidenbauer, G. Krein, Phys. Rev. C **68**, 052201(R) (2003)
15. A. Sibirtsev, J. Haidenbauer, S. Krewald, Ulf-G Meißner, Phys. Lett. B **599**, 230 (2004)
16. R.N. Cahn, G.H. Trilling, Phys. Rev. D **69**, 011501(R) (2004)
17. V.V. Barmin et al., DIANA Collaboration. Phys. Atom. Nucl. **66**, 1715 (2003); **70**, 35 (2007); **73**, 1168 (2010)
18. W.R. Gibbs, Phys. Rev. C **70**, 045208 (2004)
19. T. Bowen et al., Phys. Rev. D **2**, 2599 (1970)
20. F. Huang, Z.Y. Zhang, Y.W. Yu, B.S. Zou, Phys. Lett. B **586**, 69 (2004)

21. K. Goeke, H.-C. Kim, M. Praszałowicz, G.-S. Yang, Prog. Part. Nucl. Phys. **55**, 350 (2005)
22. R.L. Jaffe, Phys. Rep. **409**, 1 (2005)
23. R. Jaffe, F. Wilczek, Phys. Rev. Lett. **91**, 232003 (2003)
24. M. Karliner, H.J. Lipkin, Phys. Lett. B **575**, 249 (2003)
25. S. Sasaki, Nucl. Phys. B (Proc. Suppl.) **140**, 127 (2005)
26. F. Csikor, Z. Fodor, S.D. Katz, T.G. Kovács, J. High Energy Phys. **11**, 070 (2003)
27. F. Csikor, Z. Fodor, S.D. Katz, T.G. Kovács, B.C. Tóth, Phys. Rev. D **73**, 034506 (2006)
28. S. Sasaki, Phys. Rev. Lett. **93**, 152001 (2004)
29. T.-W. Chiu, T.-H. Hsieh, Phys. Rev. D **72**, 034505 (2005)
30. N. Mathur et al., Phys. Rev. D **70**, 074508 (2004)
31. N. Ishii, T. Doi, H. Iida, M. Oka, F. Okiharu, H. Suganuma, Phys. Rev. D **71**, 034001 (2005)
32. N. Ishii, T. Doi, Y. Nemoto, M. Oka, H. Suganuma, Phys. Rev. D **72**, 074503 (2005)
33. B.G. Lasscock et al., Phys. Rev. D **72**, 014502 (2005)
34. B.G. Lasscock et al., Phys. Rev. D **72**, 074507 (2005)
35. T.T. Takahashi, T. Umeda, T. Onogi, T. Kunihiro, Phys. Rev. D **71**, 114509 (2005)
36. C. Alexandrou, A. Tsapalis, Phys. Rev. D **73**, 014507 (2006)
37. K. Holland, K.J. Juge, BGR Collaboration. Phys. Rev. D **73**, 074505 (2006)
38. M.V. Danilov, R.V. Mizuk, Phys. Atom. Nucl. **71**, 605 (2008)
39. S. Eidelman et al., Particle Data Group. Phys. Lett. B **592**, 1 (2004)
40. W.-M. Yao et al., Particle Data Group. J. Phys. G **33**, 1 (2006)
41. C. Amsler et al., Particle Data Group. Phys. Lett. B **667**, 1 (2008)
42. J. Barth et al., SAPHIR Collaboration. Phys. Lett. B **572**, 127 (2003)
43. S. Stepanyan et al., CLAS Collaboration. Phys. Rev. Lett. **91**, 252001 (2003)
44. V. Kubarovsky et al., CLAS Collaboration. Phys. Rev. Lett. **92**, 032001 (2004)
45. M. Battaglieri et al., CLAS Collaboration. Phys. Rev. Lett. **96**, 042001 (2006)
46. R. De Vita et al., CLAS Collaboration. Phys. Rev. D **74**, 032001 (2006)
47. B. McKinnon et al., CLAS Collaboration. Phys. Rev. Lett. **96**, 212001 (2006)
48. S. Niccolai et al., CLAS Collaboration. Phys. Rev. Lett. **97**, 032001 (2006)
49. T. Nakano et al., LEPS Collaboration. Phys. Rev. C **79**, 025210 (2009)
50. M.J. Amaryan et al., Phys. Rev. C **85**, 035209 (2012)
51. A. Martínez Torres, E. Oset, Phys. Rev. Lett. **105**, 092001 (2010); Phys. Rev. C **81**, 055202 (2010)
52. Y. Kato, LEPS Collaboration. Few-Body Syst. **54**, 1245 (2013)
53. M. Ostrick, Prog. Part. Nucl. Phys. **55**, 337 (2005)
54. S.-I. Nam, A. Hosaka, H.-C. Kim, Phys. Lett. B **633**, 483 (2006)
55. M. Anghinolfi et al., Phys. Rev. C **86**, 069801 (2012)
56. V.V. Barmin et al., DIANA Collaboration. Phys. Rev. C **89**, 045204 (2014)
57. R. Mizuk et al., Belle Collaboration. Phys. Lett. B **632**, 173 (2006)
58. J. Beringer et al., Particle Data Group. Phys. Rev. D **86**, 010001 (2012)
59. A.E. Asratyan, A.G. Dolgolenko, M.A. Kubantsev, Phys. Atom. Nucl. **67**, 682 (2004)
60. A. Airapetian et al., HERMES Collaboration. Phys. Lett. B **585**, 213 (2004)
61. S. Chekanov et al., ZEUS Collaboration. Phys. Lett. B **591**, 7 (2004)
62. A. Aktas et al., H1 Collaboration. Phys. Lett. B **639**, 202 (2006)
63. J.Z. Bai et al., BES Collaboration. Phys. Rev. D **70**, 012004 (2004)
64. S. Schael et al., ALEPH Collaboration. Phys. Lett. B **599**, 1 (2004)
65. J. Abdallah et al., DELPHI Collaboration. Phys. Lett. B **653**, 151 (2007)
66. B. Aubert et al., BaBar Collaboration. Phys. Rev. Lett. **95**, 042002 (2005)
67. M.-Z. Wang et al., Belle Collaboration. Phys. Lett. B **617**, 141 (2005)
68. B. Aubert et al., BaBar Collaboration. Phys. Rev. D **76**, 092004 (2007)
69. P. Achard et al., L3 Collaboration. Eur. Phys. J. C **49**, 395 (2007)
70. J.M. Link et al., FOCUS Collaboration. Phys. Lett. B **639**, 604 (2006)
71. O. Samoylov et al., NOMAD Collaboration. Eur. Phys. J. C **49**, 499 (2007)
72. K. Götzen, BaBar Collaboration. Nucl. Phys. B (Proc. Suppl.) **164**, 117 (2007)
73. Y.I. Azimov, I.I. Strakovsky, Phys. Rev. C **70**, 035210 (2004)

74. A.N. Aleev et al., SVD Collaboration. Phys. Atom. Nucl. **68**, 974 (2005)
75. A. Aleev et al., SVD Collaboration, arXiv:hep-ex/0509033
76. Y.M. Antipov et al., SPHINX Collaboration. Eur. Phys. J. A **A21**, 455 (2004)
77. I. Abt et al., HERA-B Collaboration. Phys. Rev. Lett **93**, 212003 (2004)
78. M.J. Longo et al., HyperCP Collaboration. Phys. Rev. D **70**, 111101(R) (2004)
79. C. Pinkenburg et al., PHENIX Collaboration. J. Phys. G **30**, S1201 (2004)
80. D.O. Litvintsev et al., CDF Collaboration. Nucl. Phys. B (Proc. Suppl.) **142**, 374 (2005)
81. M.I. Adamovich et al., WA89 Collaboration. Phys. Rev. C **72**, 055201 (2005)
82. A.I. Titov, A. Hosaka, S. Daté, Y. Ohashi, Phys. Rev. C **70**, 042202(R) (2004)
83. M. Abdel-Bary et al., COSY-TOF Collaboration. Phys. Lett. B **595**, 127 (2004)
84. M. Abdel-Bary et al., COSY-TOF Collaboration. Phys. Lett. B **649**, 252 (2007)
85. M. Nekipelov et al., COSY-ANKE Collaboration. J. Phys. G **34**, 627 (2007)
86. K. Miwa et al., KEK-PS E522 Collaboration. Phys. Lett. B **635**, 72 (2006)
87. K. Miwa et al., KEK-PS E559 Collaboration. Phys. Rev. C **77**, 045203 (2008)
88. V. Kubarovsky et al., CLAS Collaboration. Phys. Rev. Lett. **97**, 102001 (2006)
89. Y. Qiang et al., Jefferson Lab Hall A Collaboration. Phys. Rev. C **75**, 055208 (2007)
90. C. Alt et al., NA49 Collaboration. Phys. Rev. Lett. **92**, 042003 (2004)
91. A. Aktas et al., H1 Collaboration. Phys. Lett. B **588**, 17 (2004)
92. M.I. Adamovich et al., WA89 Collaboration. Phys. Rev. C **70**, 022201(R) (2004)
93. A. Airapetian et al., HERMES Collaboration. Phys. Rev. D **71**, 032004 (2005)
94. E.S. Ageev et al., COMPASS Collaboration. Eur. Phys. J. C **41**, 469 (2005)
95. S. Chekanov et al., ZEUS Collaboration. Phys. Lett. B **610**, 212 (2005)
96. D.C. Christian et al., FNAL E690 Collaboration. Phys. Rev. Lett. **95**, 152001 (2005)
97. A.N. Aleev et al., EXCHARM Collaboration. Phys. Atom. Nucl. **70**, 1527 (2007)
98. A. Abulencia et al., CDF Collaboration. Phys. Rev. D **75**, 032003 (2007)
99. A. Aktas et al., H1 Collaboration. Eur. Phys. J. C **52**, 507 (2007)
100. J.M. Link et al., FOCUS Collaboration. Phys. Lett. B **661**, 14 (2008)
101. H. Egiyan et al., CLAS Collaboration. Phys. Rev. C **85**, 015205 (2012)
102. S. Chekanov et al., ZEUS Collaboration. Eur. Phys. J. C **38**, 29 (2004)
103. B. Aubert et al., BaBar Collaboration. Phys. Rev. D **73**, 091101 (2006)
104. G. De Lellis et al., CHORUS Collaboration. Nucl. Phys. B **763**, 268 (2007)
105. J. Pochodzalla, arXiv:hep-ex/0406077 (Talk presented at the 2nd PANDA Physics Workshop, Frascati, 2004)
106. W. Liu, C.M. Ko, Phys. Rev. C **68**, 045203 (2003)
107. T. Hyodo, A. Hosaka, E. Oset, Phys. Lett. B **579**, 290 (2004)
108. Y. Oh, H. Kim, S.H. Lee, Phys. Rev. D **69**, 014009 (2004)
109. Y. Oh, H. Kim, S.H. Lee, Phys. Rev. D **69**, 074016 (2004)
110. C.M. Ko, W. Liu, arXiv:nucl-th/0410068 (Proceedings of PENTAQUARK04)
111. P. Ko, J. Lee, T. Lee, J.-H. Park, Phys. Lett. B **611**, 87 (2005)
112. T. Hyodo, A. Hosaka, Phys. Rev. C **72**, 055202 (2005)
113. T. Hyodo, A. Hosaka, M. Oka, Prog. Theor. Phys. **128**, 523 (2012)
114. M. Naruki et al., J-PARC proposal **E19** (2006), http://j-parc.jp/researcher/Hadron/en/pac_0606/pdf/p19-Naruki.pdf
115. T. Nagae (ed.), Special Issue: Particle and Nuclear Physics at J-PARC, Prog. Theor. Exp. Phys. Issue 2 (2012)
116. K. Shirotori et al., J-PARC E19 Collaboration. Phys. Rev. Lett. **109**, 132002 (2012)

Chapter 2
Experimental Apparatus

The experiment was performed at the K1.8 beam line in the J-PARC hadron facility with a high-resolution spectrometer system: the K1.8 beam spectrometer and the Superconducting Kaon Spectrometer (SKS) [1]. As the J-PARC E19 experiment, the previous and present data were taken in 2010 and 2012 using pion beams of 1.92 and 2.01 GeV/c[1] momenta, respectively. The $\pi^- p \rightarrow K^- X$ reaction on a liquid hydrogen target was used to search for the Θ^+ pentaquark. Beam pions and outgoing kaons were identified and analyzed by the beam spectrometer and SKS, respectively. In this chapter, details of the experimental components are described.

2.1 J-PARC and Hadron Experimental Facility

J-PARC (Japan Proton Accelerator Research Complex) [2] is a high intensity proton accelerator facility which aims to pursue frontier in nuclear physics, particle physics, material and life science, and nuclear technology, with the highest beam power in the world. J-PARC consists of three accelerators: LINAC (Linear Accelerator), RCS (Rapid Cycling Synchrotron), and MR (Main Ring). A bird's-eye view of the entire facility is shown in Fig. 2.1.

A negative hydrogen ion, H^-, was produced at an ion source and accelerated by LINAC up to 181 MeV. The accelerated H^- was converted to a proton (H^+) and injected to RCS, which accelerates the proton up to 3 GeV. Part of the protons were injected to MR and accelerated up to 30 GeV. The primary proton beam was extracted with a slow extraction scheme for a duration of 2.2 second in every 6 second; this duration of the beam extraction is called a spill. Typical proton beam intensities were 3×10^{12} and 4×10^{12} per spill in 2010 and 2012, respectively. The extracted proton beams were transported to the hadron experimental facility and bombarded

[1] 2.01 GeV/c is a momentum after an offline calibration. The nominal momentum was 2.00 GeV/c.

M. Moritsu, *Search for the Pentaquark Θ^+ via the $\pi^- p \rightarrow K^- X$ Reaction at J-PARC*, Springer Theses, DOI 10.1007/978-981-10-0012-6_2

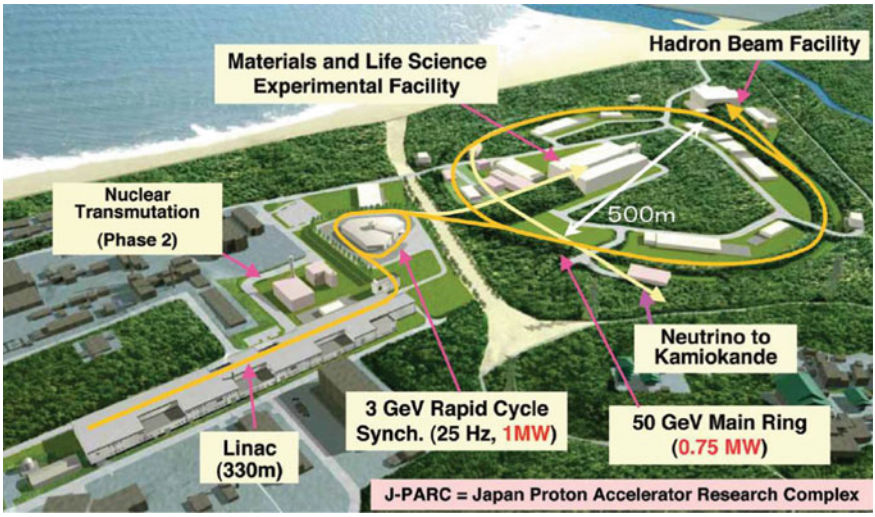

Fig. 2.1 Entire view of J-PARC, taken from [2]

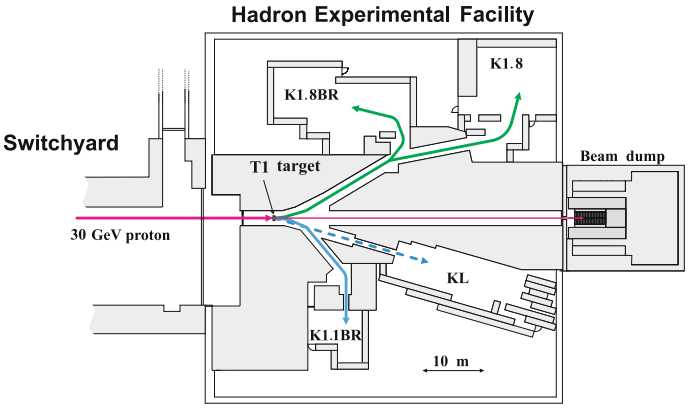

Fig. 2.2 Schematic view of the hadron experimental facility

to a platinum production target ($\phi 6 \times 60$ mm). Produced particles such as pions and kaons were delivered to experimental areas through secondary beam lines and utilized for experiments. A schematic view of the hadron experimental facility is shown in Fig. 2.2.

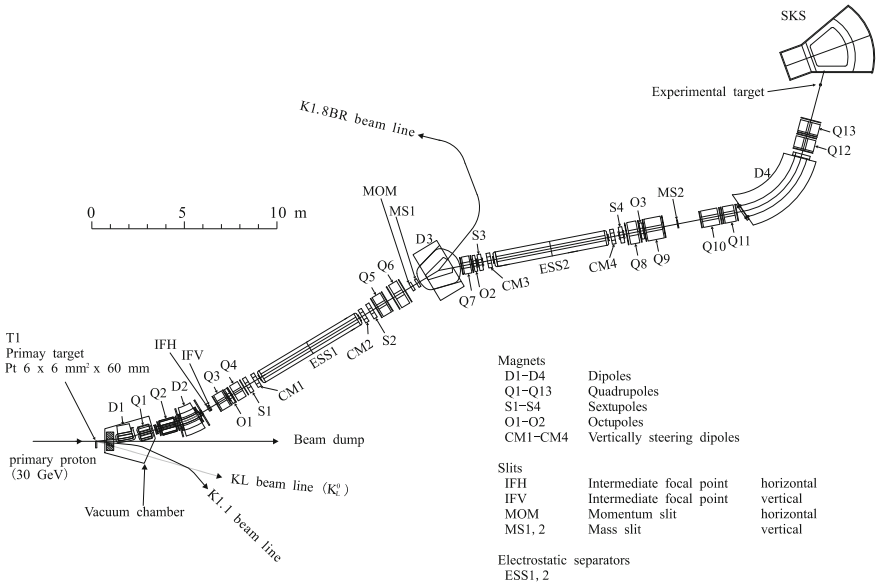

Fig. 2.3 Schematic view of the K1.8 beam line

2.2 K1.8 Beam Line

The K1.8 beam line is a general-purpose mass-separated beam line that can supply various secondary hadron beams up to 2.0 GeV/c [3]. Figure 2.3 shows a schematic view of the K1.8 beam line. The beam line consists of four dipole magnets (D1–D4), thirteen quadrupole magnets (Q1–Q13), four sextupole magnets (S1–S4), three octupole magnets (O1–O3), two electrostatic separators (ESS1 and ESS2) with four correction magnets (CM1–CM4), and four slits (IF, MOM, MS1, and MS2). The total length of the beam line is about 46 m. Figure 2.4 shows the beam envelopes and dispersion function calculated with the first order ion optical parameters.

Secondary pions were produced at the production target located at the most upstream of the beam line. The pion beam was separated by the electrostatic separators. As for a negative pion beam around 2 GeV/c, original contamination from kaons and antiprotons is two orders of magnitude smaller than pions. The separators are especially important for kaon beams. After the momentum and mass selections, the pion beam was focused on the experimental target. A typical beam size at the experimental target position was 10 (horizontal) $\times$ 5 (vertical) mm^2 (rms). The derivatives of the horizontal (dx/dz) and vertical (dy/dz) directions were typically 0.010 and 0.003 (rms), respectively. The beams were almost parallel to the nominal beam axis. In the present experiment, the central beam momenta were set at 1.92 and 2.01 GeV/c in 2010 and 2012, respectively. A typical momentum spread was adjusted to be 1 % (rms) by the momentum slit (MOM).

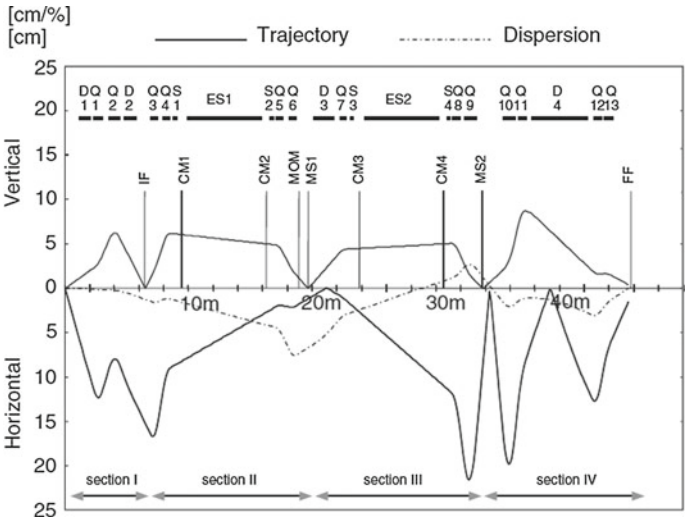

Fig. 2.4 Beam envelopes and dispersion function of the K1.8 beam line [3]

2.2.1 Time Structure of the Beam

In the present beam operation, a spike-like time structure on the extracted beam appeared. This structure arose from fluctuations in the betatron tune, which were due to current ripples of $\sim 10^{-4}$ of the MR magnet power supplies [4]. Figure 2.5 shows a typical instantaneous rate per 100 μs measured with a beam counter at the K1.8 beam line. The maximum instantaneous rate became up to 10–20 times as high as the mean rate due to the spike structure. A quality of the extracted beam is represented by a spill duty factor defined as a ratio of the effective beam time length to the extraction time of 2.2 s. The duty factor was 16–18 % in the present operation in 2010 and 2012.[2]

In physics experiments using coincidence measurements, acceptable counting rates of detectors and data-acquisition system are generally limited by the instantaneous rate. High multiplicity environment causes signal pileups, event overlaps, and dead time of detectors and data acquisition. In particular, the beam spike severely prevented a stable operation of gas chambers in the present experiment. The average secondary beam intensity in the 2010 run was adjusted to 1.0×10^6 per spill. In the 2012 run, we could handle 1.7×10^6 per spill owing to improvements in the spill structure and a practical operation of gas chambers, details of which is described in Sect. 2.3.1.

[2]The time structure was improved step by step, and the duty factor increased to ∼30 % until 2013.

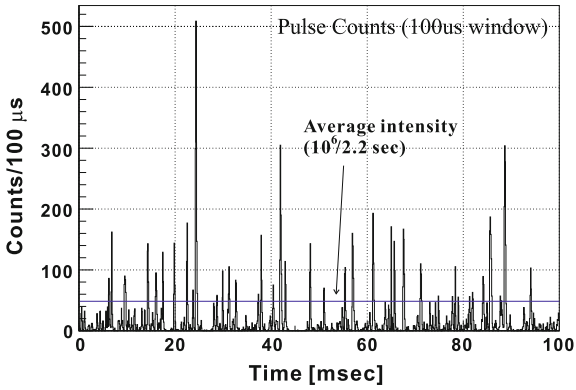

Fig. 2.5 Typical instantaneous rate per 100 μs measured with a beam counter (BH1) The *blue line* indicate the average rate of 10^6 per spill (2.2 s)

2.3 Beam Spectrometer

Figure 2.6 shows a schematic view of the experimental setup at the 2012 run. The last part of the K1.8 beam line is used as a beam spectrometer. The beam spectrometer comprises a QQDQQ magnet system with four sets of wire chambers (BC1–BC4), a gas Cherenkov counter (GC), and two sets of plastic scintillation counters (BH1 and BH2). Details of each detector are described in the following subsections.

Beam tracks were measured by BC1–BC4 at the entrance and exit of the QQDQQ magnets with a position resolution of 200–300 μm. Beam momenta were reconstructed particle by particle with a resolution of 1×10^{-3} (FWHM). In order to minimize the multiple-scattering effect on the momentum resolution, the beam spectrometer optics was designed to realize point-to-point focus to the first order. The magnetic field of the dipole magnet (D4) was monitored during the experimental period by a high-precision Hall probe [5]. Specifications of the beam spectrometer are summarized in Table 2.1.

Table 2.1 Specifications of the beam spectrometer

Maximum momentum	2.0 GeV/c
Maximum field (D4)	1.67 T
Bending angle	64°
Central orbital radius (D4)	4.00 m
Pole gap (D4)	19 cm
Momentum resolution	$\sim 1 \times 10^{-3}$ (FWHM)
Flight path (BH1–BH2)	10.4 m

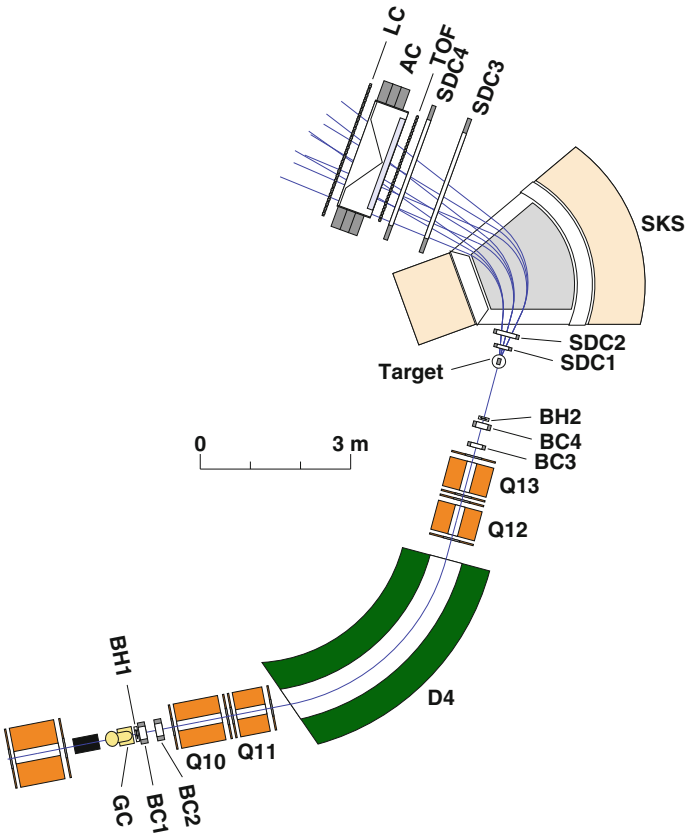

Fig. 2.6 Schematic view of the experimental setup at the 2012 run

2.3.1 Tracking Chambers for the Beam Spectrometer

Specifications of the tracking chambers for the beam spectrometer (BC1–BC4) are listed in Table 2.2.

2.3.1.1 MWPCs (BC1 and BC2)

Detectors at the upstream part of the beam spectrometer are required to operate under high counting rates of 10–20 MHz. According to the past experience at the KEK-PS K6 beam line, where wire chambers with 5 mm sense wire pitch had been used, a deterioration in the detection efficiency became serious with a counting rate over 200 kHz per wire [6, 7]. This situation requires wire chambers with the sense wire pitch of less than 1 mm for the K1.8 beam line. Therefore, multiwire proportional chambers (MWPCs) with 1 mm anode pitch were constructed for BC1 and BC2.

Table 2.2 Specifications of the wire chambers. BC1 and BC2 are MWPCs, while the others are drift chambers

Name	Sensitive area W × H (mm)	Sense wire pitch (mm)	Wire config.	Tilt angle x, u, v (deg)	Resolution (μm in rms)
BC1	256 × 100	1	$xvuxvu$	0, +15, −15	300
BC2	256 × 100	1	$vuxvux$	0, +15, −15	300
BC3	192 × 100	3	$xx'vv'uu'$	0, +15, −15	200
BC4	240 × 150	5	$vv'uu'xx'$	0, +15, −15	200
SDC1	192 × 100	3	$vv'uu'$	0, +15, −15	200
SDC2	400 × 150	5	$vv'uu'xx'$	0, +15, −15	200
SDC3	2140 × 1140	20	$vxuvxu$	0, +30, −30	300
SDC4	2140 × 1140	20	$vxuvxu$	0, +30, −30	300

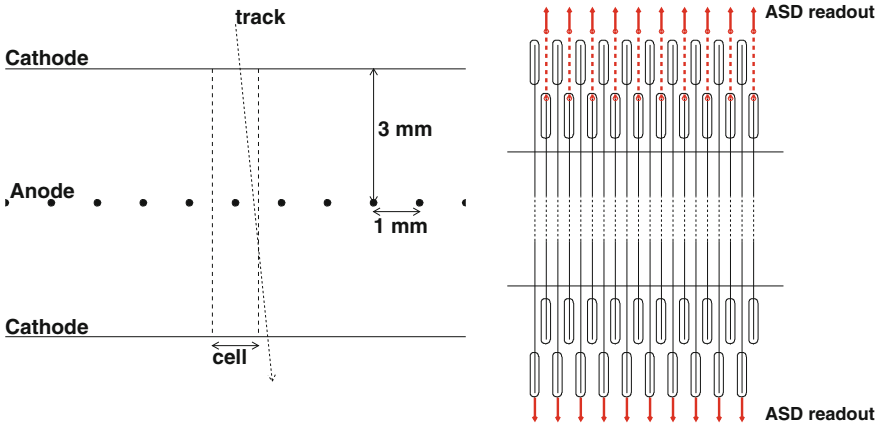

Fig. 2.7 (*Left*) Cell structure of the MWPC (BC1 and BC2). (*Right*) Front view of an anode plane of the MWPC

Note that there are practical difficulties in precisely stringing and soldering wires at a pitch below 1 mm.

A schematic view of the wire structure of the MWPC is shown in Fig. 2.7. Each of BC1 and BC2 has 6 layers labeled like $[xuvxuv]$, where x stands for a vertical-wire plane and u and v are $\pm 15°$-tilted wire planes. The sense wire is a gold-plated tungsten wire alloyed with 3 % rhenium with a diameter of 15 μm. The cathode planes are made of 12 μm thick mylar films coated with a 20 μm thick graphite paste to reduce the damage from discharge. The gas mixture was Ar (76 %) + iso-C_4H_{10} (20 %) + methylal (4 %) at the atmospheric pressure. For the front-end readout electronics, an amplifier-shaper-discriminator chip (CXA3183Q TGC ASD [8]) was used. The timing information of the MWPCs was digitized by an 100 MHz sampling MWPC encoder mounted on the COPPER boards.

As described in Sect. 2.2, the spikes in the beam structure severely prevented a stable operation of gas chambers. This effect was the most serious for BC1 and BC2. In the 2012 run, we adjusted the operational high voltage of the cathode planes to

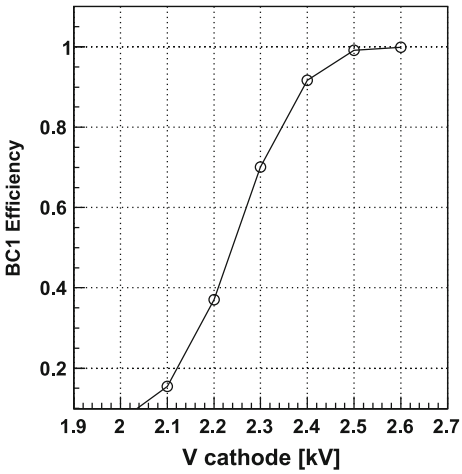

Fig. 2.8 Detection efficiency for a layer of the MWPC (BC1) as a function of high voltage of cathode planes

slightly lower values of 2.43–2.47 kV, whereas the value applied in the 2010 run was 2.51 kV. Figure 2.8 shows a efficiency curve for a layer of BC1. The detection efficiency becomes lower by a few percent; however, BC1 and BC2 have a redundant configuration of 12 layers. The low voltage operation had a merit because it let us handle an beam intensity of 1.7×10^6/spill, which is 1.7 times higher than that of the 2010 run.

2.3.1.2 Drift Chambers (BC3 and BC4)

In order to cope with several MHz counting rate at the downstream part of the beam spectrometer, a drift chamber with a sense wire pitch of 3 mm was fabricated and used as BC3. For BC4, a drift chamber with a sense wire pitch of 5 mm was recycled from the KEK-PS K6 beam line, because of a practical scheduling. Each drift chamber has 6 layers labeled like $[xx'uu'vv']$, where x stands for a vertical-wire plane and u and v are $\pm 15°$-tilted wire planes. In each pair plane, the sense wire position is shifted by a half of the cell size in order to solve the left/right ambiguity. Figure 2.9 shows a schematic view of the cell structure of BC3. For both BC3 and BC4, the sense wire is a gold-plated tungsten wire alloyed with 3 % rhenium with a diameter of 12.5 μm, and the field wire is a gold-plated copper-beryllium wire with a diameter of 75 μm. The cathode planes of BC3 are made of 12 μm thick mylar films coated with a 20 μm thick graphite paste, while the cathode planes of BC4 are made of 7.5 μm-thick kapton coated with 0.1 μm thick aluminum and 0.0025 μm thick chromium. The gas mixture was Ar (76 %) + iso-C_4H_{10} (20 %) + methylal (4 %) at the atmospheric pressure. For the front-end readout electronics, the same ASD as BC1 and BC2 was commonly used for BC3 and BC4. The timing information of BC3 and BC4 was digitized by a multi-hit TDC (AMT-2 [9]) mounted on the TKO boards.

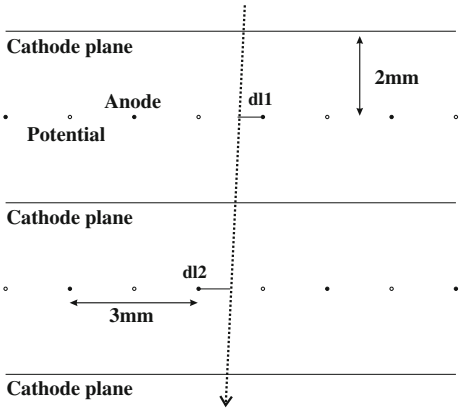

Fig. 2.9 Cell structure of the drift chamber BC3

Table 2.3 Specifications of the trigger counters

Name	Sensitive volume W × H × T (mm)	Etc.	PMT
GC	$340 \times 80^{\text{mirror}}$, 290^{gas}	iso-C_4H_{10}, $n = 1.002$ (1.5 atm)	R1250-03 (UV glass)
BH1	170 × 66 × 5	11 segments, BC420	H6524MOD
BH2	145(133) × 60 × 5	7 segments, BC420	H6524MOD
TOF	2240 × 1000 × 30	32 segments, BC410	H1949
AC	2040 × 1200 × 113	Silica aerogel, $n = 1.05$	R1584-02, Burle 8854
LC	2800 × 1400 × 40	28 segments, Lucite, $n = 1.49$	H1949, H6410

2.3.2 Trigger Counters for the Beam Spectrometer

Specifications of the trigger counters for the beam spectrometer (BH1, BH2, and GC) are listed in Table 2.3.

2.3.2.1 Beam Hodoscope Counters (BH1 and BH2)

The plastic scintillation hodoscope counters, BH1 and BH2, were used as trigger and time-of-flight counters. Beam particles were identified by the time of flight between BH1 and BH2 with a flight path of 10.4 m and with a time resolution of 0.2 ns (rms).

BH1 is a plastic scintillation counter located between GC and BC1. It is segmented into 11 vertical pieces of 5 mm thick plastic scintillators to balance the counting rate of each segment. A schematic view of BH1 is shown in Fig. 2.10. Each segment is overlapped with its adjacent segments by 1 mm to avoid a dead space. Photomultiplier tubes (PMTs) are connected on both ends of each segment and a high voltage power with a three-stage booster was supplied.

BH2 is a plastic scintillation counter located 120 cm upstream of the target. It is segmented into 7 vertical pieces of 5 mm thick plastic scintillators. A schematic view of BH2 is shown in Fig. 2.11. Each segment was overlapped with its adjacentsegments

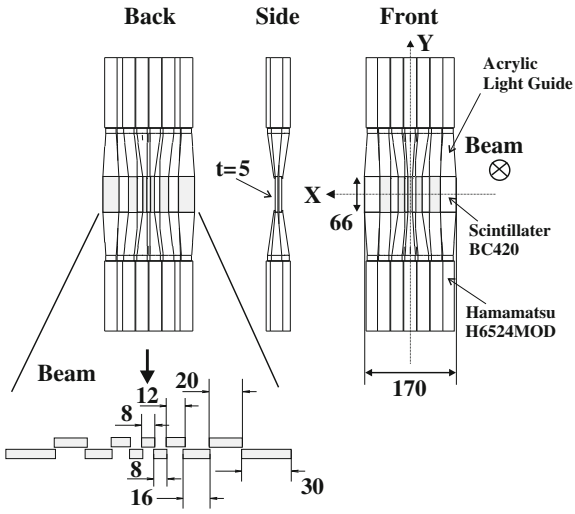

Fig. 2.10 Schematic view of the BH1 counter

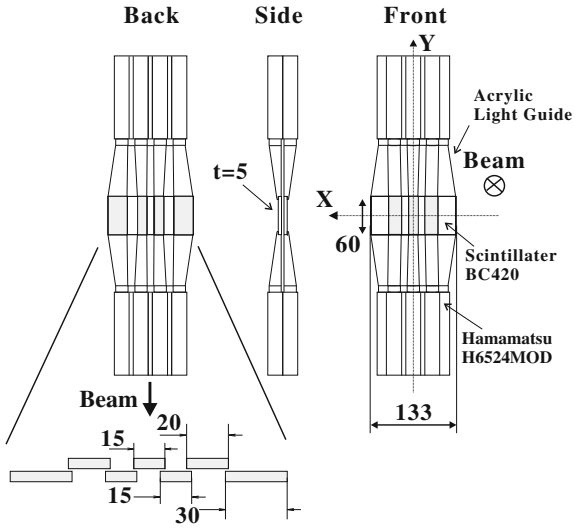

Fig. 2.11 Schematic view of the BH2 counter. Notice that each segment was not overlapped in the 2012 run

by 2 mm in the 2010 run. Since BH2 is placed between the beam spectrometer and the scattered-particle spectrometer, it should be made as thin as possible to minimize the energy loss straggling in the counter. Therefore, the segment configuration of BH2 was modified to no overlap before the 2012 run. PMTs are connected on both ends of each segment and a high voltage power with a three-stage booster was supplied. The BH2 hit timing defined the trigger timing and the time origin for any timing measurements.

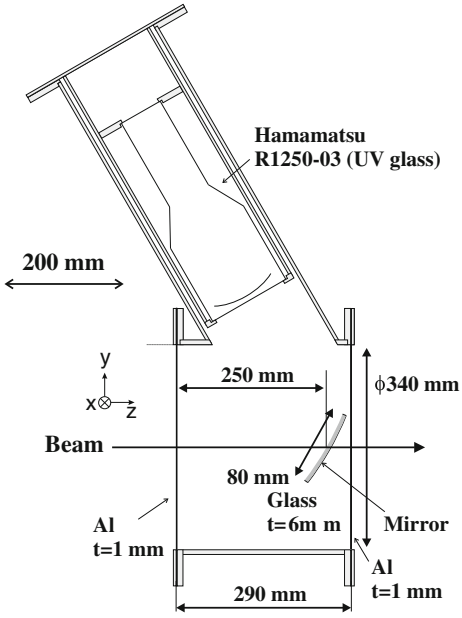

Fig. 2.12 Schematic view of the gas Cherenkov counter (GC)

2.3.2.2 Gas Cherenkov Counter (GC)

The gas Cherenkov counter, GC, was installed at the most upstream of the beam spectrometer to reject electrons/positrons in the momentum range above 1 GeV/c, where it is difficult to separate pions from electrons by the time-of-flight method. The Cherenkov radiator is an isobutane gas of 1.5 atm, which corresponds to a refractive index $n = 1.002$. A paraboloidal mirror is used as the reflector, which is made of aluminum evaporated on a borosilicate glass of 6 mm thickness. For the antioxidation of aluminum, the surface is coated with MgF_2, which is transmissive to ultraviolet photons. The Cherenkov photons are detected by a 5-inch PMT with a UV-transmissive window. Figure 2.12 shows a schematic view of GC. The measured number of photoelectrons was approximately 5 for electron beams of higher than 0.5 GeV/c. The detection efficiency was found to be 99.5 %, which was enough to reject electrons contaminating 10–20 % of the beam.

2.4 Superconducting Kaon Spectrometer

The Superconducting Kaon Spectrometer (SKS) comprises a superconducting dipole magnet with four sets of drift chambers (SDC1–SDC4) and three types of particle-identification counters (TOF, AC, and LC), as shown in Fig. 2.6. A remarkable feature of the spectrometer is a simultaneous realization of both a good momentum resolution of 2×10^{-3} (FWHM) and a large acceptance of 100 msr around 1 GeV/c. In addition, it keeps the flight path as short as 5 m, and has a powerful kaon identification ability.

Table 2.4 Specifications of the SKS spectrometer

Maximum field	2.5 T
Pole gap	49.75 cm
Momentum resolution	$\sim 2 \times 10^{-3}$ (FWHM)
Momentum acceptance	0.8–1.2 (0.75–1.0) GeV/c
Solid angle	100 msr
Angular coverage	$<5^\circ$ (vertical), $\lesssim 15^\circ$ (horizontal)
Flight path (Target–TOF)	$\sim$5 m

The SKS was originally designed and constructed for the study of Λ hypernuclei via the (π^+, K^+) reaction at the KEK K6 beam line [10]. The SKS magnet was moved to the J-PARC K1.8 beam line. The detectors were upgraded to increase the momentum acceptance and the high rate capability. Details of each detector are described in the following subsections.

Particle trajectories are reconstructed particle by particle using hit positions of the drift chambers together with a magnetic field map. The pole gap and the open space from SKS to SDC3 were occupied with helium bags to reduce multiple scattering effects. The magnet was excited at 2.5 T, and the field at the central region was monitored during the experimental period by an NMR probe [11]. The setup of SKS was slightly changed between 2010 and 2012 as follows: (i) the incident angle to the magnet face was adjusted from 30° to 15°; (ii) the AC detector was replaced with a new larger-size detector, while two small-size ACs were used in the 2010 run. Owing to these modifications, the momentum acceptance was changed from 0.75–1.0 GeV/c to 0.8–1.2 GeV/c, and the flat acceptance region increased. Specifications of the SKS spectrometer are summarized in Table 2.4.

2.4.1 Tracking Chambers for the SKS

Specifications of the tracking chambers for the SKS (SDC1–SDC4) are listed in Table 2.2.

2.4.1.1 Drift Chambers (SDC1 and SDC2)

The drift chambers, SDC1 and SDC2, were installed at the entrance of the SKS magnet. Since they are exposed to the beam, they are required to have the high rate capability at the same level as that of BC3 and BC4. SDC1 has 4 layers with a sense wire pitch of 3 mm, while SDC2 has 6 layers with a sense wire pitch of 5 mm. The structure of SDC1 is identical to that of BC3, and the structure of SDC2 is also

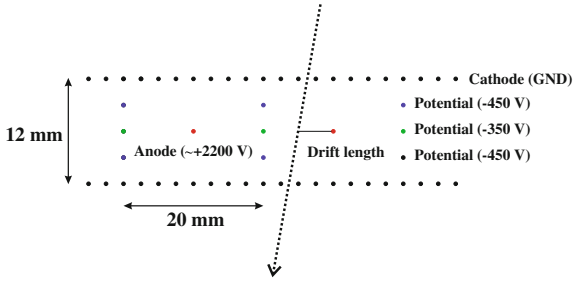

Fig. 2.13 Cell structure of the drift chambers, SDC3 and SDC4

similar to SDC1 except for the wire spacing and the size of the effective area. The gas mixture and readout electronics were the same as those of BC3 and BC4.

2.4.1.2 Drift Chambers (SDC3 and SDC4)

The drift chambers, SDC3 and SDC4, were installed at the exit of the SKS magnet. They have a large effective area of 2140 (horizontal) $\times$ 1140 (vertical) mm^2. Each chamber has 6 layers labeled as $[vxuvxu]$, where x stands for a vertical-wire plane and u and v are $\pm 30°$-tilted wire planes. The sense wire pitch is 20 mm. Figure 2.13 shows a schematic view of the cell structure. The sense wire is a gold-plated tungsten wire alloyed with 3 % rhenium with a diameter of 25 μm, and both the field and cathode wires are a gold-plated copper-beryllium wire with a diameter of 80 μm. The gas mixture was Ar (50 %) + C_2H_6 (50 %) at the atmospheric pressure. After passing through a front-end ASD, the timing information of SDC3 and SDC4 was digitized by a single-hit TDC module (TKO Dr.T II).

2.4.2 Trigger Counters for the SKS

Specifications of the trigger counters for the SKS are listed in Table 2.3.

2.4.2.1 Time-of-Flight Counter (TOF)

The time-of-flight counter, TOF, is a segmented plastic scintillation counter located at just the downstream of SDC4. TOF is horizontally segmented into 32 pieces of scintillators with a volume of $70^W \times 1000^H \times 30^T$ mm^3. Photomultiplier tubes (PMTs) are connected on both ends of each segment. A schematic view of TOF is shown in Fig. 2.14. A part of the segments (#1–10) installed at the high-momentum side were not used in the present experiment, because they are out of acceptance needed for the Θ^+ search. Scattered particles are identified by the time-of-flight measurement between TOF and BH2 in an offline analysis with a typical time resolution of 0.2 ns (rms).

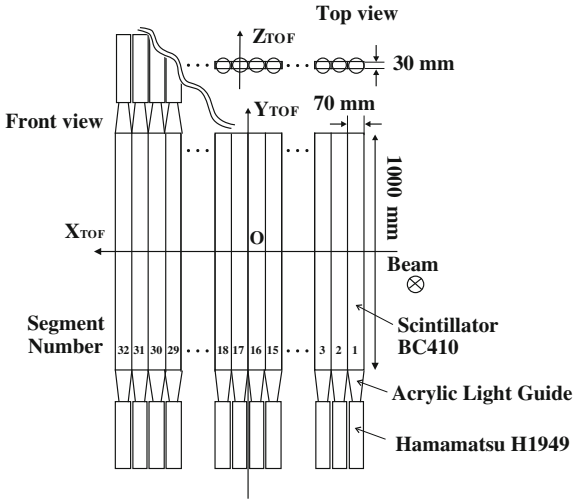

Fig. 2.14 Schematic view of the TOF counter

2.4.2.2 Aerogel Cherenkov Counter (AC)

The threshold-type silica aerogel Cherenkov counter, AC, was installed at just the downstream of TOF for pion veto at the trigger level. As shown in Fig. 2.15, pions with momenta above a threshold of 0.44 GeV/c emit the Cherenkov radiation in silica aerogels with a refractive index of 1.05. The sensitive volume of AC is $2040^W \times 1200^H \times 113^T$ mm^3. Figure 2.16 shows a schematic view of AC. For the uniform efficiency without dead space over a large sensitive area, AC is not segmented but of a large one-box type. The inner surfaces of the counter box are covered with aluminized mylar sheets. The Cherenkov photons are reflected by a mirror behind the radiator, and detected by 5-inch PMTs placed on both sides, which are sensitive to a single photon.

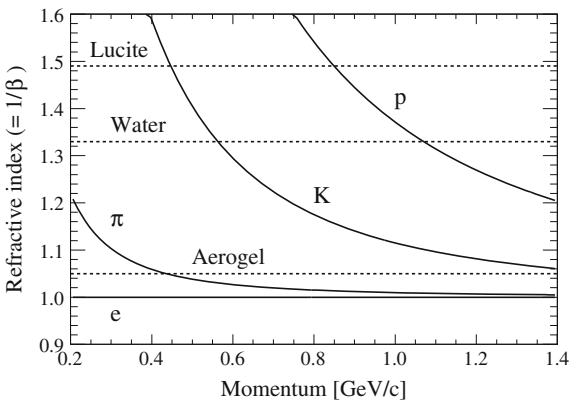

Fig. 2.15 Threshold refractive index for the Cherenkov radiation as a function of the particle momentum

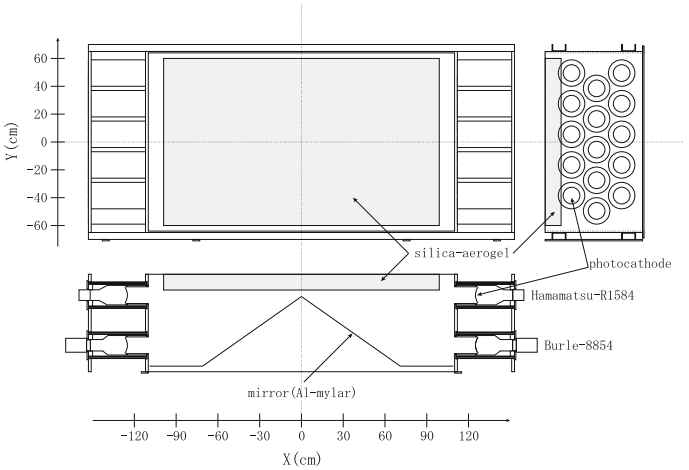

Fig. 2.16 Schematic view of the AC counter

In the present experiment, the AC efficiency for pions was 98 %, which deteriorated, locally due to support plates placed at $Y = \pm 200$ mm, and globally due to gaps of the aerogel tiles (see Appendix A). In addition, since the horizontal size of the AC radiator is smaller than that of TOF and LC, AC was inactive to the lowest momentum region, which corresponds to the last two segments of TOF (#31, 32).

2.4.2.3 Lucite Cherenkov Counter (LC)

The threshold-type lucite Cherenkov counter, LC, was installed just the downstream of AC. As shown in Fig. 2.15, protons with momenta below a threshold of 0.85 GeV/c are insensitive to the Cherenkov radiation in lucite (acrylic) with a refractive index of 1.49. LC is horizontally segmented into 28 vertical pieces of lucite bars with a volume of $100^W \times 1400^H \times 40^T$ mm^3. PMTs are connected on both ends of each segment. A schematic view of LC is shown in Fig. 2.17. In order to keep the uniform detection efficiency for various incident angles, a wavelength shifter (bis-MBS) is mixed in the lucite radiator by 10 ppm in weight, by which directional Cherenkov photons are diffused. Due to the scintillating radiation of the wavelength shifter, LC is slightly sensitive to protons even below the threshold. A part of the segments (#1–7) installed at the high-momentum side were not used in the present experiment, because they are out of acceptance needed for the Θ^+ search.

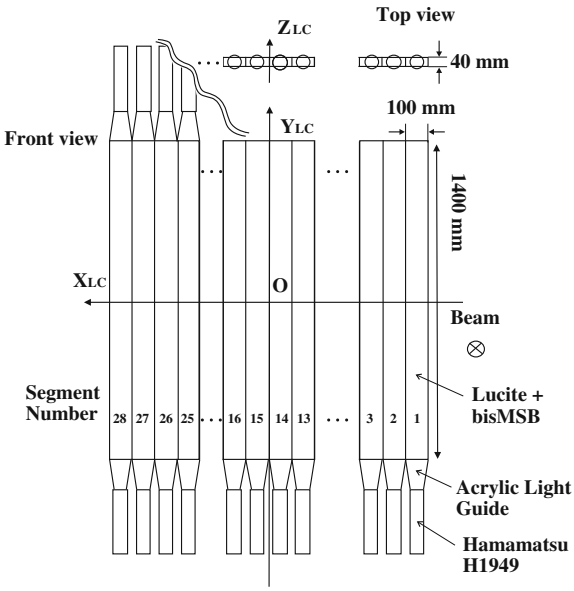

Fig. 2.17 Schematic view of the LC counter

2.5 Trigger

The trigger system was constructed to select (π, K) events efficiently from a large background produced through various pion-induced reactions, such as (π, π) and (π, p)[3] in addition to muons from beam pion decay, whose cross sections are typically two or three orders of magnitude larger than that of the (π, K) reaction. The trigger used only fast signals from the scintillation counters and the Cherenkov counters with a minimum trigger latency. The (π, K) trigger logic diagram is illustrated in Fig. 2.18.

The pion beam trigger was defined by the coincidence between BH1 and BH2 together with the anticoincidence of GC as

$$BEAM \equiv BH1 \times BH2 \times \overline{GC}.$$

For the scattered kaon trigger, TOF, AC and LC were used to eliminate scattered pions and protons as $TOF \times \overline{AC} \times LC$. In addition, the matrix trigger (MTX), which is a coincidence matrix between the TOF and LC segments, was adopted to reject the particles coming not from the target but from detector frames. As shown in Fig. 2.19, particles passing through the SKS magnet make a correlation in hit segments between

[3] Since the present experiment aimed at the $\pi^- p \to K^- X$ reaction, (π, p) events came into detection only in calibration runs using the $\pi^{\pm} p \to K^+ \Sigma^{\pm}$ reactions.

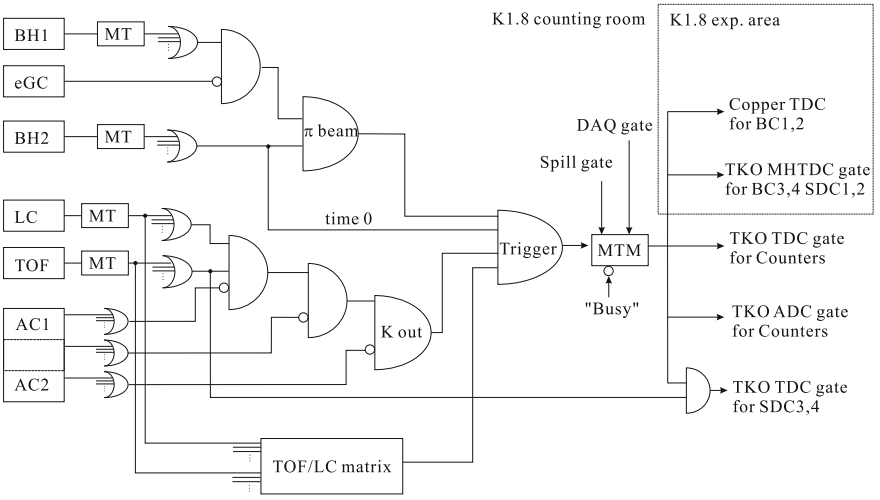

Fig. 2.18 (π, K) trigger logic diagram

TOF and LC, which appears from the lower left to the top right corner on the figure. The open boxes represent kaon events identified by the SKS tracking, whereas entire triggered events are shown in a dark scale. A locus on the top left corner originates from particles generated by the beam hitting the SDC3 frame. Such events were rejected by the matrix trigger, which accepted the region surrounded by the red lines. The trigger rate was reduced to 1/2 using the matrix trigger. The matrix coincidence was implemented using an FPGA module (TUL-8040 [12]). Then, the (π, K) trigger was defined as

$$PIK \equiv BEAM \times TOF \times \overline{AC} \times LC \times MTX.$$

In order to study inefficiency of the matrix trigger, the (π, K) trigger data without the matrix coincidence were simultaneously acquired at a 1/10 prescaled rate. A typical trigger rate for the $\pi^- p \to K^- X$ data was 600 per spill at a beam rate of 1.7×10^6 per spill.

2.6 Data-Acquisition System

For the data acquisition (DAQ) system of the K1.8 experimental area, we adopted a new network-oriented readout module, KEK-VME/COPPER [13], as well as conventional readout systems such as VME, CAMAC, and TKO [14]. These different DAQ subsystems were integrated by a network-based DAQ software (HDDAQ) [15]. Today, networking communication among the inter-subsystem has become the most common method. Data from each subsystem are gathered by controllers having network interfaces with the TCP/IP protocol. However, since the network is an asynchronous communication, the event identification becomes an issue. Therefore, the

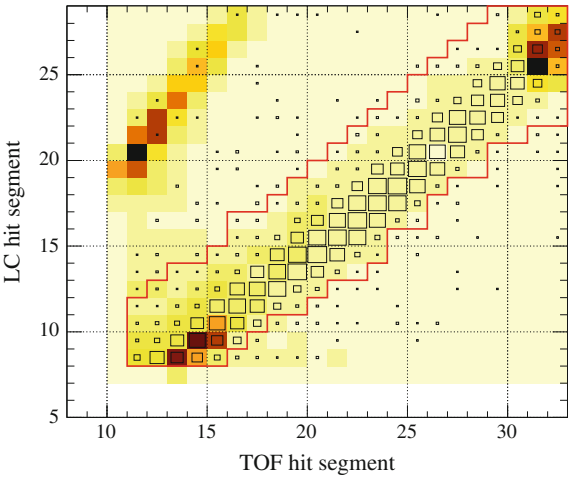

Fig. 2.19 Hit segment correlation between TOF and LC taken with the (π, K) trigger without the matrix trigger. Entire triggered events are shown in a *dark scale*, while the *open boxes* represents Kaon events identified by the SKS tracking. The *red line* indicates the region accepted by the matrix trigger

master trigger module (MTM) and the receiver module (RM) were developed for the experiment [15]; the system distributes an event tag to each subsystem. The entire scheme of the DAQ system is illustrated in Fig. 2.20.

MTM manages functions controlling the DAQ system such as "trigger", "clear", "busy", and the event tag. These information are distributed via the Ethernet cable from MTM to RM of each subsystem. The trigger signal is used as a start/stop timing of TDC and a gate of ADC. The busy signals issued in the subsystems veto the next trigger on MTM. The event tag is decoded in RMs and embedded in an event packet. The tags embedded in the data structure are checked at the beginning of the data analysis. After finishing the analog-to-digital conversion, the data are transferred to an event builder.

HDDAQ is a network-based DAQ software consisting of several DAQ components, i.e., Front-end (FE), Event Builder (EB), Event Distributor (ED), and Recorder (RD). The FE process is running on each front-end computer, while other components are running on the control DAQ server. These components have two different paths, namely, "data path" and "message path", with the TCP/IP protocol. The data path is a pathway to individual detector data, while all components are controlled via the message path. The FE process reads data from each readout electronics and transmits them to the EB process. The EB process collects data fragments from FEs and builds an event packet event by event. This packet is sent to the ED process, which distributes it to downstream processes such as RD and online monitors. The RD process reads data from ED and stores them to storage devices with compression.

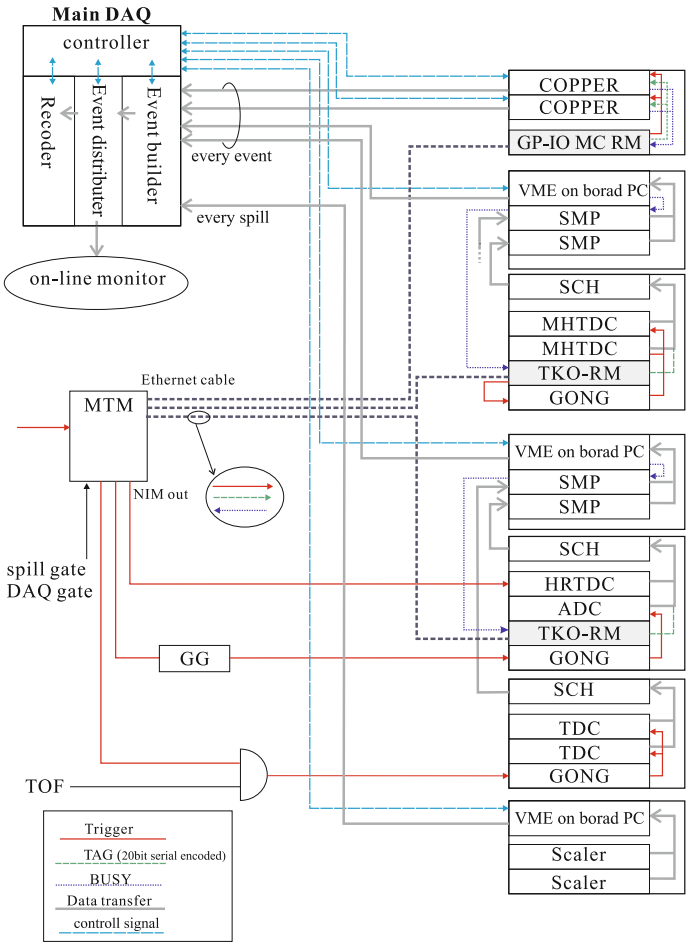

Fig. 2.20 Schematic diagram of the data-acquisition system

2.7 Liquid Hydrogen Target

We used a liquid hydrogen (LH_2) target with a thickness of 0.85 g/cm^2. Figure 2.21 shows a schematic view of the target system. The hydrogen vessel size was 67.8 mm in diameter and 120 mm in length along the beam direction. The hydrogen vessel was made of a 0.30 mm thick PET (polyethylene terephthalate) for the cylinder part, and a 0.25 mm thick mylar for the end cap part. The windows of the target vacuum chamber were made of a 0.25 mm thick mylar. The hydrogen target was cooled by a heat exchanger and continuous flow of cold helium gas from a liquid helium container. The stability of the pressures and temperature was kept by a feedback

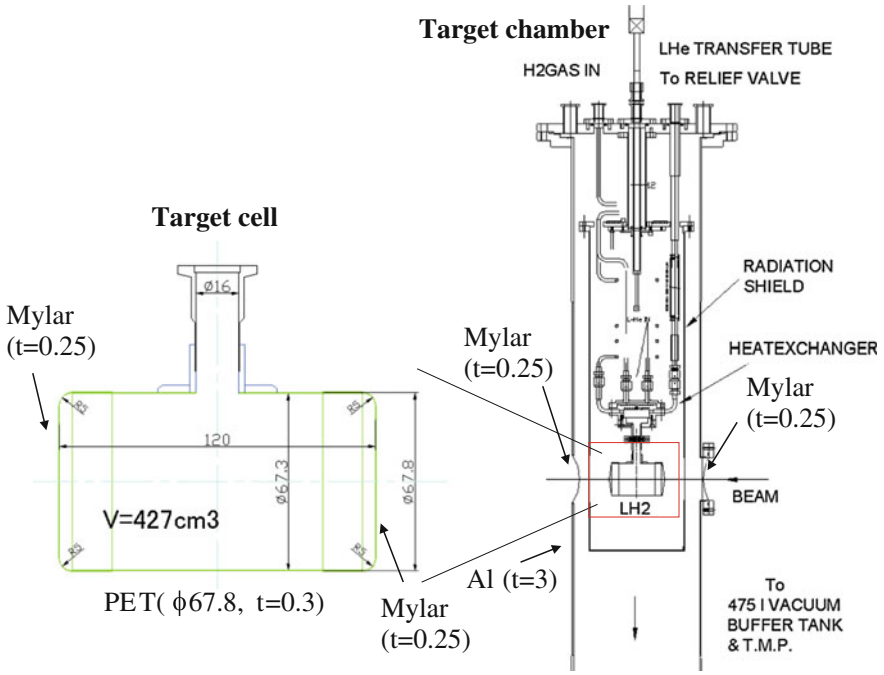

Fig. 2.21 Schematic view of the liquid hydrogen target. All units are in mm

Table 2.5 Specifications of the liquid hydrogen target

Vessel size	$\phi 67.8 \times 120$ mm
Vessel material	PET (cylinder), Mylar (end cap)
Average thickness	0.30 mm (cylinder), 0.25 mm (end cap)
Target chamber	Aluminum: $t = 3$ mm, $\phi 270$ mm
Chamber window	Mylar: $t = 0.25$ mm
LH_2 thickness	0.85 g/cm^2 (0.0708 g/cm^3 $\times$ 12 cm)
Density fluctuation	$<3 \times 10^{-5}$

system of the He flow, and monitored during the experimental period. The density fluctuation was found to be less than 3×10^{-5}. Specifications of the liquid hydrogen target are summarized in Table 2.5.

2.8 Data Summary

Table 2.6 shows the data summary of the E19 experiment taken in both the previous and present runs in 2010 and 2012, respectively. For the Θ^+ search data, the $\pi^- p \to K^- X$ reaction at 1.92 and 2.01 GeV/c were accumulated in the 2010 and 2012 runs, respectively. In the present data, 8.1×10^{10} π^- beams were irradiated on the liquid hydrogen target, which is almost the same amount as the previous data of 7.8×10^{10}. Empty target data with the empty vessel instead of the liquid hydrogen target were also taken in order to estimate a background contamination from surrounding materials and the vertex cut efficiency. For the momentum calibration of the spectrometers, the following two kinds of calibration data were used:

Σ production data The outgoing kaon momenta in the $\pi^- p \to K^- \Theta^+(1530)$ reaction at 2.01 GeV/c are around 1.0 GeV/c at forward angles. The kinematics of the outgoing kaons in the $\pi^- p \to K^+ \Sigma^-$ reaction at 1.46 GeV/c is similar to that in the $\pi^- p \to K^- \Theta^+(1530)$ reaction at 2.01 GeV/c (see Fig. 3.25 in detail). Therefore, the $\pi^- p \to K^+ \Sigma^-$ reaction at 1.46 GeV/c are useful for various calibration. In the same manner, the $\pi^\pm p \to K^+ \Sigma^\pm$ reactions at 1.38 GeV/c correspond to the $\pi^- p \to K^- \Theta^+(1530)$ reaction at 1.92 GeV/c. The validity of the analysis is examined by using the missing-mass peak and the cross section of the Σ hyperons.

Beam-through data A low-momentum pion beam of 0.75–1.38 GeV/c can directly pass through the both spectrometers. This kind of data is called $\pi^\pm$ beam-through data. The data were acquired at several momentum settings between 0.75 and 1.38 GeV/c with both positively and negatively charged beams.

In the subsequent chapters, the analysis and result of the 2012 data are presented.

Table 2.6 Summary of the E19 experimental data

Reaction	Beam momentum (GeV/c)	Target	Number of pions on target	
			2010 data	2012 data
$\pi^- p \to K^- X$	1.92/2.01	LH_2	7.8×10^{10}	8.1×10^{10}
Empty run	1.92/2.01	Empty	4.6×10^9	4.1×10^9
$\pi^+ p \to K^+ \Sigma^+$	1.38	LH_2	2.9×10^9	8.5×10^8
$\pi^- p \to K^+ \Sigma^-$	1.38	LH_2	1.2×10^{10}	3.8×10^9
$\pi^- p \to K^+ \Sigma^-$	1.46	LH_2	–	8.7×10^9
$\pi^\pm$ beam-through	0.75–1.38	Empty	–	–

The 2010 and 2012 data represent the previous and present data, respectively. The first row is the Θ^+ search data, while the others are calibration data

References

1. T. Takahashi et al., Prog. Theor. Exp. Phys. **2012**, 02B010 (2012)
2. S. Nagamiya, Prog. Theor. Exp. Phys. **2012**, 02B001 (2012)
3. K. Agari et al., Prog. Theor. Exp. Phys. **2012**, 02B009 (2012)
4. T. Koseki et al., Prog. Theor. Exp. Phys. **2012**, 02B004 (2012)
5. Digital Teslameter 151 (DTM-151), Group3 Technology. http://www.group3technology.com/index.php/products/product/digital-teslameter-151
6. T. Hasegawa, Ph.D. thesis (University of Tokyo, INS-IM-15, 1994)
7. H. Hotchi, Ph.D. thesis (University of Tokyo, KEK Report 2000–3, 2000)
8. O. Sasaki, M. Yoshida, I.E.E.E. Trans, Nucl. Sci. **46**, 1871 (1999)
9. Y. Arai, Nucl. Instrum. Method. A **453**, 365 (2000)
10. T. Fukuda et al., Nucl. Instrum. Method. A **361**, 485 (1995)
11. EFM-3000AX, Echo Electronics. http://echo-denshi.co.jp/nmr_magnetic.htm
12. Tohoku Universal Logic Module. http://lambda.phys.tohoku.ac.jp/~takahasi/TUL-8040/
13. Y. Igarashi et al., IEEE Trans. Nucl. Sci. **52**, 2866 (2005)
14. KEK Data Acquisition Development Working Group, KEK Report 85–10 (1985)
15. Y. Igarashi et al., IEEE Trans. Nucl. Sci. **57**, 618 (2010)

Chapter 3
Data Analysis

3.1 Outline

The Θ^+ was searched for in a missing mass spectrum of the $\pi^- p \to K^- X$ reaction. The missing mass, M_X, is calculated in the laboratory frame as follows:

$$M_X = \sqrt{(E_\pi + m_p - E_K)^2 - (p_\pi^2 + p_K^2 - 2p_\pi p_K \cos\theta)}, \tag{3.1}$$

where E_π and p_π are the energy and momentum of a beam pion, respectively; E_K and p_K are those of a scattered kaon; m_p is the mass of a target proton; and θ is the scattering angle. Thus, there are three kinematic variables to be measured: p_π, p_K and θ.

The procedure of the missing mass reconstruction was as follows:

1. event selection by using counter information,
2. momentum reconstruction for beam and scattered particles,
3. particle identification of kaons,
4. reconstruction of the scattering angle and the vertex point, and
5. calculation of the missing mass.

Details of the procedure are described in Sects. 3.2, 3.3 and 3.4.

The calibration procedures applied in the present analysis are described in Sects. 3.6 and 3.7. Analyses on both the momentum scale calibration and the momentum resolution are performed by using the dedicated calibration data: the $\Sigma^\pm$ production data and the $\pi^\pm$ beam-through data.

The method of the cross section calculation is described in Sect. 3.8. The cross section is calculated with experimental efficiency and acceptance correction. The validity of the method is examined through the $\Sigma^\pm$ production cross sections in Sect. 3.9.

M. Moritsu, *Search for the Pentaquark Θ^+ via the $\pi^- p \to K^- X$ Reaction at J-PARC*, Springer Theses, DOI 10.1007/978-981-10-0012-6_3

3.2 Analysis of Beam Particles

3.2.1 Beam Particle Identification

The beam particles were identified by using the time of flight between BH1 and BH2 with a flight length of 10.4 m. Figure 3.1 shows a typical time-of-flight spectrum for a 2-GeV/c π^- beam, where the π peak position was adjusted to be zero in the horizontal axis. The same spectrum in a logarithmic scale is shown in the inset. The continuous background around the peak was due to accidental hits on BH1 and BH2. Neither kaons (+1.0 ns) nor antiprotons (+3.5 ns) are seen because their production and survival rate to the target position is two orders of magnitude smaller than that of pions. Furthermore, the electrostatic separators could reject protons in case of π^+ beams. A contamination rate of muons, which con not be separated from pions by the time-of-flight method, are described in Sect. 3.8.1. Electron contamination in the beam trigger was negligibly small as described in Sect. 2.3.2. The time resolution of the time-of-flight measurement is 0.2 ns (rms). The cut positions were set at ± 1 ns with the efficiency of 96.8 %.

3.2.2 Beam Track Reconstruction

The beam momentum was reconstructed from the BC1–4 data as follows. First, straight-line tracks were defined locally at the entrance and exit of the QQDQQ magnets by the linear least-squares fitting. In the MWPC (BC1 and BC2) tracking, hits on adjoining wires within a proper timing of ± 10 ns were made up as a cluster hit and the weighted-mean position of the cluster was used. In the drift chamber (BC3 and BC4) tracking, the drift time was converted to the drift length and the pair-plane information was used to solve the left/right ambiguity. Figure 3.2 shows typical χ^2

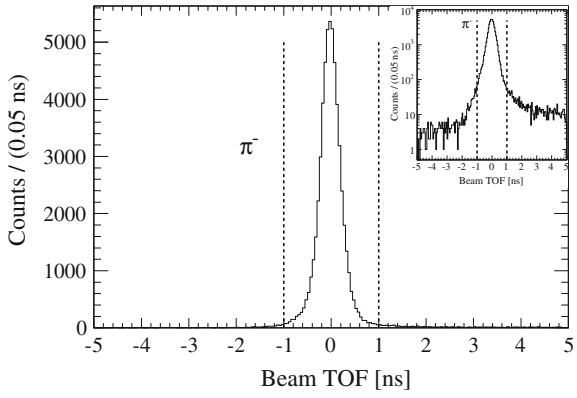

Fig. 3.1 Time-of-flight spectrum for a 2-GeV/c π^- beam. The *inset* shows the same spectrum in a logarithmic scale. The selected time window is indicated by the *dashed lines*

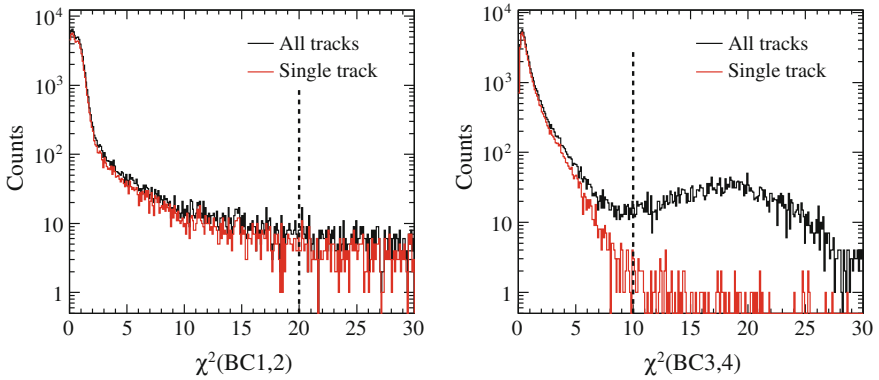

Fig. 3.2 χ^2 distributions of the local *straight-line* tracking of BC1 and BC2 (*left*), and BC3 and BC4 (*right*). The *red histograms* denote single track events. The *dashed lines* indicate the χ^2 cut positions

distributions for the local straight-line tracking. The red histograms represent single track events, while the black histograms represent all tracks including multitrack events. The multitrack event consists of a triggered (true) track and subsequent (false) tracks. For the drift chambers (Fig. 3.2 right), the single track events show a reasonable χ^2 distribution, whereas the χ^2 distribution for multitrack events shows a bump structure around 20, because the subsequent tracks do not have a proper drift time. Most of the subsequent tracks were excluded by setting the cut position at $\chi^2 = 10$ without decreasing the tracking efficiency.

Next, the straight-line tracks determined at the entrance and exit of the QQDQQ magnets were connected using a transport matrix (third-order in horizontal and second-order in vertical) calculated by ORBIT [1]:

$$\mathbf{X}_{out} = \mathcal{M}(\mathbf{X}_{in}), \tag{3.2}$$

where $\mathbf{X}_{\rm in}$ and $\mathbf{X}_{\rm out}$ are vectors that represent positions, directions and momentum (p) of the particle such as $\mathbf{X} = \left(x, \frac{dx}{dz}, y, \frac{dy}{dz}, p\right)$; the local (x, y, z) coordinate was defined as shown in Fig. 3.3. VI and VO stand for reference planes in which $\mathbf{X}_{\rm in}$ and $\mathbf{X}_{\rm out}$ are defined, respectively. The operator $\mathcal{M}$ denotes the transport matrix. The particle trajectory was determined by minimizing the following χ^2 value:

$$\chi^2_{\rm K1.8} \equiv \frac{1}{n-5}\left[\sum_{i=1}^{12} H_i \left(\frac{P_i - f_i(\mathbf{X}_{\rm in})}{w_i}\right)^2 + \sum_{i=13}^{24} H_i \left(\frac{P_i - g_i(\mathbf{X}_{\rm out})}{w_i}\right)^2\right] \tag{3.3}$$

$$n = \sum_{i=1}^{24} H_i, \tag{3.4}$$

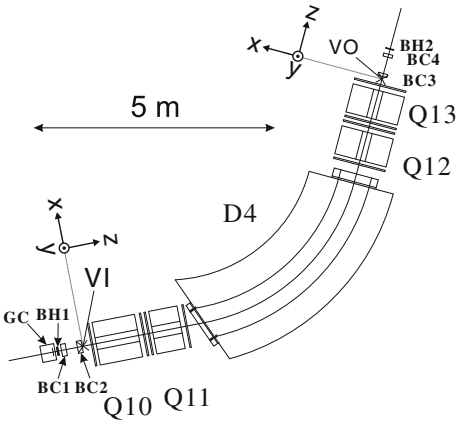

Fig. 3.3 Reference planes *VI* and *VO* in which the local coordinates are defined. *VI* is defined at a 13-cm upstream of the entrance of *Q10*, while *VO* is defined at a 13-cm downstream of the exit of *Q13*

$$H_i = \left\{ \begin{array}{ll} 1 & \text{if } i\text{th plane has a hit,} \\ 0 & \text{if } i\text{th plane has no hit} \end{array} \right\}, \tag{3.5}$$

where P_i and w_i denote the hit position and resolution of the ith plane in BCs, respectively. The calculated position by the transport matrix at the ith plane is denoted by $f_i(\mathbf{X}_{\text{in}})$ or $g_i(\mathbf{X}_{\text{out}})$. The minimization was done for each combination of the straight-line tracks by using MINUIT [2] with respect to $\mathbf{X}_{\text{in}}$ as parameters.

Figure 3.4 left shows a typical $\chi^2_{\text{K1.8}}$ distribution for a 2-GeV/c π^- beam. Events with χ^2 less than 30 were accepted as good tracks. Figure 3.4 right shows a momentum distribution for a 2-GeV/c π^- beam. The central momentum was found to be

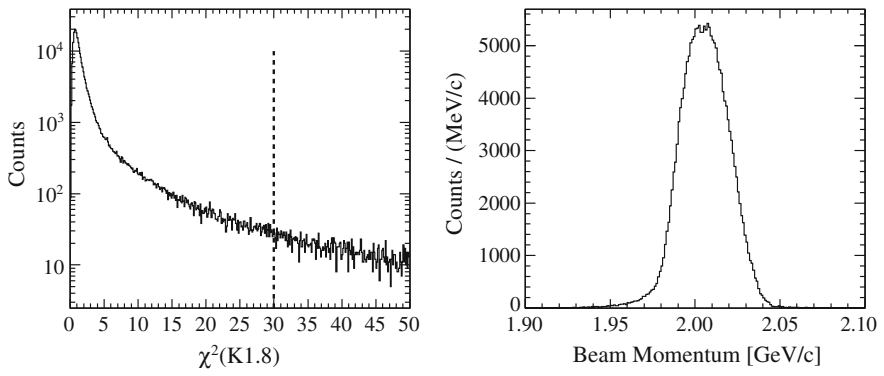

Fig. 3.4 *Left* $\chi^2_{\text{K1.8}}$ distribution of the K1.8 tracking for a 2-GeV/c beam. The *dashed line* indicates the cut position. *Right* Reconstructed beam momentum distribution for a 2-GeV/c beam

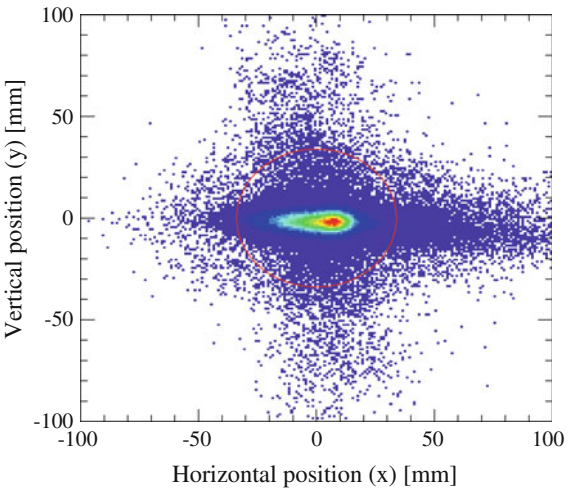

Fig. 3.5 Beam profile at the target position in the Θ^+ search data at 2 GeV/c. The (x, y, z) coordinate is defined in the right-handed system with the z-axis as the nominal beam direction. The beam profile peaks at $(x, y) = (7\text{ mm}, -2\text{ mm})$ with $(\sigma_x, \sigma_y) = (11\text{ mm}, 4\text{ mm})$. The horizontal profile is skew toward *right* in this figure. The *red circle* indicates the target vessel with a diameter of 67.8 mm

2.01 GeV/c[1] and the momentum spread was 1 % in rms. In the present analysis, events including more than two beam tracks were discarded, which corresponds to 6 % of the total events. Figure 3.5 shows a typical beam profile at the target position in the Θ^+ search data at 2 GeV/c. The beam was irradiated to the LH_2 target with a typical targeting efficiency of 96 %. Since 2 GeV/c is the maximum momentum of the K1.8 beam line, the horizontal profile was skew toward right in the figure.

3.3 Analysis of Scattered Particles

3.3.1 Scattered-Particle Track Reconstruction

The momentum of a scattered particle was reconstructed from the SDC1–4 data as follows. First, straight-line tracks were defined locally at the entrance and exit of the SKS magnet by the linear least-squares fitting. The same local tracking method as for BC3 and BC4 was applied both for SDC1 and SDC2 and for SDC3 and SDC4. For SDC3 and SDC4, all combinations of the left/right ambiguity were examined because they do not have the pair-plane structure. Figure 3.6 shows typical χ^2 distributions for the local straight-line tracking. The red histograms denote single track events. In the χ^2 distribution for the local tracking of SDC1 and SDC2 (Fig. 3.6 left), a bump around 30–40 caused by multitrack events was observed due to the same reason as for BC3 and BC4. Most of the subsequent tracks were excluded by setting the cut position at $\chi^2 = 20$ without decreasing the tracking efficiency. In the χ^2 distribution

[1]This value is the one obtained after applying the momentum scale calibration described in Sect. 3.6.3.

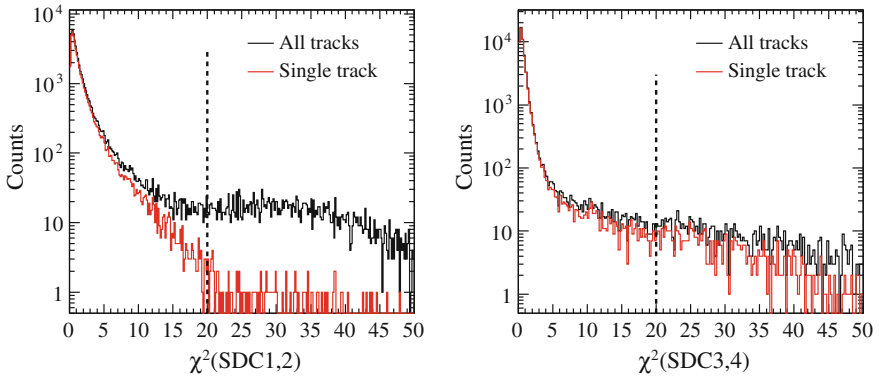

Fig. 3.6 χ^2 distributions of the local straight-line tracking of SDC1 and SDC2 (*left*), and SDC3 and SDC4 (*right*). The *red histograms* denote single track events. The *dashed lines* indicate the χ^2 cut positions

for the local tracking of SDC3 and SDC4 (Fig. 3.6 right), multitrack events were rarely observed, because the beam does not pass through the chambers. In addition to the χ^2 cut, a position matching between the hit segment of TOF and the local track of SDC3 and SDC4 was checked.

Next, the momentum of the scattered particle was determined by reconstructing the trajectory from the chamber hit positions. The trajectory was reconstructed with the fast Runge–Kutta method [3] using a magnetic field map of SKS. The magnetic field map was calculated by ANSYS [4] using the finite element method. The trajectory and the momentum were iteratively optimized by minimizing the following χ^2 value:

$$\chi^2_{\mathrm{SKS}} \equiv \frac{1}{n-5}\sum_{i=1}^{n}\left(\frac{x_i^{\mathrm{tracking}} - x_i^{\mathrm{data}}}{w_i}\right)^2, \tag{3.6}$$

where n is the number of the chamber planes with a hit; x_i^{tracking} and x_i^{data} are the hit positions on the ith hit plane in the tracking and the data, respectively; and w_i is the position resolution of the ith hit plane. The fitting parameters were the momentum (p), the horizontal (x) and vertical (y) positions and their derivatives (dx/dz, dy/dz) at the target position. The convergence criterion in the iteration was $\delta\chi^2 = (\chi^2_{k+1} - \chi^2_k)/\chi^2_k < 2 \times 10^{-4}$, where χ^2_k is the tracking χ^2 for the kth iteration.

Figure 3.7 shows a typical χ^2_{SKS} distribution for scattered proton events in the calibration data. Events with χ^2 less than 30 were accepted as good tracks. The tracking efficiency is discussed in Sect. 3.8.1.

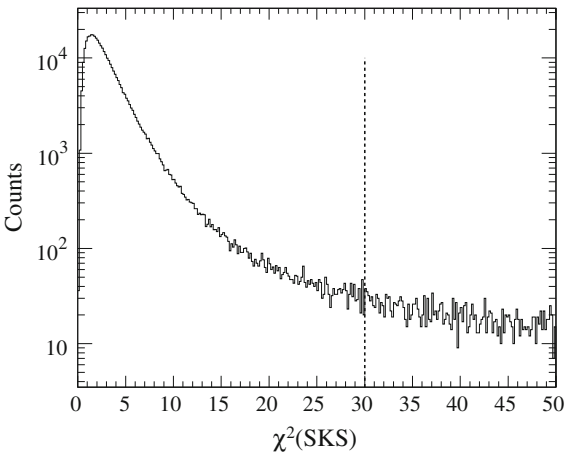

Fig. 3.7 χ^2_{SKS} distribution of the SKS tracking for scattered proton events contaminating the Σ^- production data. The *dashed line* indicates the cut position

3.3.2 Scattered-Particle Identification

After the SKS tracking, the mass of a scattered particles, M_{scat}, was calculated as

$$M_{\mathrm{scat}} = \frac{p}{\beta}\sqrt{1-\beta^2}, \tag{3.7}$$

where β is the velocity of a scattered particle obtained from the time-of-flight and the flight path length between BH2 and TOF; and p is the momentum obtained from the SKS tracking. In the (π, K) trigger events, a main source of background in scattered particles were fast protons which fired LC and pions which were not vetoed by AC due to its inefficiency. Figure 3.8 shows typical squared-mass (M^2_{scat}) distributions in the Θ^+ search data and the Σ^+ production data. Negatively charged particles are detected in the Θ^+ search data, while positively charged particles are detected in the Σ production data. The kaon cut region was determined in order to reduce contamination from other particles without decreasing the efficiency described below. The kaon cut region is indicated in the spectra: $0.15 < M^2_{\mathrm{scat}} < 0.40$ $(\mathrm{GeV}/c^2)^2$.

3.3.2.1 Kaon Identification and Pion Contamination

In the squared-mass distribution, a peak for each particle has a tail ascribed to the time walk effect of TOF and time lags among the TOF segments. Figure 3.9 shows a mass-squared distribution in a logarithmic scale. In order to estimate the kaon identification efficiency, two types of assumptions were considered:

(a) Assume that the low-mass tail of the kaon peak is subjected to the Gaussian distribution. This may slightly underestimate the total amount of kaons, since a low-mass tail tends to be longer than the Gaussian distribution.

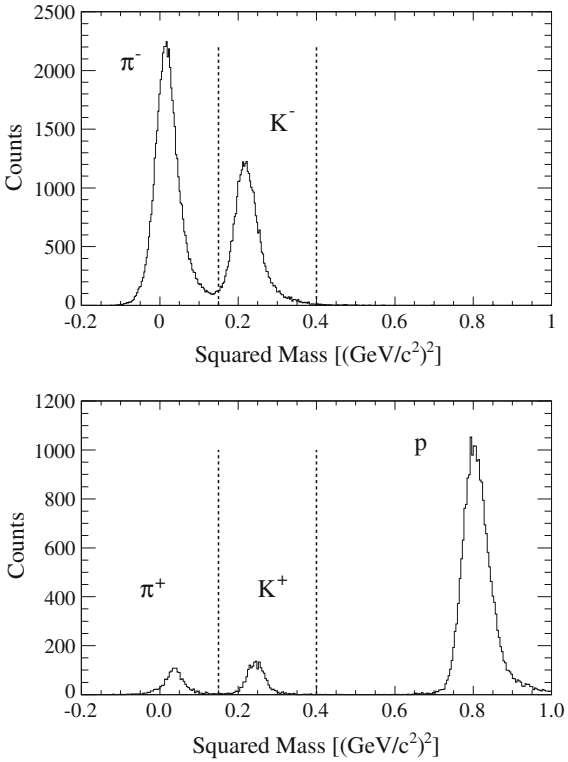

Fig. 3.8 Squared mass distribution for scattered particles in the Θ^+ search data (*top*) and the Σ^+ production data (*bottom*). A momentum range of 0.9–1.1 GeV/c is selected in the *top figure*. The vertex cut and the scattering angle selection of 2–15° have been applied in *both figures*. The *dashed lines* indicate the kaon selection gate

(b) Assume that the low-mass tail shape of the kaon peak is the same as that of the high-mass tail. This may slightly overestimate the total amount of kaons, since a low-mass tail tends to be shorter than a high-mass tail.

A result of the peak fittings for pions and kaons by using the Gaussian function is shown in Fig. 3.9. The kaon identification efficiency for $0.15 < M^2_{\rm scat} < 0.40$ $({\rm GeV}/c^2)^2$ was calculated according to the assumption (a) or (b). The mean value between the results from (a) and (b) was adopted, and the difference of the two results was attributed to the systematic uncertainty. In order to estimate the pion contamination fraction in the kaon region, the high-mass tail of the pion peak was fitted by using the exponential function as shown in Fig. 3.9. The systematic uncertainty was estimated from the fitting range dependence.

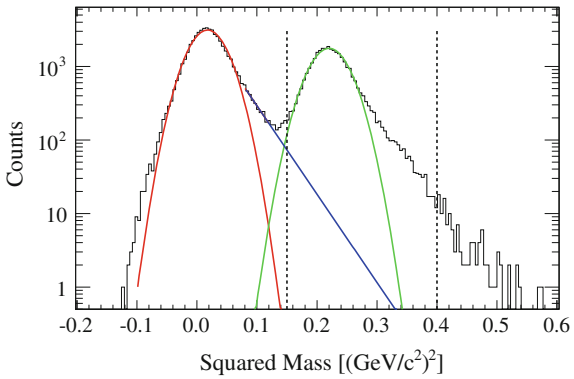

Fig. 3.9 Squared mass distribution for scattered particles with fitting results used for the efficiency evaluation. The distribution is taken from the Θ^+ search data in a momentum range of 0.9–1.1 GeV/c. The *red* and *green* Gaussian functions were obtained by fitting the pion and kaon peaks, respectively. The *blue* exponential function was obtained by fitting the high-mass tail of the pion peak. The *dashed lines* indicate the kaon selection gate

Moreover, the squared-mass distribution depends on the momentum as shown in Fig. 3.10. The mass resolution deteriorates with increase of the momenta. Figure 3.11 shows the kaon identification efficiency and the pion contamination fraction estimated for some momentum ranges. With the increase of the momenta, the efficiency decreases whereas the contamination increases. The high contamination fraction in the momenta of 0.8–0.9 GeV/c is caused by the large pion contribution due to a trigger bias shown in Fig. 3.10. The Θ^+ search region in the missing mass is 1500–1560 MeV/c^2 which corresponds to the kaon momentum range of 0.9–1.1 GeV/c. In this momentum range, the kaon identification efficiency was estimated to be 95.5 ± 2.0 % and the pion contamination fraction was 1.9 ± 1.0 %.

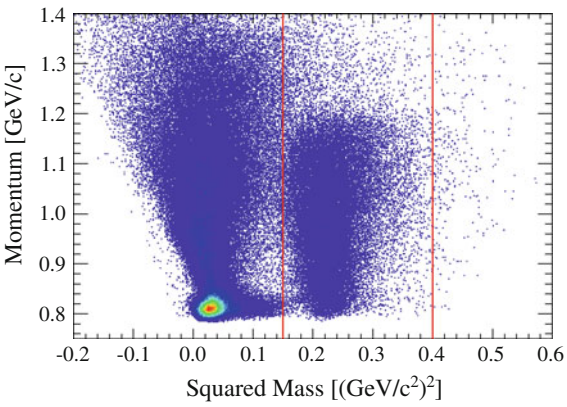

Fig. 3.10 Two-dimensional plot of the squared mass versus the momentum for scattered particles in the Θ^+ search data. The large contribution of pions around 0.8 GeV/c is attributed to a trigger bias due to the AC inactive region. The *red lines* indicate the kaon selection gate

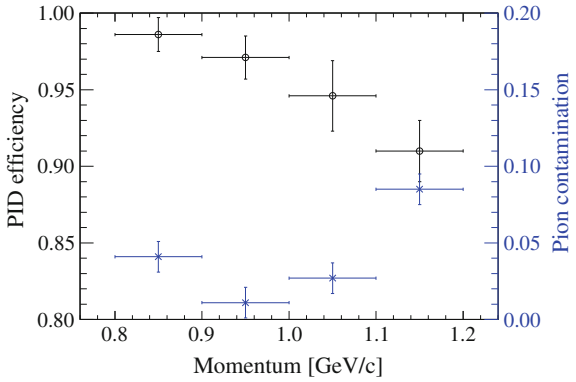

Fig. 3.11 Kaon identification efficiency and pion contamination fraction for each momentum range. The *black circles* denote the kaon identification efficiency (left axis), while the *blue crosses* denote the pion contamination fraction in the kaon region (right axis). The vertical error bars denote the systematic uncertainty described in the text

3.4 Scattering Angle and Vertex Reconstruction

The scattering angle and the reaction vertex were reconstructed from two tracks: the local straight-line track obtained from BC3 and BC4 hit positions and the track obtained from the momentum reconstruction in SKS. The relative geometry between the beam and SKS spectrometers was adjusted by using the beam-through data. Figure 3.12 shows distributions of the horizontal and vertical angle difference between the two tracks at the target position in the 1.1-GeV/c π^- beam-through data. The horizontal and vertical angular resolutions were estimated to be 2.2 and 2.7 mrad in rms, respectively. The vertical resolution was worse than the horizontal one because of the wire configuration of the drift chambers.

The reaction vertex point was defined as the closest point between the two tracks. In the present analysis, the forward scattering angle less than 2° was excluded because of the following two reasons:

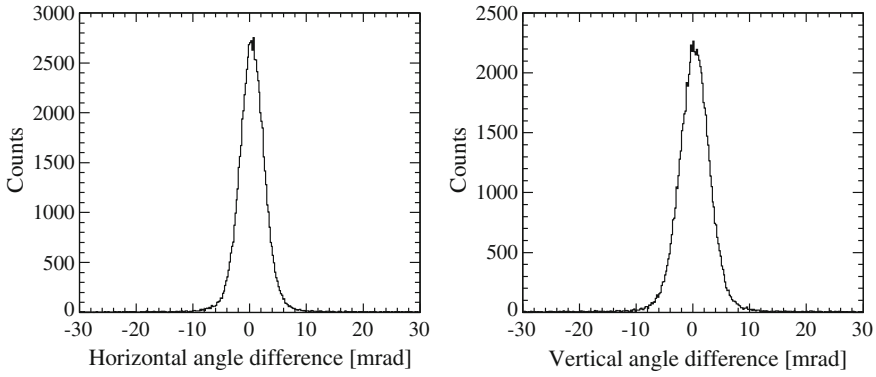

Fig. 3.12 Distributions of the horizontal (*left*) and vertical (*right*) angle difference between the beam track and the SKS track at the target position in the 1.1-GeV/c π^- beam-through data

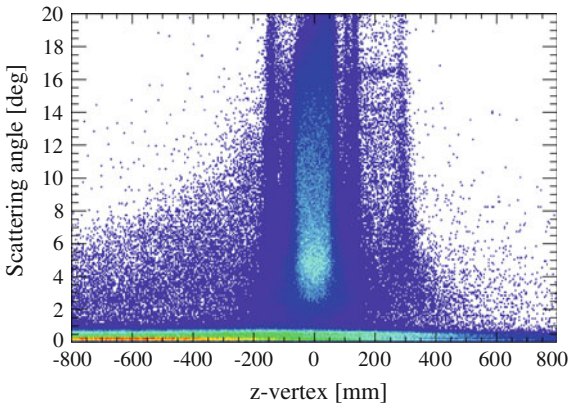

Fig. 3.13 Two-dimensional plot of the z-vertex versus the scattering angle in the Θ^+ search data. The large contribution of muons which originated from beam pion decay was observed in the small scattering angle region

- The z-vertex resolution rapidly deteriorates with decrease of the scattering angles. The target image could not recognize in events with the scattering angle less than 2°; see Appendix B.1 in detail.
- Large contribution of muons which originated from beam pion decay around the target region was observed in the forward scattering angle region as shown in Fig. 3.13. These muons which passed through the AC veto contaminated the (π, K) trigger data.

Figure 3.14 shows the vertex distributions along the z-axis (beam direction) and the r-axis (radial direction). The histograms of LH_2 target data are overlaid with those of the empty target data normalized by the beam flux. In order to accumulate a large number of events, (π^-, π^-) scattering events were used instead of (π^-, K^-) reaction events in the both histograms. In the z-vertex distribution, contributions from the mylar windows of the target vessel ($z = \pm 60$ mm) and the vacuum chamber ($z = \pm 135$ mm) are clearly seen in the empty target data. The bump around 280 mm is due to SDC1. In the r-vertex distribution, contribution from the side surface of the target vessel ($r = 33.9$ mm) are seen. The vertex cuts of $-60 < z < 60$ mm and $r < 30$ mm were applied in order to exclude the contamination from the surrounding materials without decreasing reaction events at the LH_2.

3.4.1 Vertex Cut Efficiency and Contamination Fraction

Figure 3.15 shows the vertex cut efficiency and the contamination fraction, which strongly depend on the scattering angle because the z-vertex resolution deteriorates with decrease of the scattering angles; therefore, they were calculated angle by angle. A net contribution from the LH_2 was obtained by subtracting the empty target data from the LH_2 target data as shown in Fig. 3.14. The vertex cut efficiency averaged over 2–15° was 84.8 % with a typical statistical uncertainty of 1.0 % in each angle. The contamination from the surrounding materials was obtained from the remaining

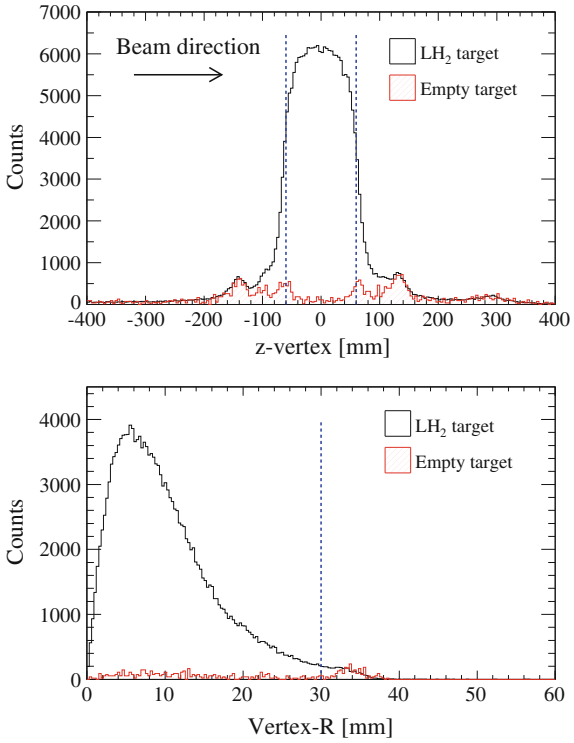

Fig. 3.14 Vertex distribution along (*top*) the z-axis, beam direction, and (*bottom*) the r-axis, radial direction. The open histograms show the LH_2 target data. The *red hatched histograms* show the empty target data normalized by the beam flux. The subtraction of these histograms represents a net contribution from LH_2. (π^-, π^-) events of scattering angles from 2° to 15° are selected in the both histograms. In the *top figure*, events with $r < 30$ mm are plotted, while, in the *bottom figure*, events with $-60 < z < 60$ mm are plotted. The *blue dashed lines* indicate the vertex cut positions

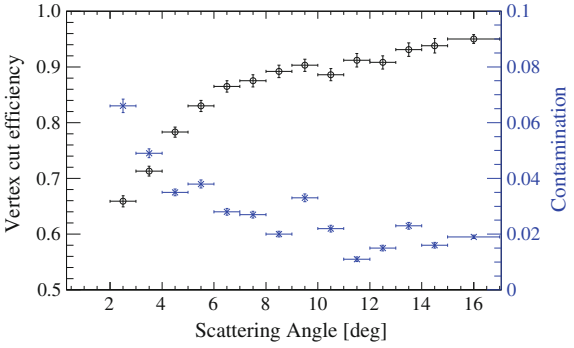

Fig. 3.15 Vertex cut efficiency and contamination fraction for each scattering angle. The *black circles* denote the vertex cut efficiency (left axis), while the *blue crosses* denote the contamination fraction (right axis). The vertical error bars denote the statistical uncertainty. The values at 16° stand for the values for scattering angles beyond 15°

events in the empty target data after applying the vertex cut. The contamination fraction averaged over 2–15° was found to be 3 %. It should be reminded that the present value was estimated by using the (π^-, π^-) events. The contamination fraction for the (π^-, K^-) events may be slightly smaller than that of the (π^-, π^-) events, because of a difference of these two reactions between a proton and nucleus target (see Appendix B.3). Hence, the contamination fraction for the (π^-, K^-) events was found to be less than 3 %.

3.5 Calibration Data

As described in Sect. 2.8, several calibration data were taken in addition to the Θ^+ search data. The validity of the missing-mass reconstruction was examined by using the $\pi^\pm p \to K^+ \Sigma^\pm$ reactions. Figure 3.16 shows the missing mass spectra obtained

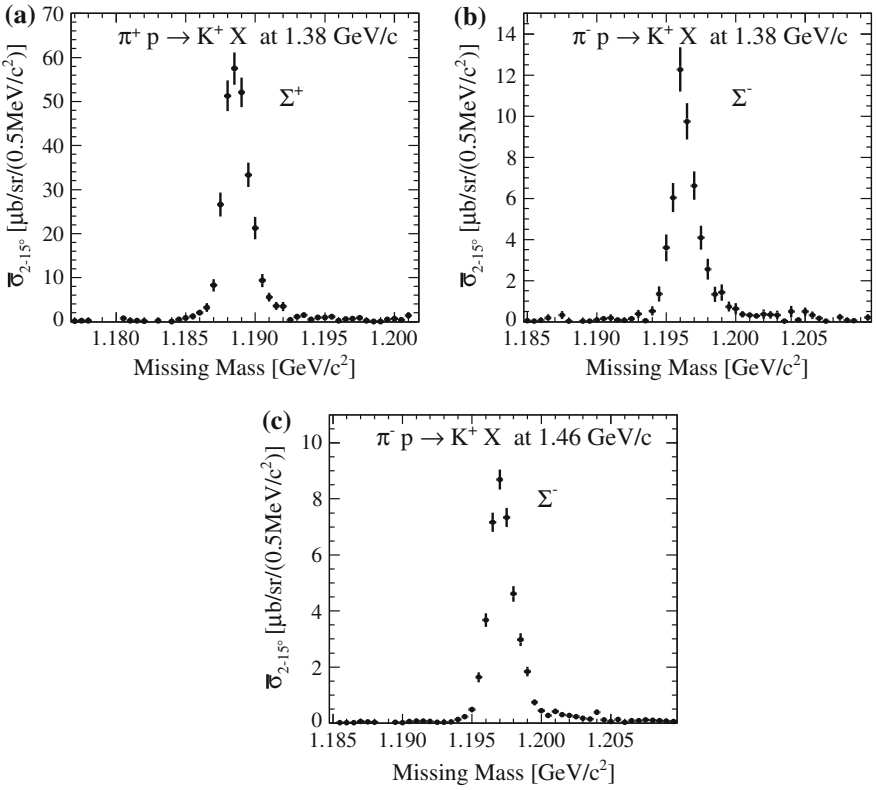

Fig. 3.16 Missing mass spectra of the $\pi^\pm p \to K^+ X$ reactions for the $\Sigma^\pm$ production. The ordinates represent the differential cross section averaged over the scattering angles of 2–15° in the laboratory frame. The quoted errors are statistical (These plots were made after applying the momentum calibration described in Sect. 3.6)

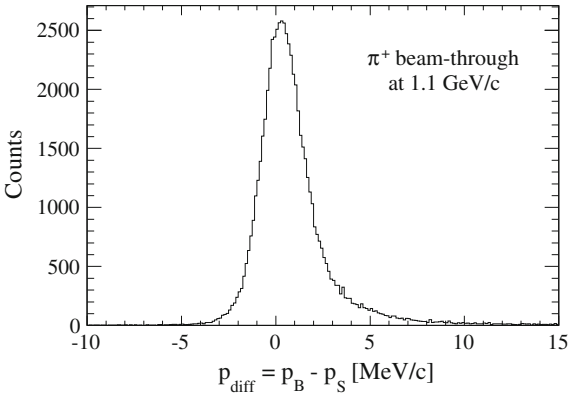

Fig. 3.17 Distribution of the momentum difference between the beam and SKS spectrometers, defined as $p_{\mathrm{diff}} \equiv p_{\mathrm{B}} - p_{\mathrm{S}}$ (see text), in the π^+ beam-through data at 1.1 GeV/c before the momentum calibration. The energy loss in the BH2 counter was subtracted from p_{B}

in three data sets of the Σ production reactions: (a) $\pi^+ p \to K^+ \Sigma^+$ at 1.38 GeV/c, (b) $\pi^- p \to K^+ \Sigma^-$ at 1.38 GeV/c, and (c) $\pi^- p \to K^+ \Sigma^-$ at 1.46 GeV/c. The $\Sigma^{\pm}$ peaks were correctly reconstructed with low background. The peak positions are used for the momentum calibration described in Sect. 3.6. The peak widths, which represent the missing-mass resolution for the Σ hyperons, are used for the estimation of the missing-mass resolution for the Θ^+, described in Sect. 3.7.

In the present experiment, the beam-through data were taken with three momentum settings, i.e., 0.9, 1.1, and 1.38 GeV/c, with both positively and negatively charged beams and with the empty target. In the beam-through data, the momentum difference, p_{diff}, was defined as

$$p_{\mathrm{diff}} \equiv p_{\mathrm{B}} - p_{\mathrm{S}}, \tag{3.8}$$

where p_{B} and p_{S} denote the momenta obtained by the beam and SKS spectrometer, respectively. Figure 3.17 shows a distribution of the momentum difference in the π^+ beam-through data at 1.1 GeV/c. The tail of the distribution is ascribed to the energy-loss straggling in the BH2 counter. In the same manner as the above Σ data, the peak positions are used for the momentum calibration, while the peak widths are used for the estimation of the missing-mass resolution for the Θ^+.

3.6 Momentum Calibration and Missing Mass Scale Uncertainty

The absolute scales of the momenta and missing mass are discussed in this section. There is no calibration peak in the Θ^+ search data, because the $\pi^- p \to K^- X$ reaction is an exotic production channel. Therefore, the absolute scale of the momenta were calibrated by using the $\Sigma^{\pm}$ production data and the $\pi^{\pm}$ beam-through data. In this experiment, it is important to determine the mass of Θ^+ correctly, if the peak is observed. The uncertainty of the missing mass scale for the $\pi^- p \to K^- \Theta^+$ reaction was finally estimated with the momentum scale uncertainty.

3.6.1 Energy Loss Correction

The energy loss in the LH_2 target and the BH2 counter was evaluated according to the Bethe–Bloch formula. The liquid hydrogen of a 12-cm length and the plastic scintillator of a 0.5-cm length were taken into account. The correction was applied to the beam-pion and scattered-kaon momenta event by event considering the reaction vertex point.

3.6.2 Momentum Correction in SKS

Figure 3.18a, b show correlation plots between an accuracy of the momentum versus the incident angle to SKS in the $\pi^- p \to K^+ \Sigma^-$ reaction. The accuracy of the momentum was defined by $p_{\mathrm{SKS}} - p_{\mathrm{kine}}$, where p_{SKS} is the kaon momentum measured with SKS, and p_{kine} is the kaon momentum calculated from the incident pion momentum and the scattering angle according to the kinematics of the $\pi^- p \to K^+ \Sigma^-$ reaction. The abscissas are (a) the horizontal angle dx/dz or (b) the vertical angle dy/dz. A correlation was observed especially in the region of $dx/dz > 0.1$, which corresponds to the inner tracks in SKS. The correlation seems to be attributed to the inaccuracy of the calculated magnetic field of SKS.

The correlation was corrected by using a forth-order polynomial function. The correction was applied to both dx/dz and dy/dz. Figure 3.18c, d show the correlation plots after applying the correction.[2] By this correction, the missing mass resolution for Σ^- was improved by 10 %. The correlation scheme was examined in three kinds of the Σ production data. The correlation curve of the Σ^+ data at 1.38 GeV/c was similar to that of the Σ^- data at 1.38 GeV/c due to the same reaction kinematics. Since the kaon momentum region for the $\Theta^+(1530)$ production at 2.01 GeV/c is almost the same as that for the Σ^- production at 1.46 GeV/c as shown in Fig. 3.25, the same correction function determined by the Σ^- at 1.46 GeV/c was applied to the Θ^+ search data.

3.6.3 Momentum Calibration

The initial scales of the momenta were reconstructed by the beam and SKS spectrometers based on the magnetic-field values monitored by the Hall probe and the NMR probe, respectively. Then, the energy loss correction in the LH_2 target and the BH2 counter was applied as described in Sect. 3.6.1. The Σ production data provided information on a mass difference, M_{diff}, between the reconstructed mass and the known Σ mass, i.e., $1189.37 \pm 0.07\,\mathrm{MeV}/c^2$ for Σ^+ and $1197.449 \pm 0.030\,\mathrm{MeV}/c^2$ for Σ^- [5]. On the other hand, the momentum difference, p_{diff}, defined in Eq. (3.8) was obtained from each beam-through event.

[2] The zeroth order coefficient of the function was not used for the correction because it corresponds to the absolute momentum scale which should be calibrated later in Sect. 3.6.3.

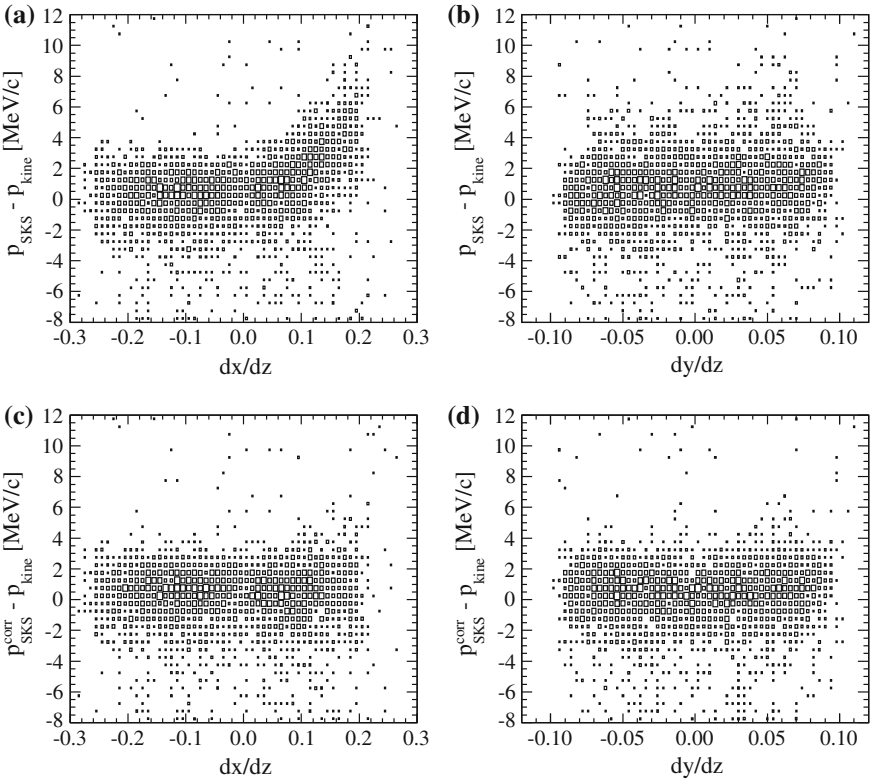

Fig. 3.18 Correlation between the accuracy of the momentum versus the incident angle to SKS in the $\pi^- p \to K^+ \Sigma^-$ reaction. The *left panels* **a**, **c** show the correlation to the horizontal angle dx/dz before (**a**) and after (**c**) the correction, while the *right panels* **b**, **d** show the correlation to the vertical angle dy/dz before (**b**) and after (**d**) the correction. The ordinates are $p_{\mathrm{SKS}} - p_{\mathrm{kine}}$, where p_{SKS} is the kaon momentum measured with SKS, and p_{kine} is the kaon momentum calculated from the incident pion momentum and the scattering angle according to the kinematics of the $\pi^- p \to K^+ \Sigma^-$ reaction

Table 3.1 shows the mass/momentum difference in each calibration data. M_{diff} and p_{diff} represent the peak value in the distribution. The error of M_{diff} was derived from the quadratic sum of the known Σ mass uncertainty [5] and the uncertainty of a peak fitting in the missing mass spectra, while the error of p_{diff} was from the uncertainty of a peak fitting in the p_{diff} distributions. These mass and momentum differences must be zero, if the absolute scales of both the beam and scattered-particle momenta are correct. Thus, the momentum scale calibration was done so as to reduce the mass and momentum differences simultaneously.

To compare M_{diff} equivalently with p_{diff}, M_{diff} was divided by the kinematical factor, $\frac{\partial M}{\partial p_{\mathrm{B}}}$ or $\frac{\partial M}{\partial p_{\mathrm{S}}}$:

$$\frac{\partial M}{\partial p_{\mathrm{B}}} = \frac{1}{M}\left[\beta_{\mathrm{B}}(m_p - E_{\mathrm{S}}) + p_{\mathrm{S}}\cos\theta\right], \tag{3.9}$$

Table 3.1 Mass/Momentum difference in each calibration data

Data	p_{B} (GeV/c)	p_{S} (GeV/c)	M_{diff} (MeV/c^2)	$M_{\mathrm{diff}}^{\mathrm{corr}}$ (MeV/c^2)
$\pi^+ p \to K^+ \Sigma^+$	1.38	0.92	-3.20 ± 0.07	-0.75
$\pi^- p \to K^+ \Sigma^-$	1.38	0.90	-1.63 ± 0.05	-1.07
$\pi^- p \to K^+ \Sigma^-$	1.46	0.99	-1.32 ± 0.04	-0.20
Data	p_{B} (GeV/c)	p_{S} (GeV/c)	p_{diff} (MeV/c)	$p_{\mathrm{diff}}^{\mathrm{corr}}$ (MeV/c)
π^+ B.T.	0.90	0.90	0.91 ± 0.06	-0.20
π^- B.T.	0.90	0.90	3.04 ± 0.06	-0.85
π^+ B.T.	1.10	1.10	0.39 ± 0.10	1.21
π^- B.T.	1.10	1.10	3.74 ± 0.07	1.79
π^+ B.T.	1.38	1.38	-3.17 ± 0.06	0.48
π^- B.T.	1.38	1.38	0.40 ± 0.08	1.28

p_{B} and p_{S} are the momenta obtained by the beam and SKS spectrometer, respectively. M_{diff} (p_{diff}) and $M_{\mathrm{diff}}^{\mathrm{corr}}$ ($p_{\mathrm{diff}}^{\mathrm{corr}}$) are the mass (momentum) differences before and after the calibration, respectively

$$\frac{\partial M}{\partial p_{\mathrm{S}}} = -\frac{1}{M}\left[\beta_{\mathrm{S}}(m_p + E_{\mathrm{B}}) - p_{\mathrm{B}}\cos\theta\right]. \tag{3.10}$$

These are derived from Eq. (3.1) where the subscripts π and K should be replaced by B and S which represent the beam and scattered particle, respectively; and β is the velocity of each particle. In the present Σ production reactions, $\frac{\partial M}{\partial p_{\mathrm{B}}}$ and $\frac{\partial M}{\partial p_{\mathrm{S}}}$ are 0.68 and -0.57, respectively, in the forward angle. M_{diff} divided by the kinematical factor is compatible with p_{diff}.

p_{diff} and $M_{\mathrm{diff}}/(\frac{\partial M}{\partial p_{\mathrm{B}}})$ are plotted in Fig. 3.19a as a function of the beam momentum p_{B}, while $-p_{\mathrm{diff}}$ and $M_{\mathrm{diff}}/(\frac{\partial M}{\partial p_{\mathrm{S}}})$ are plotted in Fig. 3.19b as a function of the scattered-particle momentum p_{S}. In Fig. 3.19a, b, one can see a common shift of 2–3 MeV/c between the opposite-charge with the same momentum, namely, three pairs of the $\pi^{\pm}$ beam-through data (blue open or green solid triangles) and a pair of the $\pi^{\pm} p \to K^+ \Sigma^{\pm}$ data at 1.38 GeV/c (red open or magenta solid circles). The shift is due to the opposite polarity setting of the beam spectrometer, because the shift was observed even in M_{diff}s of the $\pi^{\pm} p \to K^+ \Sigma^{\pm}$ data at 1.38 GeV/c where only the charge of the beam was different. In order to minimize the shifts observed in four pairs of the data with the opposite beam charge, a polarity offset parameter, z, was introduced as

$$p_{\mathrm{B}} \to p'_{\mathrm{B}} \equiv p_{\mathrm{B}} \pm z \text{ (double sign corresponds to the beam charge.)}, \tag{3.11}$$

$$z = 1.39 \pm 0.03 \text{ MeV}/c. \tag{3.12}$$

Figure 3.19c, d show the mass/momentum differences after applying the polarity offset. The shifts were reduced within 0.9 MeV/c.

Figure 3.19c, d give a dependence of the mass/momentum difference on the beam momentum p_{B} and scattered-particle momentum p_{S}, respectively. A negative correlation in terms of p_{B} is seen in Fig. 3.19c, whereas no clear correlation in terms of p_{S} is seen in Fig. 3.19d. This negative correlation corresponds to a linearity of the reconstructed beam momentum. Since the Hall probe was set at 75-mm upside of

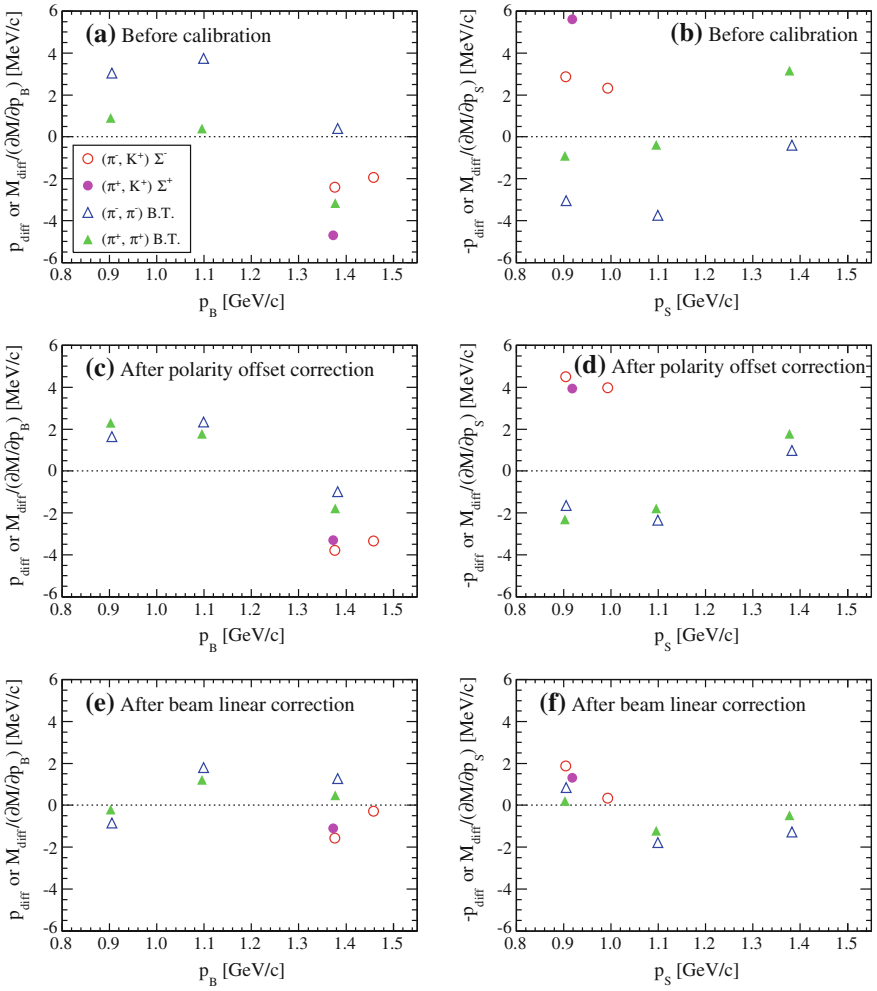

Fig. 3.19 Plots of the mass/momentum difference through the momentum calibration. The *left-side panels* **a**, **c**, **e** show p_{diff} or $M_{\mathrm{diff}}/(\frac{\partial M}{\partial p_{\mathrm{B}}})$ versus p_{B}, while the *right-side panels* **b**, **d**, **f** show $-p_{\mathrm{diff}}$ or $M_{\mathrm{diff}}/(\frac{\partial M}{\partial p_{\mathrm{S}}})$ versus p_{S}. The *top panels* **a**, **b** are the plots before the momentum calibration, the *middle panels* **c**, **d** are the plots after applying the polarity offset correction, and the *bottom panels* **e**, **f** are the plots after applying the beam linear correction. The *red open circles* are from the Σ^- data, the *magenta solid circle* is from the Σ^+ data, the *blue open triangles* are from the π^- beam-through data, and the *green solid triangles* are from the π^+ beam-through data

the central plane of the D4 magnet, the measured field value could deviate from the central field value which should be used in the transport calculation. This deviation could cause the linear correlation for p_{B}. Therefore, a linear correction for p'_B was introduced as

$$p'_{\mathrm{B}} \rightarrow p''_{\mathrm{B}} \equiv a p'_{\mathrm{B}} + b, \tag{3.13}$$

$$a = 1.0100 \pm 0.0001, \tag{3.14}$$

$$b = -11.56 \pm 0.13\ \mathrm{MeV}/c, \tag{3.15}$$

where a and b are the correction parameters determined by minimizing the mass and momentum differences. Figure 3.19e, f show the mass/momentum difference after applying the beam linear correction, which is also tabulated in the last column of Table 3.1. The differences were reduced between -2 and $2\,\mathrm{MeV}/c$.

We regarded the remaining differences as a systematic uncertainty of the momentum scale. In the momentum calibration above, no correction was applied for p_{S}; in other words, we regarded the momentum reconstructed by the SKS as the reference of the momentum scale. Therefore, the beam spectrometer was calibrated with SKS. The absolute scale uncertainty of the beam momentum is expected to be the same as that of the scattered-particle momentum. Assuming that the uncertainty is simply proportional to the momentum,

$$\frac{\delta p_{\mathrm{B}}}{p_{\mathrm{B}}} = \frac{\delta p_{\mathrm{S}}}{p_{\mathrm{S}}} \equiv \varepsilon. \tag{3.16}$$

ε was estimated to be 0.12 % from the maximum remaining difference obtained in the 1.1-GeV/c π^- beam-through data.

3.6.4 Missing Mass Scale Uncertainty

In the momentum calibration, we applied the polarity-offset and linear correction for the beam momentum, i.e.,

$$p_{\mathrm{B}} \rightarrow p''_{\mathrm{B}} \equiv a(p_{\mathrm{B}} \pm z) + b, \tag{3.17}$$

where the double sign corresponds to the beam charge. The π^- beam momentum of $2.01\,\mathrm{GeV}/c$ was corrected by $+7.1 \pm 0.1\,\mathrm{MeV}/c$ according to Eq. (3.17). The uncertainty of $0.1\,\mathrm{MeV}/c$ was propagated from the errors of a, b, and z,[3] which correspond to the uncertainties of the correction itself. Considering the kinematics of the $\pi^- p \rightarrow K^- \Theta^+$ reaction at $2.01\,\mathrm{GeV}/c$, the absolute scale of the missing mass was corrected by $+3.8 \pm 0.1\,\mathrm{MeV}/c^2$ for the $\Theta^+(1530)$ production. The uncertainty of $0.1\,\mathrm{MeV}/c^2$ was propagated from the above uncertainty of $0.1\,\mathrm{MeV}/c$.

In addition to the uncertainty of the correction itself ($0.1\,\mathrm{MeV}/c^2$), the systematic uncertainty of the momentum scale ($\varepsilon = 0.12\,\%$) discussed above, should be taken into account. Considering the kinematics of the $\pi^- p \rightarrow K^- \Theta^+$ reaction at $2.01\,\mathrm{GeV}/c$, the systematic uncertainty of the missing mass scale was estimated to be $1.3\,\mathrm{MeV}/c^2$, propagating from the momentum scale uncertainty of 0.12 %.

[3] The covariance between a and b (-1.39×10^{-5}) was also taken into account.

Hence, summing up 0.1 and 1.3 MeV/c^2, overall uncertainty of the missing mass scale for Θ^+ was found to be 1.4 MeV/c^2.

3.7 Momentum and Missing Mass Resolution

The resolutions of the momenta and missing mass are discussed in this section. As described in the previous section, there is no calibration peak in the Θ^+ search data, because the $\pi^- p \to K^- X$ reaction is an exotic production channel. Therefore, the resolution of the momenta was evaluated by using the $\Sigma^\pm$ production data and the $\pi^\pm$ beam-through data. In this experiment, it is important to estimate the missing mass resolution for the $\pi^- p \to K^- \Theta^+$ reaction.

In a reaction $B + p \to S + X$, where B and S denote a beam and scattered particles, respectively, the missing mass of X is calculated in the laboratory frame as follows:

$$M = \sqrt{(E_\mathrm{B} + m_p - E_\mathrm{S})^2 - \left(p_\mathrm{B}^2 + p_\mathrm{S}^2 - 2 p_\mathrm{B} p_\mathrm{S} \cos\theta\right)}, \tag{3.18}$$

where E_B and p_B are the energy and momentum of a beam particle, respectively; E_S and p_S are those of a scattered particle; m_p is the mass of a target proton; and θ is the scattering angle. The mass resolution ΔM is derived from the momentum resolution of the beam and scattered particles, Δp_B and Δp_S, the scattering angle resolution $\Delta\theta$, and ΔE_strag which stands for a contribution from the energy-loss straggling to the missing mass resolution. It can be expressed in the following equations[4]:

$$\Delta M^2 = \left(\frac{\partial M}{\partial p_\mathrm{B}}\right)^2 \Delta p_\mathrm{B}^2 + \left(\frac{\partial M}{\partial p_\mathrm{S}}\right)^2 \Delta p_\mathrm{S}^2 + \left(\frac{\partial M}{\partial \theta}\right)^2 \Delta\theta^2 + \Delta E_\mathrm{strag}^2, \tag{3.19}$$

$$\frac{\partial M}{\partial p_\mathrm{B}} = \frac{1}{M}\left[\beta_\mathrm{B}(m_p - E_\mathrm{S}) + p_\mathrm{S}\cos\theta\right], \tag{3.20}$$

$$\frac{\partial M}{\partial p_\mathrm{S}} = -\frac{1}{M}\left[\beta_\mathrm{S}(m_p + E_\mathrm{B}) - p_\mathrm{B}\cos\theta\right], \tag{3.21}$$

$$\frac{\partial M}{\partial \theta} = -\frac{1}{M} p_\mathrm{B} p_\mathrm{S} \sin\theta, \tag{3.22}$$

where β represents the velocity of each particle. The covariance terms in Eq. (3.19) were ignored in this analysis. Since p_B and p_S were obtained by independent spectrometers, they are not correlated. The correlation between the scattering angle θ and each momentum was neglected assuming that their contribution to the overall resolution is limited.

[4]The scattering angle term was negligibly small in previous hypernuclear experiments using SKS because of the large target mass M; however, the term is not negligible in hadron production reactions.

In the following subsections, the contributions of Δp_{B}, Δp_{S}, $\Delta\theta$, and $\Delta E_{\mathrm{strag}}$ are estimated step by step, and then, the missing mass resolution for the $\pi^- p \to K^- \Theta^+$ reaction is finally estimated.

3.7.1 Energy Loss Straggling

The energy loss distribution in materials of moderate thickness is expressed by the Landau–Vavilov distribution. The FWHM of the distribution is approximately expressed as [5]

$$\mathrm{FWHM} \simeq 4\xi, \tag{3.23}$$

$$\xi \equiv 2\pi N_{\mathrm{A}} r_e^2 m_e \frac{Z}{A}\frac{\rho x}{\beta^2}, \tag{3.24}$$

where N_{A} is the Avogadro's number, r_e the classical electron radius, m_e the electron mass, Z and A the atomic number and atomic mass of the material, β the particle velocity, and ρx the mass thickness. $\Delta E_{\mathrm{strag}}$ denotes the contribution from the energy-loss straggling in the LH_2 target and the BH2 counter to the missing mass resolution. The liquid hydrogen of a 12-cm length and the plastic scintillator of a 0.5-cm length were considered. $\Delta E_{\mathrm{strag}}$ was calculated to be 0.39 MeV (FWHM) for the Θ^+ production reaction at 2 GeV/c. The dependence on the reaction vertex point in the target was less than 0.01 MeV.

3.7.2 Scattering Angle Resolution

The missing mass resolution for Σ at the scattering angles of 2–15° was obtained by fitting the peaks of the Σ hyperons shown in Fig. 3.16. The missing mass peaks tend to have the Landau tail in the high-mass side due to the energy-loss straggling. Since the tails are not so significant as shown in Fig. 3.16, the Gaussian distribution was used in the fitting. Table 3.2 shows the obtained missing mass resolution. The systematic uncertainty of ±0.1 MeV was estimated from the fitting range dependence.

As can be seen in Eqs. (3.19)–(3.22), the missing mass resolution depends on the scattering angle θ. At the forward angles of 2–15°, the θ-dependence predominantly comes from the $\sin\theta$ term in Eq. (3.22). Therefore, ΔM can be expressed as a function of θ:

$$\Delta M(\theta) = \sqrt{a_0 + a_1 \sin^2\theta}, \tag{3.25}$$

$$a_0 \equiv \left(\frac{\partial M}{\partial p_{\mathrm{B}}}\right)^2 \Delta p_{\mathrm{B}}^2 + \left(\frac{\partial M}{\partial p_{\mathrm{S}}}\right)^2 \Delta p_{\mathrm{S}}^2 + \Delta E_{\mathrm{strag}}^2, \tag{3.26}$$

Table 3.2 Missing mass resolution for Σ, ΔM_{2-15°, at scattering angles of 2–15° (upper table) and the resolution for the momentum difference, $\Delta p_{\rm diff}$, in the beam-through data (lower table)

Data	$p_{\rm B}$ (GeV/c)	ΔM_{2-15° (MeV)
$\pi^+ p \to K^+ \Sigma^+$	1.38	$2.12 \pm 0.06 \pm 0.1$
$\pi^- p \to K^+ \Sigma^-$	1.38	$2.24 \pm 0.10 \pm 0.1$
$\pi^- p \to K^+ \Sigma^-$	1.46	$2.21 \pm 0.05 \pm 0.1$
Data	$p_{\rm B}$ (GeV/c)	$\Delta p_{\rm diff}$ (MeV/c)
π^+ B.T.	0.90	2.22 ± 0.12
π^- B.T.	0.90	2.18 ± 0.12
π^+ B.T.	1.10	2.69 ± 0.12
π^- B.T.	1.10	2.65 ± 0.12
π^+ B.T.	1.38	4.11 ± 0.12
π^- B.T.	1.38	4.00 ± 0.12

ΔM_{2-15° and $\Delta p_{\rm diff}$ are shown in FWHM. For the errors of ΔM_{2-15°, the first one is statistical and the second one is systematic uncertainty estimated from the fitting range dependence. For the errors of $\Delta p_{\rm diff}$, the statistical error is negligibly small and the quoted error is estimated from the fitting range dependence

$$a_1 \equiv \left(\frac{p_{\rm B} p_{\rm S}}{M} \Delta\theta\right)^2 . \tag{3.27}$$

Figure 3.20 shows the scattering angle dependence of the missing mass resolution in the Σ^- production data at 1.46 GeV/c. The data were well fitted by Eq. (3.25) with the θ-independent parameters a_0 and a_1; here, we neglected a slight θ-dependence of $p_{\rm S}$, and assumed that $\Delta p_{\rm S}$ and $\Delta\theta$ are independent of θ. The scattering angle resolution $\Delta\theta$ was found from a_1 to be 5.7 ± 0.8 mrad (FWHM). The value was consistent with the other two set of the Σ data. In addition, since a_0 is equivalent to $\Delta M^2(0^\circ)$, the missing mass resolution at 0°, $\Delta M(0^\circ)$, was found to be 1.89 ± 0.07 MeV (FWHM).

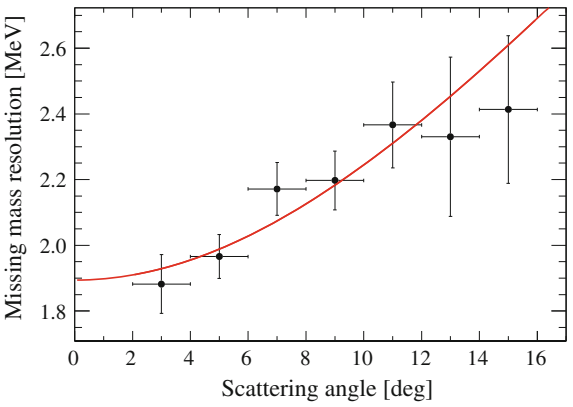

Fig. 3.20 Scattering angle dependence of the missing mass resolution in the Σ^- production data at 1.46 GeV/c. The data were fitted by Eq. (3.25) with the θ-independent parameters a_0 and a_1

3.7.3 Momentum Resolution

The stability of the magnetic field of both spectrometers was monitored during the experiment (see Appendix C). The long-term fluctuation of the beam and SKS spectrometer field was less than 2.4×10^{-4} and 9.6×10^{-5}, respectively, which were neglected in the momentum resolution estimation.

In order to obtain Δp_{B} and Δp_{S}, Eq. (3.19) in the Σ production data is used. In addition, from the p_{diff} ($=p_{\mathrm{B}} - p_{\mathrm{S}}$) distribution obtained from the beam-through data as shown in Fig. 3.17, the width of the distribution Δp_{diff} is also used. Δp_{diff} is composed of the momentum resolutions of the beam and SKS spectrometers and the energy-loss straggling effect in BH2 ($\Delta p_{\mathrm{strag}}$). It is written as

$$\Delta p_{\mathrm{diff}}^2 = \Delta p_{\mathrm{B}}^2 + \Delta p_{\mathrm{S}}^2 + \Delta p_{\mathrm{strag}}^2, \tag{3.28}$$

where $\Delta p_{\mathrm{strag}}$ was calculated in the same way as for $\Delta E_{\mathrm{strag}}$. Table 3.2 shows Δp_{diff} obtained from each beam-through data. Since Δp_{diff}s in three pairs of the beam-through data with the same momentum but with the opposite charge were consistent within the errors, it was found that the momentum resolution does not depend on the magnet polarity.

Assuming that the momentum resolution is simply proportional to the momentum, $\Delta p_{\mathrm{B}}/p_{\mathrm{B}}$ and $\Delta p_{\mathrm{S}}/p_{\mathrm{S}}$ were derived by solving the quadratic equations (3.19) and (3.28). Considering the consistency of p_{S} with the Θ^+ production reaction, the Σ^- data at 1.46 GeV/c were used for Eq. (3.19) and the beam-through data at 1.1 GeV/c were used for Eq. (3.28). The resolution of the beam spectrometer was calculated to be $\Delta p_{\mathrm{B}}/p_{\mathrm{B}} = (1.4 \pm 0.2) \times 10^{-3}$ and that of the SKS spectrometer was $\Delta p_{\mathrm{S}}/p_{\mathrm{S}} = (2.0 \pm 0.2) \times 10^{-3}$ in FWHM.

3.7.4 Missing Mass Resolution

Using Δp_{B}, Δp_{S}, $\Delta\theta$ and $\Delta E_{\mathrm{strag}}$ obtained above and considering the kinematics for the Θ^+ production, the missing mass resolution expected for the Θ^+ was derived as a function of the scattering angle, $\Delta M_{\Theta}(\theta)$, which is shown in Fig. 3.21 with a black solid line with an yellow 1σ error band. The contributions from each component are also shown in the figure. As for the Θ^+ missing mass resolution, the beam momentum resolution was dominant in the small angle region because of the high beam momentum of 2 GeV/c, whereas the scattering angle resolution was dominant in the large angle region.

In order to utilize in the following analysis, we needed the mass resolution averaged over 2–15°, which was evaluated to be 2.13 ± 0.15 MeV (FWHM) with a simulation assuming the isotropic angular distribution for the $\Theta^+(1530)$ production. The uncertainty was estimated from the upper and lower error bands of $\Delta M_{\Theta}(\theta)$. The dependence on different angular distributions, e.g., forward or backward peaked

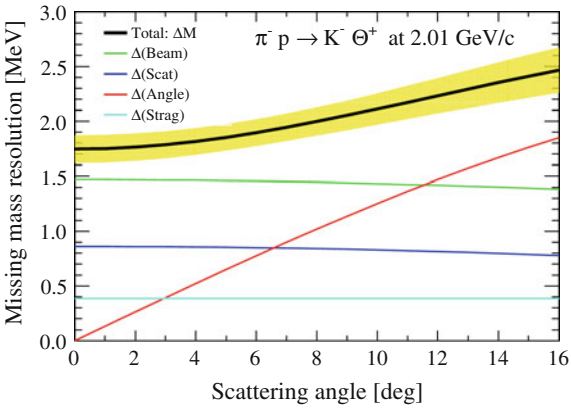

Fig. 3.21 Scattering angle dependence of the missing mass resolution for the Θ^+ production at 2.01 GeV/c. The *black solid line* indicates $\Delta M_\Theta(\theta)$ and the *yellow area* represents the 1σ error band. The four contributions in Eq. (3.19) are also shown: $\Delta(\text{Beam}) \equiv \frac{\partial M}{\partial p_\text{B}} \Delta p_\text{B}$ (*green*), $\Delta(\text{Scat}) \equiv \frac{\partial M}{\partial p_\text{S}} \Delta p_\text{S}$ (*blue*), $\Delta(\text{Angle}) \equiv \frac{\partial M}{\partial \theta} \Delta\theta$ (*red*) and $\Delta(\text{Strag}) \equiv \Delta E_\text{strag}$ (*cyan*)

distributions such as $\frac{1\pm\cos\theta}{2}$, was examined and found to be less than 0.1 MeV, because the present experimental acceptance was limited to the forward angles of 2–15°. The Θ^+ mass dependence was also examined between 1500 and 1550 MeV/c^2, and found to be negligible (<0.002 MeV).

3.8 Cross Section

The cross section of the $\pi p \to KX$ reaction was calculated from the experimental yields as

$$\frac{d\sigma}{d\Omega} = \frac{A}{(\rho x)\, N_\text{A}} \cdot \frac{N_K}{N_\text{beam}} \cdot \frac{1}{\varepsilon_\text{exp}\, d\Omega}, \tag{3.29}$$

where A is the atomic mass of target Hydrogen, ρx the target mass thickness, N_A the Avogadro's number, N_beam the scaler counts of the beam trigger, N_K the number of (π, K) events, ε_exp the total experimental efficiency and $d\Omega$ the solid angle of SKS. Table 3.3 is a list of the experimental efficiency factors which consists of the beam normalization, detection efficiency, analysis efficiency and other factors. Some factors depend on various experimental conditions, e.g., beam intensity, scattering angle, and momentum, which are discussed in the next subsection. The acceptance of SKS estimated by a MC simulation is described in the following subsection.

3.8.1 Efficiency

The efficiency factors were evaluated for both the Θ^+ search data and the Σ production data. Hereinafter, representative values for the Θ^+ search data are mentioned and quoted errors are statistical one unless otherwise noted.

Table 3.3 List of the experimental efficiency factors

Efficiency	Typical value (%)
Beam normalization factor	90.2 ± 1.9
BC1,2 efficiency	85.0 ± 0.5
BC3,4 efficiency	99.1 ± 0.3
Beam spectrometer tracking efficiency	98.2 ± 0.3
Single track ratio	94.3 ± 0.3
SDC1,2 efficiency	97.4 ± 0.2
SDC3,4 efficiency	94.6 ± 1.1
SKS tracking efficiency	97.0 ± 0.8
TOF efficiency	99.6 ± 2.5
LC efficiency	97.5 ± 2.4
AC overkill factor	91.8 ± 2.1
PID efficiency for kaon	95.5 ± 2.0
Vertex cut efficiency	84.8 ± 1.0
Kaon decay factor	48.3 ± 0.4[a]
K^- absorption factor	91.1 ± 1.2
Data acquisition efficiency	76.9 ± 0.5
Matrix trigger efficiency	98.6 ± 1.4
Total efficiency	15.1 ± 0.9

Typical values in the Θ^+ search data are shown
[a] A representative value in case of a 1-GeV/c momentum and a 5-m path length

3.8.1.1 Beam Normalization Factor

The beam normalization factor represents a fraction of the effective pion number out of N_{beam}. It was estimated to be $90.2 \pm 1.9\,\%$, taking into account the following components:

Muon contamination Electrons (or positrons) in the beam were rejected by GC at trigger level. However muons, which are decay products of pions, can not be separated from pions. The muon contamination rate was estimated to be $3.0 \pm 2.0\,\%$ by a MC simulation using DECAY- TURTLE [6]. In the simulation, the properties of the magnets, slits and separators in the K1.8 beam line were taken into account. Note that most of muons which reached the experimental target were originated from the pion decay in the beam spectrometer magnets. The quoted error represents the systematic uncertainty in the simulation, which was estimated as follows; in previous experiments at KEK-PS [7, 8], the muon contamination rate was measured with a high-pressure Freon-gas Cherenkov counter and agreed with a DECAY- TURTLE simulation within 2 %.

Accidental coincidence The accidental coincidence rate between BH1 and BH2 was estimated to be 3.2 ± 0.3 % by using time-of-flight spectra in the beam trigger as described in Sect. 3.2.1.

Beam profile The beam tracks which did not pass through the target volume were excluded from the number of beams. A typical targeting efficiency was 96.1 ± 0.3 % as shown in Fig. 3.5.

3.8.1.2 BC1·2 and BC3·4 Tracking Efficiency

The efficiency of the beam local tracking was estimated using pion beam particles defined with BH1 and BH2 in the beam trigger data. The BC1·2 and BC3·4 tracking efficiencies are the total efficiency including the analysis efficiency to find a local straight-line track at the entrance and exit of the QQDQQ magnets, which were found to be typically 85.0 ± 0.5 and 99.1 ± 0.3 %, respectively. As was mentioned in Sect. 2.2, due to the beam ripples, the maximum instantaneous rate came up to 10–20 times as high as the mean rate. Since these high-multiplicity events consumed enormous processing time in the track finding, events including more than 10^5 track candidates were discarded in the present analysis. The BC1·2 tracking efficiency depended on the beam intensity and the number of active layers, and was evaluated run by run, whereas the BC3·4 tracking efficiency was stable within the error.

3.8.1.3 Beam Spectrometer Tracking Efficiency and Single Track Ratio

The beam spectrometer tracking efficiency is the analysis efficiency to reconstruct a particle trajectory in the beam spectrometer after determining the local straight-line tracks in both the BC1·2 and BC3·4 tracking. A typical efficiency was found to be 98.2 ± 0.3 %. In the present analysis, events including more than two beam tracks were discarded. A typical single track ratio was 94.3 ± 0.3 %.

3.8.1.4 SDC1·2 Tracking Efficiency

The SDC1·2 tracking efficiency is the total efficiency including the analysis efficiency to find a local straight-line track at the entrance of the SKS magnet. It was estimated by using the beam trigger data. Tracks which should pass through the effective area of SDC1 and SDC2 were defined by the beam track determined by BC3 and BC4. The beam absorption between BC4 and SDC1 was ignored. The efficiency was found to be 97.4 ± 0.2 %. In this procedure, the incident beam angles to SDC1 and SDC2 were almost less than 2°. We assumed that the efficiency was the same for large incident angles.

3.8.1.5 SDC3·4 Tracking Efficiency

The SDC3·4 tracking efficiency is the total efficiency including the analysis efficiency to find a local straight-line track at the exit of the SKS magnet. It was estimated by using scattered proton events in the data set of the $\pi^{\pm}p \rightarrow K^{+}\Sigma^{\pm}$ reactions, since protons are free from decay in fight. Figure 3.22 shows a scatter plot of the horizontal scattering angle determined by SDC1 and SDC2 versus the inverse time-of-flight between TOF and BH2 taken from the Σ^{-} production data. The scattered proton events were selected as shown in the figure. The efficiency estimated in the Σ^{-} production data was $98.2 \pm 0.2\,\%$. Figure 3.23 shows the SDC3·4 tracking efficiency as a function of the horizontal track positions at TOF. The position dependence was found to be within 0.5 %. As for the Σ^{+} production data, the chamber hit rate was higher than that of Σ^{-} data because of the decay product of the beam particle, and therefore the efficiency decreased by 2 %. Taking account of the rate dependence, the efficiency for the Θ^{+} search data was estimated to be $94.6 \pm 1.1\,\%$.

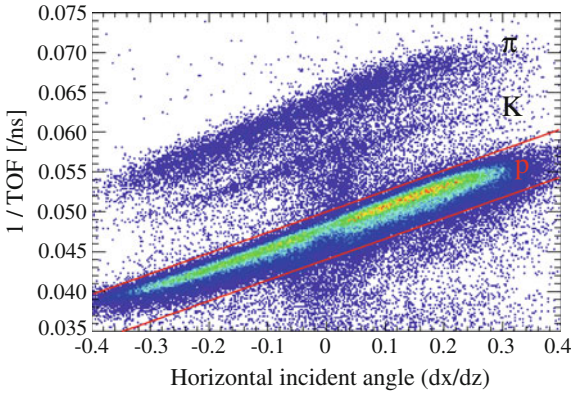

Fig. 3.22 Scatter plot of horizontal scattering angle versus inverse time-of-flight between TOF and BH2 in the Σ^{-} production data. The loci for pions, kaons and protons are seen. The red lines indicate the proton selection gate

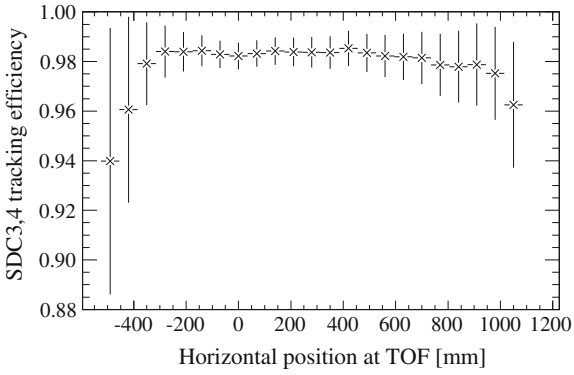

Fig. 3.23 SDC3·4 tracking efficiency for each horizontal track position at TOF in the Σ^{-} production data. Each point corresponds to a segment of TOF. The quoted errors are statistical

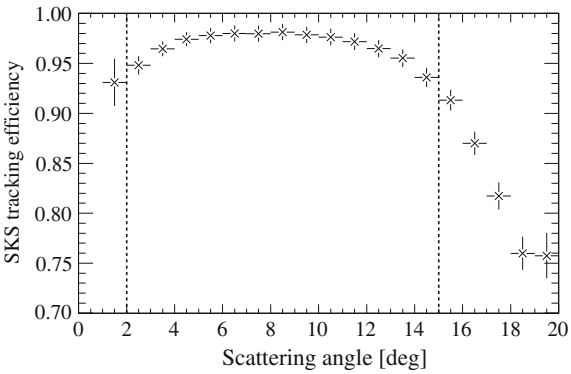

Fig. 3.24 SKS tracking efficiency for each scattering angle. The *dashed lines* indicate the angle region adopted in the present analysis. The quoted errors are statistical

3.8.1.6 SKS Tracking Efficiency

The SKS tracking efficiency is the analysis efficiency to reconstruct a particle trajectory in the SKS spectrometer after determining the local straight-line tracks in both the SDC1·2 and SDC3·4 tracking. It was estimated by using the scattered proton events in the data set of the $\pi^{\pm}p \rightarrow K^{+}\Sigma^{\pm}$ reactions, since protons are free from decay in fight. Since the efficiency depends on the incident angle to SKS, it was estimated angle by angle as shown in Fig. 3.24. For the forward angles of less than 2°, it was difficult to estimate the proper efficiency since beam-related products contaminated the scattered proton events. The efficiency decrease in the large angle region was due to an inaccuracy of the magnetic field calculation in the fringing regions.[5] Events with the scattering angles more than 15° were not used in the present analysis. A typical efficiency for 2–15° was $97.0 \pm 0.8\,\%$.

3.8.1.7 TOF and LC Efficiency

The detection efficiency of TOF was estimated by using controlled trigger data (BEAM × LC) where hits of the TOF counter were not required. Scattered pion events were selected by reconstructing a particle trajectory in SKS, because the number of kaon events was too small to use for this analysis. Events which should be detected in TOF were defined by the particle trajectory and the LC hit segment. The efficiency was found to be $99.6 \pm 2.5\,\%$. The dependence on the momentum and incident angle was within the error in the 0.8–1.2 GeV/c and 0–20° ranges, respectively. The result was assumed to be the same for kaons because of a small energy-loss difference between a pion and a kaon in a momentum range of 0.8–1.2 GeV/c.

The detection efficiency of LC was similarly estimated to be $97.5 \pm 2.4\,\%$ by using controlled trigger data (BEAM × TOF) where hits of the LC counter were

[5] In the region near the pole edge and the coil of the SKS magnet, the calculated field value deviated from the measured value in 10^{-2}, whereas the deviation was within 10^{-3} in the central region [9].

not required. Events which should be detected in LC were defined by the particle trajectory and the TOF hit segment. The pion absorption in AC (∼2 %) was ignored. The dependence on the momentum and the incident angle was within the error. The result was assumed to be the same for kaons, because the discriminator threshold of LC was set to be low enough.

3.8.1.8 AC Overkill Factor

The kaon overkill by AC occurred by the following reasons:

Accidental veto The accidental veto rate, $f_{\rm acc}$, was calculated as

$$f_{acc} = \frac{R_{\rm AC} \times W_{\rm coin}}{F_{\rm duty}}, \tag{3.30}$$

where $R_{\rm AC}$ is the single rate of AC, $W_{\rm coin} = 30 \pm 5$ ns is the coincidence width of AC in the (π, K) trigger, and $F_{\rm duty} = 0.18$ is the beam duty factor described in Sect. 2.2. In the Θ^+ search data, the single rate of AC was 200 kHz due to muons originated from the beam pion decay. Therefore, the accidental veto rate was calculated to be 3.3 ± 0.6 %.

δ-ray induced The overkill rate induced by the δ-ray was estimated by using controlled trigger data (BEAM × TOF × LC) mixed in the Σ^- production data, where the accidental veto rate was negligible (0.4 %) since the single rate of AC was 20 kHz. Scattered proton events which should not fire AC were used, because the number of kaon events was too small to use for this analysis. The tracks which should pass through the AC effective area were defined by the particle trajectory with the hits of TOF and LC. The overkill rate was found to be 4.9 ± 2.0 % in the momentum range of 0.8–1.1 GeV/c. The uncertainty was estimated from the momentum dependence. The result was assumed to be the same for kaons.

Consequently, summing up the above two factors, the kaon overkill rate by AC was estimated to be 8.2 ± 2.1 %.

3.8.1.9 Kaon Decay Factor

Since the $\beta\gamma c\tau$ of a 1-GeV/c kaon is 7.5 m, about a half of the kaons produced in the target decay before they reach the detectors. The kaon decay events before passing through SDC4 were rejected by the SKS track reconstruction process. The kaon survival rate to SDC4 ($\varepsilon_{\rm surv}$) was calculated event by event using the momentum (p) and the flight path length from the vertex point to SDC4 (L) as

$$\varepsilon_{\rm surv} = \exp\left(-\frac{Lm}{pc\tau}\right), \tag{3.31}$$

where m and τ denote the mass and the life time of the kaon, respectively. A representative value was $51.4 \pm 0.4\,\%$ in case of $p = 1\,\mathrm{GeV}/c$ and $L = 5\,\mathrm{m}$. The uncertainty was mainly ascribed to that of L which was estimated from the thickness of SDC4 of 6 cm.

Furthermore, a part of kaons which decayed after passing through SDC4 fired AC or escaped from the detector acceptance. The probability of these leakages from the (π, K) trigger was evaluated to be $6.1 \pm 0.4\,\%$ by a MC simulation. The uncertainty was estimated from the momentum dependence between 0.9 and 1.1 GeV/c.

Consequently, a typical kaon decay correction factor was $48.3 \pm 0.4\,\%$ in case of a 1-GeV/c momentum and a 5-m path length.

3.8.1.10 Kaon Absorption Factor

Some of the kaons produced in the target are absorbed by materials along the flight path in the spectrometer, which are listed in Table 3.4.

First, a simple calculation is given: the absorption rate f_{abs} was estimated as

$$f_{\mathrm{abs}} = \sum_i \sigma_{\mathrm{inel}}^{KA} \frac{N_{\mathrm{A}}\,(\rho x)_i}{A_i} \approx \sigma_{\mathrm{inel}}^{KN} N_{\mathrm{A}}\,(\rho x)\,, \tag{3.32}$$

where $\sigma_{\mathrm{inel}}^{KA}$ and $\sigma_{\mathrm{inel}}^{KN}$ denote the K-induced inelastic cross sections for a nucleus A and a nucleon N, respectively; N_{A} is the Avogadro's number, ρx the thickness of materials, A the atomic mass, and i represents an index of the materials; here, we assumed $\sigma_{\mathrm{inel}}^{KA} \approx A\ \sigma_{\mathrm{inel}}^{KN}$. The $K^- N$ and $K^+ N$ inelastic cross sections around 1 GeV/c are approximately 20 and 3 mb, respectively [5]. Therefore, the absorption rates for K^- and K^+ were found to be 10 and 1.5 %, respectively.

Next, the absorption rate was evaluated by using a MC simulation based on GEANT4 [10] including the realistic materials and hadronic reactions. The K^- absorption rate was found to be $8.9 \pm 1.2\,\%$. The uncertainty was estimated from the momentum dependence between 0.9 and 1.1 GeV/c. The K^+ absorption rate was found to be $2.7 \pm 0.7\,\%$. These values are in good agreement with those of the simple calculation. We adopted the simulated values as the absorption rates.

Table 3.4 Materials along the flight path in the SKS spectrometer

Material	Length (cm)	Density (g/cm^3)	Thickness (g/cm^2)
LH_2 target	12.0	0.0709	0.85
TOF	3.0	1.06	3.18
AC (aerogel)	11.3	0.20	2.26
AC (Al frame)	0.6	2.70	1.62
He	∼300	0.000179	0.05
Air	∼200	0.00129	0.26
Total			8.22

3.8.1.11 Data-Acquisition Efficiency

The data-acquisition efficiency, caused by the dead time of the data-acquisition system, was obtained as a ratio of the number of events accepted by the data-acquisition system to that of the triggered events. Since the efficiency depends on the trigger rate, it was estimated rate by rate. A typical efficiency was $76.9 \pm 0.5\,\%$ at a trigger rate of 600 per 2.2-s spill. The uncertainty was estimated from the time fluctuation.

3.8.1.12 Matrix Trigger Efficiency

In the Θ^+ search data, the prescaled (π, K) trigger data without the matrix coincidence trigger was also taken with the prescale factor of 10. The matrix trigger efficiency was defined as a ratio of the number of (π, K) events with the matrix trigger to that without the matrix trigger. It was estimated to be $98.6 \pm 1.4\,\%$. Since the dependence on the scattering angle and the scattered-particle momentum was within the error, the matrix trigger made no bias on the missing mass spectrum.

3.8.1.13 Summary of Efficiencies

Summarizing the efficiency factors described above with the PID efficiency for a kaon (Sect. 3.3.2) and the vertex cut efficiency (Sect. 3.4), the overall efficiency factor was calculated event by event. A typical efficiency was estimated to be $15.1\,\%$. A typical uncertainty of $0.9\,\%$ was obtained by summing up all the uncertainties in quadrature assuming no correlation among the efficiencies. Hence, the relative systematic uncertainty caused by the efficiency correction was estimated to be $0.9/15.1 = 6\,\%$ for the Θ^+ search data.

The relative systematic uncertainty for the $\Sigma^\pm$ production data was similarly estimated to be $5\,\%$. Since the kaon momentum in the Σ production reaction is within a narrow range around 0.9 or 1.0 GeV/c, the uncertainty due to the kaon momentum dependence was smaller than that of the Θ^+ search data.

3.8.2 Acceptance of SKS

The acceptance of SKS was estimated with a MC simulation as a function of the momentum p_{SKS} and the angle θ_{SKS} which was defined as the incident angle to SDC1.[6] In the simulation, realistic distributions of the beam profile and the reaction vertex point were taken into account, and the acceptance was averaged over the distribution. Note that the acceptance evaluated in this simulation is a geometrical

[6] θ_{SKS} is almost the same as the scattering angle and does not depend on the beam direction.

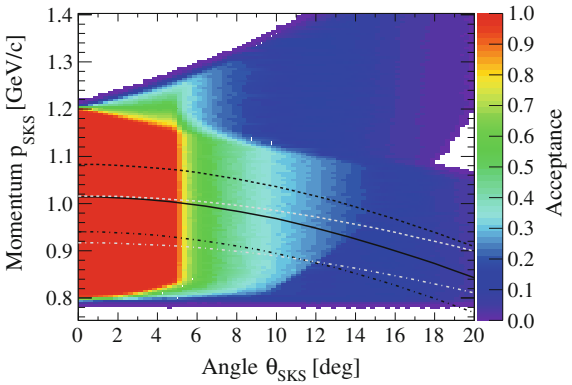

Fig. 3.25 Acceptance of SKS as a function of the momentum (p_{SKS}) and the incident angle (θ_{SKS}) in the Θ^+ search data. The magnetic field was set at 2.5 T. A part of the TOF (#1–10) and LC (#1–7) segments installed at the high-momentum side were not used in the present experiment. The *black solid*, *dashed*, and *dashed-dotted lines* indicate the kinematics of the $\pi^- p \to K^- \Theta^+$ reaction at 2.01 GeV/c assuming the Θ^+ masses of 1530, 1500, and 1560 MeV/c^2, respectively. The *gray dashed* and *dashed-dotted lines* indicate the kinematics of the $\pi^- p \to K^+ \Sigma^-$ reaction at 1.46 and 1.38 GeV/c, respectively

one; the effect of the detector efficiencies, particle decay and absorption are taken into account as the efficiency factor.

Particles were generated uniformly in a phase space defined by p_{SKS} and θ_{SKS}: from $(p_{\mathrm{SKS}} - \frac{1}{2}\Delta p)$ to $(p_{\mathrm{SKS}} + \frac{1}{2}\Delta p)$ and from $\cos(\theta_{\mathrm{SKS}} + \frac{1}{2}\Delta\theta)$ to $\cos(\theta_{\mathrm{SKS}} - \frac{1}{2}\Delta\theta)$, where the step sizes were defined as $\Delta p = 5$ MeV/c and $\Delta\theta = 0.25°$. The particle generation was uniform in azimuthal angle from 0 to 2π. The acceptance was calculated as a ratio of the number of the detected events (N_{det}) to that of the generated events (N_{gen}). Hence, the solid angle was calculated as

$$d\Omega(p_{\mathrm{SKS}}, \theta_{\mathrm{SKS}}) = 2\pi \int_{\theta - \frac{1}{2}\Delta\theta}^{\theta + \frac{1}{2}\Delta\theta} d\cos\theta \times \frac{N_{\mathrm{det}}(p_{\mathrm{SKS}}, \theta_{\mathrm{SKS}})}{N_{\mathrm{gen}}(p_{\mathrm{SKS}}, \theta_{\mathrm{SKS}})}. \tag{3.33}$$

This process was carried out step by step for p_{SKS} and θ_{SKS}.

Figure 3.25 shows the acceptance of SKS as a function of p_{SKS} and θ_{SKS}. The full acceptance was confirmed in the region of the momenta of 0.8–1.2 GeV/c and the angles less than 5°. The angular acceptance was limited by the vertical gap of the SKS magnet. In Fig. 3.25, the band extended toward the lower right is attributed to the outer tracks in SKS, while the band extended toward the upper right is attributed to the inner tracks in SKS.[7] A kinematical line corresponding to the $\pi^- p \to K^- \Theta^+$ reaction at 2.01 GeV/c is also indicated with black lines in the figure, assuming the Θ^+ mass of 1500 (dashed), 1530 (solid), or 1560 (dashed-dotted) MeV/c^2. The present experimental acceptance well covers the Θ^+ mass range of 1500–1560 MeV/c^2.

[7] The inner (outer) track corresponds to the events scattered to left (right) at the target in Fig. 2.6.

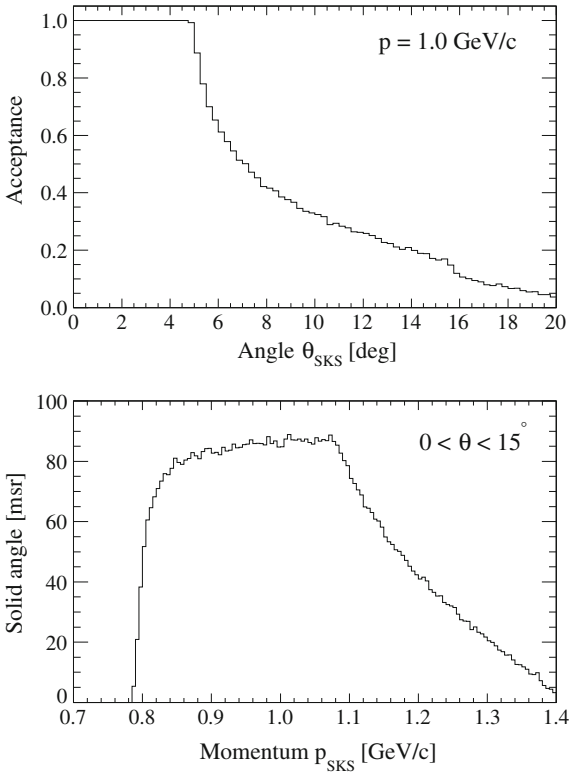

Fig. 3.26 *Top* Acceptance of SKS as a function of the incident angle (θ_{SKS}) for the momentum of 1.0 GeV/c in the Θ^+ search data. *Bottom* Solid angle of SKS as a function of the momentum for the incident angle range from 0° to 15° in the Θ^+ search data. The condition is the same as that for Fig. 3.25

Figure 3.26 (top) shows the acceptance projected onto the θ_{SKS} at the momentum of 1.0 GeV/c. In the present analysis, events with the scattering angle more than 15° were not used because of the small acceptance. Figure 3.26 (bottom) shows the solid angle of SKS as a function of the momentum for the angle range from 0° to 15°. The momentum acceptance was almost flat in the momentum range from 0.9 to 1.1 GeV/c, which corresponds to the Θ^+ missing mass region of 1500–1560 MeV/c^2.

The uncertainty of the acceptance was estimated from the statistical error in the simulation, which was controlled within typically 1 %.

3.8.3 Systematic Uncertainty

The systematic uncertainty of the cross section is summarized in Table 3.5, which was obtained from the uncertainty of the experimental efficiency and that of the SKS acceptance, described above. The uncertainties for the Θ^+ search data and the $\Sigma^{\pm}$ production data were estimated to be 7 and 6 %, respectively.

Table 3.5 Systematic uncertainty of the cross section

Data	$\Delta\varepsilon/\varepsilon$ (%)	$\Delta\Omega/\Omega$ (%)	Total (%)
$\pi^- p \to K^- \Theta^+$	6	1	7
$\pi^\pm p \to K^+ \Sigma^\pm$	5	1	6

ε and Ω denote the overall efficiency and the solid angle of SKS, respectively

Table 3.6 Forward production cross sections averaged over the scattering angles of 2–15° in the laboratory frame ($\bar{\sigma}_{2-15^\circ}$) for the $\pi^\pm p \to K^+ \Sigma^\pm$ reactions obtained in the E19-2012 data

Reaction	p_π (GeV/c)	$\bar{\sigma}_{2-15^\circ}$ (μb/sr)
$\pi^+ p \to K^+ \Sigma^+$	1.38	$274.8 \pm 8.1 \pm 17.6$
$\pi^- p \to K^+ \Sigma^-$	1.38	$51.5 \pm 2.1 \pm 3.0$
$\pi^- p \to K^+ \Sigma^-$	1.46	$40.4 \pm 0.8 \pm 2.4$

The first and second errors of the cross section denote the statistical and systematic uncertainties, respectively

3.9 Σ Production Cross Section

The validity of the cross section was examined by using the $\pi^\pm p \to K^+ \Sigma^\pm$ reactions. Table 3.6 shows the cross sections for the three data sets of the $\pi^\pm p \to K^+ \Sigma^\pm$ reactions obtained in the present experiment. The cross section averaged over scattering angles of 2–15° in the laboratory frame are defined as

$$\bar{\sigma}_{2-15^\circ} \equiv \frac{\int_{2^\circ}^{15^\circ} \left(\frac{d\sigma}{d\Omega}\right) d\Omega}{\int_{2^\circ}^{15^\circ} d\Omega}. \tag{3.34}$$

The systematic errors are from the uncertainty of the efficiency and acceptance described in Sect. 3.8.3.

Figure 3.27 shows the differential cross sections of the $\pi^+ p \to K^+ \Sigma^+$ reaction at 1.38 GeV/c, while Fig. 3.28 shows the differential cross sections of the $\pi^- p \to K^+ \Sigma^-$ reaction at 1.38 and 1.46 GeV/c. The present data are indicated by the black solid circles.[8] The cross sections reported in the previous 2010 data [9, 11] and other previous experiments [12–14] are also shown. The present data are in reasonable agreement with both the 2010 data and the other previous experimental data. Furthermore, the E19 data provided the Σ production cross section at forward angles more precisely than any previous experimental data.

[8] The differential cross sections in the c.m. frame are presented in Appendix D.

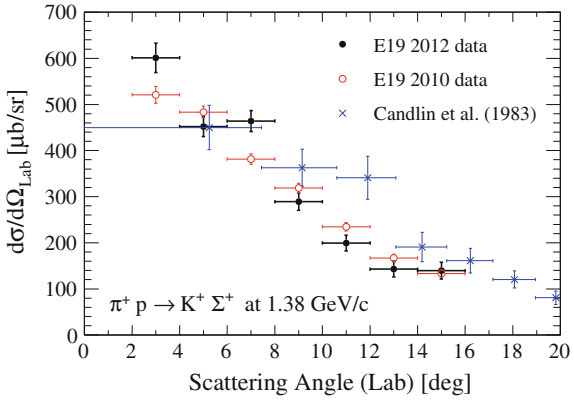

Fig. 3.27 Differential cross sections for the $\pi^+ p \rightarrow K^+ \Sigma^+$ reaction at 1.38 GeV/c. The *black solid circles* are the present E19-2012 data at 1.38 GeV/c. The *red open circles* are the E19-2010 data at 1.375 GeV/c [9, 11]. The *blue crosses* are the data from Candlin et al. [12] at 1.377 GeV/c, converted from the c.m. frame to the laboratory one. The quoted errors are statistical only. The present data are tabulated in Table D.1

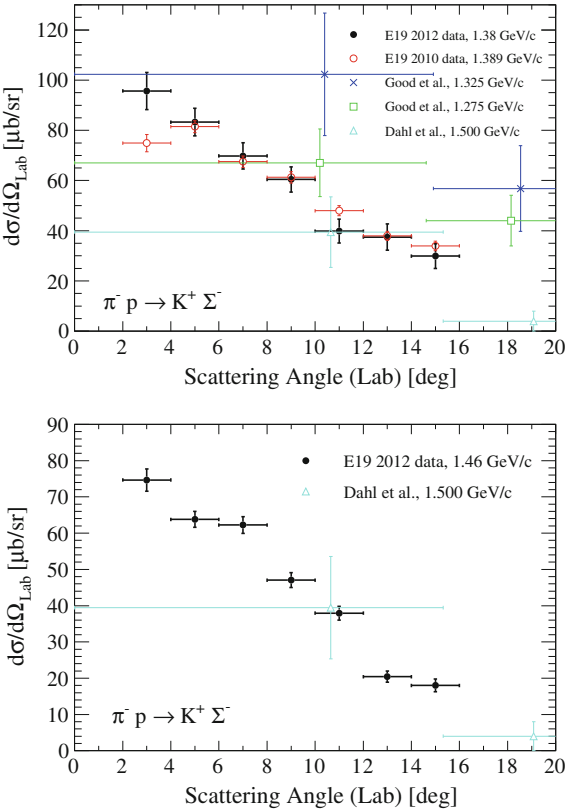

Fig. 3.28 Differential cross sections for the $\pi^- p \rightarrow K^+ \Sigma^-$ reaction. *Top* The *black solid circles* are the present E19-2012 data at 1.38 GeV/c. The *red open circles* are the E19-2010 data at 1.389 GeV/c [9]. The *blue crosses* and the *green open squares* are the data from Good et al. [13] at 1.325 and 1.275 GeV/c, respectively. The *cyan open triangles* are the data from Dahl et al. [14] at 1.500 GeV/c. *Bottom* The *black solid circles* are the present E19-2012 data at 1.46 GeV/c. The *cyan open circles* are the same as those of the *top figure*. The quoted errors are statistical only. The present data are tabulated in Table D.1

References

1. S. Morinobu (private communication)
2. F. James, MINUIT–Function minimization and error analysis, CERN-D506 (1994)
3. J. Myrheim, L. Bugge, Nucl. Instrum. Meth. **160**, 43 (1979)
4. ANSYS, http://www.ansys.com
5. J. Beringer et al., Particle data group. Phys. Rev. D **86**, 010001 (2012)
6. K.L. Brown, Ch. Iselin, CERN 74–2 (1974); U. Rohrer, Compendium of decay turtle enhancements, PSI
7. K. Aoki et al., Phys. Rev. C **76**, 024610 (2007)
8. T. Takahashi et al., Phys. Rev. C **51**, 2542 (1995)
9. K. Shirotori, Ph.D. thesis, Tohoku University (2011)
10. S. Agostinelli et al., Nucl. Instrum. Meth. A **506**, 250 (2003); J. Allison et al., IEEE Trans. Nucl. Sci. **53**, 270 (2006)
11. K. Shirotori et al., J-PARC E19 collaboration. Phys. Rev. Lett. **109**, 132002 (2012)
12. D.J. Candlin et al., Nucl. Phys. B **226**, 1 (1983)
13. M.L. Good, R.R. Kofler, Phys. Rev. **183**, 1142 (1969)
14. O.I. Dahl et al., Phys. Rev. **163**, 1430 (1967)

Chapter 4
Results

4.1 Missing Mass Spectrum

The missing mass spectrum of the $\pi^- p \rightarrow K^- X$ reaction at a beam momentum of 2.01 GeV/c at scattering angles of 2°–15° in the laboratory frame is shown in Fig. 4.1. The spectrum has no distinct structure, and no clear peak was observed. Comparing with the previous 2010 data shown in Fig. 1.12, the missing mass acceptance became wider owing to the improved experimental setup as described in Sect. 2.4.

4.2 Background Processes

The background events remaining in the missing mass spectrum of the $\pi^- p \rightarrow K^- X$ reaction shown in Fig. 4.1 are discussed in this section. The scattered pion contamination, which is due to the misidentification of outgoing kaons with pions, was estimated to be 1.9 % in a central missing mass region of 1500–1560 MeV/c^2, as described in Sect. 3.3.2. The background events from materials surrounding the LH_2 target were estimated to be less than 3 %, as described in Sect. 3.4. Since these background components are controlled within small fractions, the remaining background events ought to originate from physical background processes.

In the $\pi^- p \rightarrow K^- X$ reaction, several physical background processes are associated with the Θ^+ production. The $\pi^- p \rightarrow \bar{K} K N$ reaction at a beam momentum of 1.8–2.2 GeV/c was reported by Dahl et al. [1] using a hydrogen bubble chamber. In this momentum region around 2 GeV/c, the main physical processes are the following three reactions:

$$\pi^- p \rightarrow \phi\, n \rightarrow K^- K^+ n, \tag{4.1}$$

$$\pi^- p \rightarrow \Lambda(1520)\, K^0 \rightarrow K^- K^0 p, \tag{4.2}$$

$$\pi^- p \rightarrow K^- K^+ n \text{ or } K^- K^0 p \text{ (nonresonant)}. \tag{4.3}$$

M. Moritsu, *Search for the Pentaquark Θ^+ via the $\pi^- p \rightarrow K^- X$ Reaction at J-PARC*, Springer Theses, DOI 10.1007/978-981-10-0012-6_4

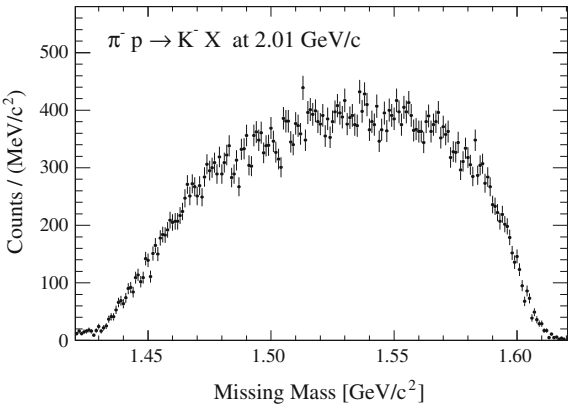

Fig. 4.1 Missing mass spectrum of the $\pi^- p \rightarrow K^- X$ reaction at 2.01 GeV/c at scattering angles of 2°–15°. The quoted errors are statistical

Since other higher excited Λ^* and Σ^* resonances were not observed in [1], we assumed the cross section of these resonances is small and neglected the contributions.[1]

The background event should include a K^- in the three-body final state detected in the spectrometer acceptance. Since the SKS is a single-arm spectrometer which is dedicated to the high-resolution measurement of K^-, we could not detect the other particles in the final state. The missing mass spectrum of the $\pi^- p \rightarrow K^- X$ reaction includes the reflections of the ϕ and $\Lambda(1520)$ productions together with the nonresonant components.

The background distribution should be reproduced by a MC simulation taking account of the three reactions (4.1–4.3). The cross sections and angular distributions of the reactions (4.1) and (4.2) were taken from previous experiments [1, 2]. The total cross section of the $\pi^- p \rightarrow \phi n$ reaction was measured to be 30.0 ± 8.0 and 21 ± 7 μb for incident momenta of 1.8–2.2 [1] and 2.0 GeV/c [2], respectively. The weighted-average of these values, 25 ± 5 μb, was used for the simulation. The isotropic angular distribution of both the production and decay of ϕ was used in the simulation as reported in [1, 2]. The total cross section of the $\pi^- p \rightarrow \Lambda(1520) K^0 \rightarrow N \bar{K} K^0$ reaction was measured to be 20.8 ± 5.0 μb for an incident momentum of 1.8–2.2 GeV/c [1]. According to [1], the angular distributions of the production and the decay of $\Lambda(1520)$ were used in the simulation such as $\frac{1-\cos\theta}{2}$ and $\frac{1}{3} + \cos^2\theta$, respectively. Since there was no reliable information on the nonresonant cross sections, the amplitude of the nonresonant productions were normalized to the present experimental data. Because of the same spectrum shape of the nonresonant $K^- K^+ n$ and $K^- K^0 p$, these spectra are represented by an unified spectrum as nonresonant $\bar{K} K N$, hereafter.

Figure 4.2 shows simulated missing mass spectra of the $\pi^- p \rightarrow K^- X$ reaction for the background processes together with the present experimental data. The nonresonant $\bar{K} K N$ production is dominant in the present reaction. In the missing mass

[1] The Λ^* and Σ^* contributions are reconsidered in Appendix E.

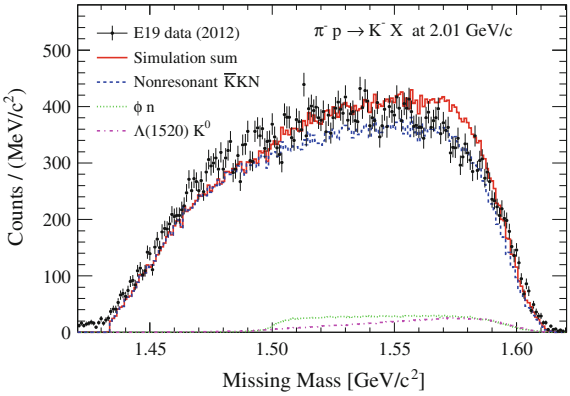

Fig. 4.2 Missing mass spectrum of the $\pi^- p \rightarrow K^- X$ reaction at 2.01 GeV/c. The experimental data are indicated by the *black* points with statistical errors. The *red* histogram represents the total background shape obtained by the MC simulation including three processes: nonresonant $\bar{K}KN$ (*blue dashed*), ϕ-intermediated $K^- K^+ n$ (*green dotted*) and $\Lambda(1520)$-intermediated $K^- K^0 p$ (*magenta dashed-dotted*). The scale of the nonresonant components was normalized to the experimental data

spectra, the low-mass edges (1.43 GeV/c^2 for nonresonant and 1.50 GeV/c^2 for ϕ and $\Lambda(1520)$) are restricted from the maximum K^- momenta kinematically allowed in the reactions, while the high-mass edge at 1.61 GeV/c^2 is from the minimum K^- momentum accepted in SKS. Note that the background spectra do not make any sharp structure in the missing mass spectrum. Therefore, we can represent the background shape with a smooth function such as polynomial functions, especially in a central missing mass region of 1500–1560 MeV/c^2.

4.3 Upper Limit of Production Cross Section

4.3.1 Upper Limit

Figure 4.3 shows the missing mass spectrum of the $\pi^- p \rightarrow K^- X$ reaction at 2.01 GeV/c after the experimental efficiency and acceptance correction. The ordinate represents the differential cross section averaged over 2°–15° in the laboratory frame (as defined in Eq. (3.34)). The missing mass spectrum for each angle region at 2° intervals is also shown in Fig. 4.4. Since the efficiency and acceptance are almost flat except for the acceptance edges as described in Sect. 3.8, the spectrum shape does not change so much and still has no distinct structure. In particular, as shown in Sect. 3.8.2, the momentum acceptance of SKS is flat in a range of 0.9–1.1 GeV/c, which corresponds to a missing mass range of 1500–1560 MeV/c^2. The mass of Θ^+ reported in experiments with positive evidence ranged from 1520 to 1550 MeV/c^2.

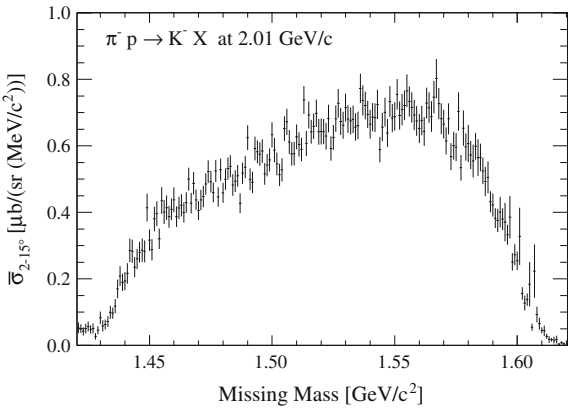

Fig. 4.3 Missing mass spectrum of the $\pi^- p \rightarrow K^- X$ reaction at 2.01 GeV/c. The ordinate represents the differential cross section averaged over 2–15° in the laboratory frame. The quoted errors are statistical only

Thus, we evaluated the upper limit of the Θ^+ production cross section in a mass region of 1500–1560 MeV/c^2.

As shown in Fig. 4.5 (top), the spectrum was fitted with a background plus signal function. The background function is a second-order polynomial function defined in a mass range of 1495–1565 MeV/c^2. The signal function is a Gaussian distribution with a fixed width of 2.13 MeV (FWHM), which is the experimental resolution evaluated in Sect. 3.7.4. The natural width for the Θ^+ was ignored in the fitting, because the Θ^+ must have very small width. In the figure, the error bar at each point indicates only the statistical uncertainty. The systematic uncertainty, which came from the efficiency and acceptance correction, is almost common within a local mass range of a few MeV/c^2. The systematic uncertainty is discussed later. Hence, the fitting result provides an estimation of the effect only from statistical fluctuation.

The fitting was carried out for every assumed peak position from 1500–1560 MeV/c^2 with 1-MeV step. The cross section was calculated from the area of the signal function. The results are plotted with black points as a function of masses in Fig. 4.5 (bottom). In the confidence level estimation, we assumed a Gaussian distribution where an unphysical region corresponding to negative cross section was excluded; i.e., the upper limit at the 90 % C.L., x_{up}, was obtained from

$$\frac{\int_0^{x_{\mathrm{up}}} G(x;\mu,\sigma)dx}{\int_0^{\infty} G(x;\mu,\sigma)dx} = 0.9, \tag{4.4}$$

where $G(x;\mu,\sigma)$ is a Gaussian function with a mean μ and a standard deviation σ, which correspond to the obtained cross section and the uncertainty. The upper limit at the 90 % C.L. was obtained as a function of masses as shown with a red line in Fig. 4.5 (bottom). The upper limit was found to be at most 0.28 μb/sr in the mass region of 1500–1560 MeV/c^2.

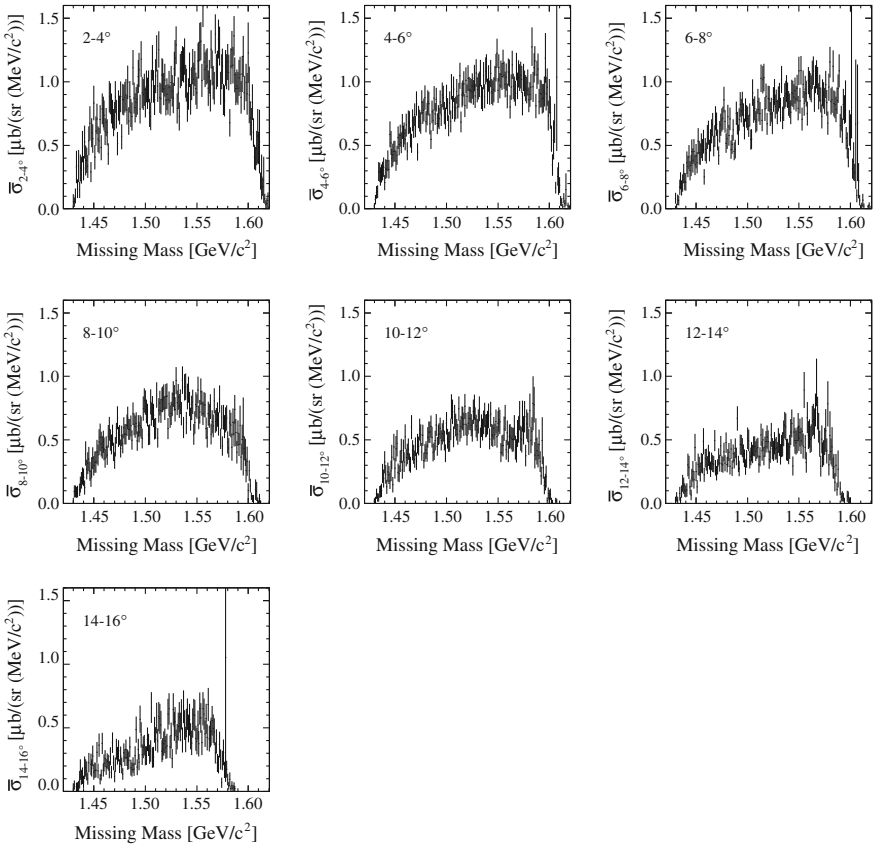

Fig. 4.4 Missing mass spectrum of the $\pi^- p \rightarrow K^- X$ reaction at 2.01 GeV/c for each angle region. The ordinate represents the differential cross section averaged over the angle region at 2° intervals in the laboratory frame. The quoted errors are statistical only

4.3.2 Systematic Uncertainty

The systematic uncertainties on the upper limit of the cross section are discussed here. The following components can be a source of the uncertainty;

- The systematic uncertainty of the efficiency and acceptance correction was discussed in Sect. 3.8.3. The upper limit of the cross section is affected by this uncertainty of 7 % over the mass region of 1500–1560 MeV/c^2.
- The width of the signal Gaussian peak was fixed to the missing-mass resolution of 2.13 MeV (FWHM) in the above fitting. As described in Sect. 3.7.4, the uncertainty of the missing-mass resolution was estimated to be ±0.15 MeV. The dependence of the upper limit on the missing-mass resolution was examined as shown in Fig. 4.6 (top). The uncertainty of ±0.15 MeV corresponds to deviations of ±0.012 μb/sr

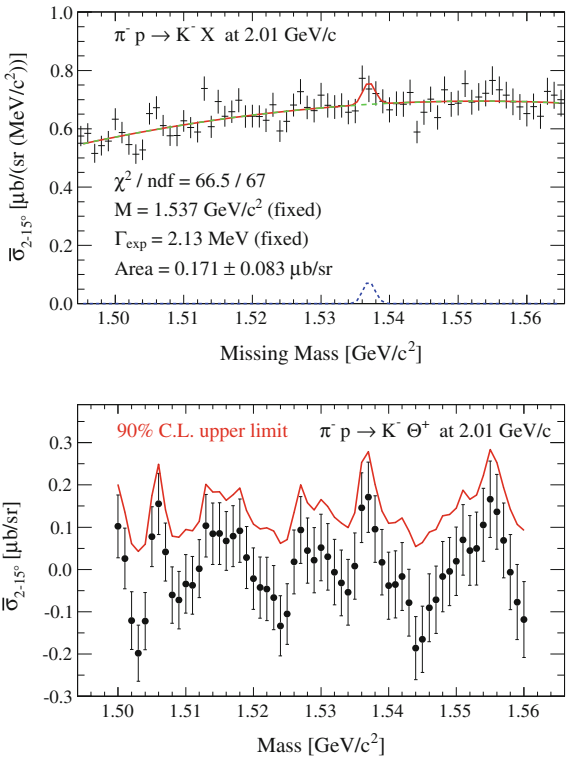

Fig. 4.5 (*Top*) Missing mass spectrum of the $\pi^- p \rightarrow K^- X$ reaction at 2.01 GeV/c in the mass region of the Θ^+ search. The quoted errors of the data are statistical. A fitting result at the mass of 1537 MeV/c^2 is also shown. The fitting function (*red solid*) is a second-order polynomial (*green dashed*) with a Gaussian peak (*blue dotted*) whose width is fixed at the experimental resolution of 2.13 MeV. (*Bottom*) Allowed signal yields for each mass. The error bars denote the statistical uncertainty. The red line indicates the upper limit at the 90 % C.L

at the maximum upper limit of 0.28 μb/sr, as shown in red and blue solid lines in the figure. Therefore, the missing-mass resolution uncertainty has at most 4 % influence upon the upper limit.

- The uncertainty due to the background shape was examined by applying a third-order polynomial function instead of the second-order one as shown in Fig. 4.6 (bottom). The difference was less than 0.005 μb/sr and found to be negligibly small. This means that it is reasonable enough to use the second-order polynomial function as the background shape.

Considering the above three kinds of uncertainties, the systematic uncertainty on the upper limit of the cross section was found to be controlled within 10 %. This means that the present upper limit is predominantly determined by the statistics of the experimental data.

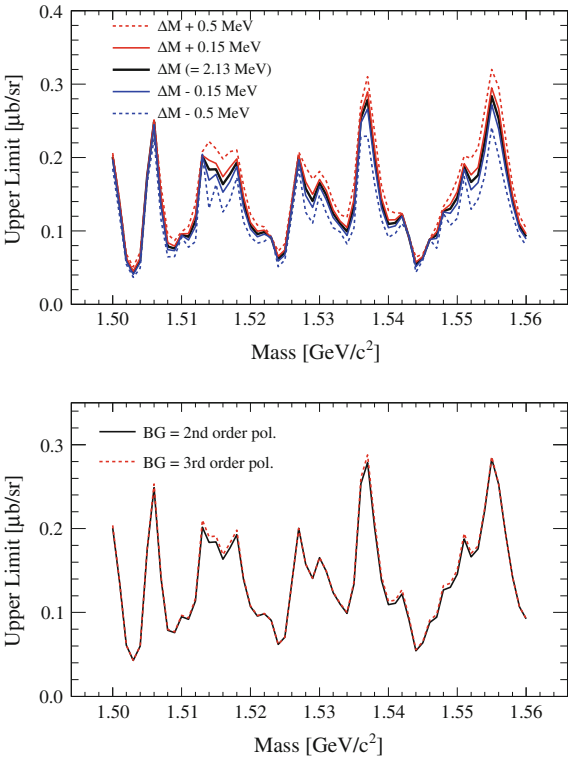

Fig. 4.6 (*Top*) Dependence of the upper limit on the missing-mass resolution. The *black solid line* is the upper limit obtained with the expected missing mass resolution ($\Delta M = 2.13$ MeV). The *red* and *blue solid lines* correspond to the upper limits with 1σ-deviated mass resolutions (± 0.15 MeV). The *red* and *blue dashed lines* correspond to the upper limits with $\Delta M \pm 0.5$ MeV. (*Bottom*) Dependence of the upper limit on the background function. The black solid line is the upper limit obtained with the second-order polynomial function, while the *red dashed line* is that of the third-order one

4.3.3 Dependence on the Θ^+ Width

The natural width of Θ^+ was ignored in the above fitting, because the Θ^+ must have very small width. The dependence of the upper limit on the natural width of Θ^+ is discussed here. The width of Θ^+ was implemented with the Breit-Wigner distribution convoluted by the Gaussian with the experimental resolution of 2.13 MeV (FWHM). The signal function in the fitting was replaced with the Breit-Wigner distribution smeared by the Gaussian. Figure 4.7 shows the upper limits with assumed widths of 0–1.0 MeV. The upper limit rises by 0.10 μb/sr at most, if the Θ^+ width is 1 MeV.

4.3.4 Summary of the 2012 and 2010 Data

The present upper limit obtained in the 2012 data at an incident momentum of 2.01 GeV/c was compared with that of the 2010 data at 1.92 GeV/c. For the 2010 data, the upper limit was reevaluated with an updated missing-mass resolution of

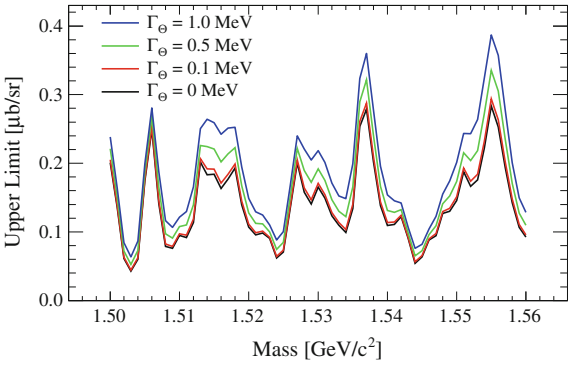

Fig. 4.7 Θ^+-width dependence of the upper limit. The *solid lines* represent the upper limits with assumed Θ^+ widths of 0 (*black*), 0.1 (*red*), 0.5 (*green*), and 1.0 (*blue*) MeV

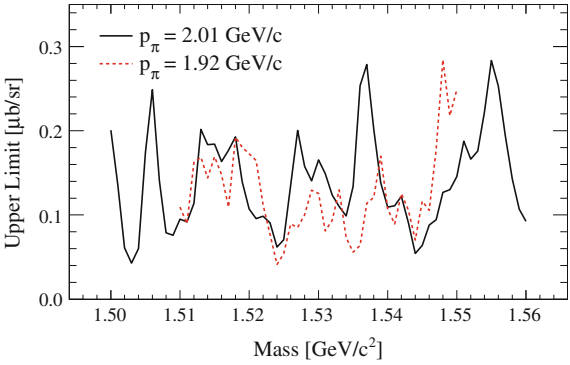

Fig. 4.8 Comparison of the upper limits in the 2012 and 2010 data. The *black solid (red dashed) line* indicates the upper limit in the 2012 (2010) data with the incident momentum of 2.01 (1.92) GeV/*c* using the missing mass resolution of 2.13 (1.72) MeV. The difference of the mass range is due to the difference of the missing mass acceptance

1.72 MeV [3], which was previously estimated as 1.44 MeV [4].[2] The upper limits obtained in the 2012 and 2010 data are shown in Fig. 4.8 with black solid and red dashed lines, respectively, in case of the Θ^+ natural width of 0 MeV. The available mass range of 1500–1560 MeV/c^2 in the 2012 data is wider than that of 1510–1550 MeV/c^2 in the 2010 data, owing to the improved experimental acceptance. The upper limits in the both data are on the same level and less than 0.28 μb/sr. This is attributed to almost the same statistics of the both data, and the resolution difference of 2.13 versus 1.72 MeV does not have much influence.

[2]The missing-mass resolution of 1.44 MeV was estimated by assuming $\Delta p_B/p_B = 5.2 \times 10^{-4}$ (FWHM), which was calculated by the first-order transport matrix with a tracker position resolution of 0.2 mm and by fluctuation of the magnetic field. We found that this underestimated the resolution of the beam spectrometer.

References

1. O.I. Dahl et al., Phys. Rev. **163**, 1377 (1967)
2. H. Courant et al., Phys. Rev. D **16**, 1 (1977)
3. T. N. Takahashi, Ph.D. thesis, University of Tokyo, 2014
4. K. Shirotori, Ph.D. thesis, Tohoku University, 2011

Chapter 5
Discussion

5.1 Upper Limit of the Θ^+ Width

The narrowness of the width is the most peculiar property to the Θ^+ pentaquark. It is a big issue for any theoretical models to interpret the narrow width in a viewpoint of the internal structure of the hadron. The width of Θ^+ should be less than a few MeV at least on the basis of past K^+d scattering data, and the Belle Collaboration obtained the upper limit of 0.64 MeV [1]. Only the DIANA Collaboration claims a finite value of 0.34 ± 0.10 MeV [2], which is extraordinarily small as the width for strongly decaying hadrons.

As described in Sect. 1.5, the production mechanism of Θ^+ in the $\pi^- p \to K^- \Theta^+$ reaction was studied in several theoretical calculations using the effective Lagrangian approach as shown in Fig. 1.10a–c. They suggest that the contributions of the t-channel process and contact term must be very small from the KEK E522 and E559 results. Therefore, the s-channel contribution is important in the $\pi^- p \to K^- \Theta^+$ reaction. Since the s-channel amplitude is related to the Θ^+ decay width through the coupling constant $g_{KN\Theta}$, we are able to estimate the width from the cross section measured in the experiment. From the present null result, the upper limit of the Θ^+ width can be derived.

In this section, we evaluate the upper limit of the Θ^+ width using both the 2010 and 2012 data together with a theoretical calculation. The theoretical framework is described in the next subsection. Using the theoretical prescription, the upper limit of the width is estimated in the subsequent subsection. Finally, we discuss the obtained result comparing with other experimental results.

5.1.1 Theoretical Calculation

Several theoretical groups discussed the production mechanism of Θ^+ in the $\pi^- p \to K^- \Theta^+$ reaction using the effective Lagrangian approach, which was described in

M. Moritsu, *Search for the Pentaquark Θ^+ via the $\pi^- p \to K^- X$ Reaction at J-PARC*, Springer Theses, DOI 10.1007/978-981-10-0012-6_5

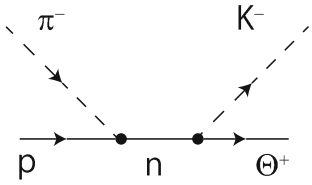

Fig. 5.1 s-channel diagram for the $\pi^- p \to K^- \Theta^+$ reaction

Sect. 1.5. Recently, Hyodo et al. have published a comprehensive calculation [3], which can be directly compared to our experimental result. They considered only the nucleon pole term which corresponds to the s-channel diagram in the $\pi^- p \to K^- \Theta^+$ reaction as shown in Fig. 5.1. Their calculation was performed for the isosinglet Θ^+ with the spin-parity $J^P = 1/2^{\pm}$ and $3/2^{\pm}$ cases.

In the $3/2^{\pm}$ cases, the width corresponding to the upper limit of the previous experiment [4] becomes much smaller than 1 MeV in their calculation, which is too narrow to be understood as a strongly decaying hadron. Therefore, the $3/2^{\pm}$ cases are highly disfavored in their calculation. Hence, only the $1/2^{\pm}$ cases are discussed in the following.

To evaluate the diagram in Fig. 5.1, the Yukawa couplings for the $KN\Theta$ and πNN vertices are needed for the effective interaction Lagrangian. They introduced two schemes for the Yukawa couplings, namely pseudoscalar (PS) and pseudovector (PV) schemes. For the πNN coupling, the former and latter correspond to the linear and nonlinear representations of the chiral symmetry, respectively. The difference of results in the two schemes are regarded as a theoretical uncertainty. The interaction Lagrangians in the PS scheme are given by

$$\mathcal{L}^{1/2^{\pm}}_{KN\Theta} = g^{1/2^{\pm}}_{KN\Theta} \bar{\Theta} \Gamma K N + \text{h.c.}, \tag{5.1}$$

$$\mathcal{L}_{\pi NN} = i g_{\pi NN} \bar{N} \gamma_5 \pi N, \tag{5.2}$$

where $\Gamma = 1$ for the negative parity case and $\Gamma = i\gamma_5$ for the positive parity case. The $KN\Theta$ coupling constant is determined by the Θ^+ decay width Γ_Θ as

$$g^{1/2^{\pm}}_{KN\Theta} = \sqrt{\frac{2\pi m_\Theta \Gamma_\Theta}{q(E_N \mp m_N)}}, \tag{5.3}$$

where m_Θ and m_N are the mass of the Θ^+ and the nucleon, respectively; q is the momentum of K or N in the Θ^+ decay; and $E_N = \sqrt{q^2 + m_N^2}$. The interaction Lagrangians in the PV scheme are the derivative couplings:

$$\mathcal{L}^{1/2^{\pm}}_{KN\Theta} = \frac{-i g_A^{*\pm}}{2f} \bar{\Theta} \gamma_\mu \Gamma \partial^\mu K N + \text{h.c.}, \tag{5.4}$$

$$\mathcal{L}_{\pi NN} = \frac{g_A}{2f} \bar{N} \gamma_\mu \gamma_5 \partial^\mu \pi N, \tag{5.5}$$

where f is the meson decay constant, and g_A is the axial coupling constant of the nucleon. The transition axial coupling constant, g_A^*, for the $\Theta^+ \to N$ is related to the $g_{KN\Theta}$ through the generalized Goldberger–Treiman relation as [5]

$$g_A^{*\pm} = \frac{2f}{m_\Theta \pm m_N} g_{KN\Theta}^{1/2^\pm}. \tag{5.6}$$

The theoretical constants were determined based on known hadron reactions except for the unknown $KN\Theta$ coupling constant. Their calculation adopted standard values such as $g_{\pi NN} = 13.5, f = 93\,\text{MeV}$, and $g_A = 1.25$.

In addition, they introduced a phenomenological form factor, which reflects the finite size of the hadrons, in each vertex. They examined two types of from factors, namely the static (F_s) and covariant (F_c) type form factors. The difference of results in the two form factors are also regarded as a theoretical uncertainty. The static form factor is the three momentum monopole type, defined as

$$F_s = \frac{\Lambda_s^2}{\Lambda_s^2 + |\boldsymbol{k}|^2}, \tag{5.7}$$

where $\boldsymbol{k}$ is the incident pion momentum in the c.m. frame, and Λ_s denotes a cut-off value. The covariant form factor is often used in photoproduction processes, defined as

$$F_c = \frac{\Lambda_c^4}{\Lambda_c^4 + (s - m_N^2)^2}, \tag{5.8}$$

where s is the squared total energy, and Λ_c denotes a cutoff value. The cutoff values were determined based on known hyperon production reactions as $\Lambda_s = 0.5\,\text{GeV}$ and $\Lambda_c = 1.8\,\text{GeV}$.

According to this prescription, the total cross section of the $\pi^- p \to K^- \Theta^+$ reaction was calculated as shown in Fig. 1.13. The calculated differential cross sections are shown in Fig. 5.2 at an incident momentum of $2.0\,\text{GeV}/c$ for $J^P = 1/2^\pm$ assuming $\Gamma_\Theta = 1\,\text{MeV}$. One can see that the cross section for $1/2^+$ is larger than that for $1/2^-$ as a general tendency. This can be understood by a parity dependence of the coupling constant shown in Eq. (5.3); the coupling constant for $1/2^+$ is larger than that for $1/2^-$ for Γ_Θ being fixed. This is essentially attributed to the partial wave of the $\Theta^+ \to KN$ decay. Θ^+ decays in $s(p)$-wave in $1/2^-(1/2^+)$ case. In general, a decay width is suppressed in a higher partial wave for the coupling constant being fixed.

Since the amplitude for the s-channel diagram is proportional to the $KN\Theta$ coupling constant, the cross section (σ_Θ) is simply proportional to the width of Θ^+:

$$\frac{d\sigma_\Theta}{d\Omega} \propto g_{KN\Theta}^2 \propto \Gamma_\Theta, \tag{5.9}$$

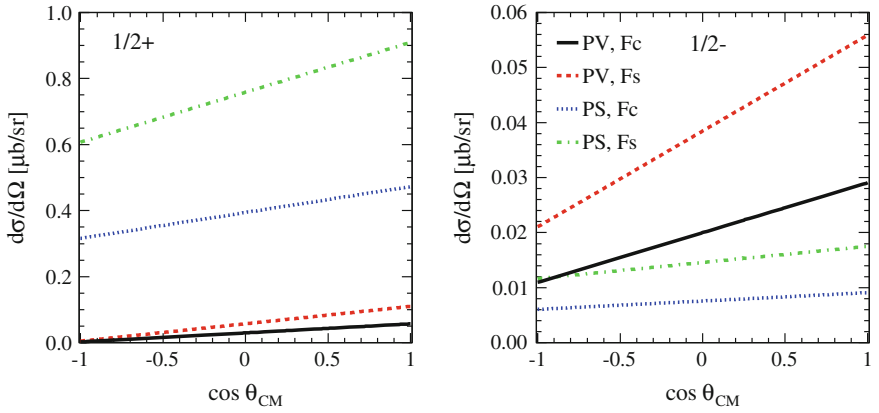

Fig. 5.2 Differential cross sections of the $\pi^- p \to K^- \Theta^+$ reaction calculated by Hyodo, Hosaka, and Oka [3, 6] at an incident momentum of 2.0 GeV/c, the Θ^+ mass of 1540 MeV, and the Θ^+ width of 1 MeV for the spin-parity of $1/2^+$ (*left*) and $1/2^-$ (*right*). Each line indicates the different theoretical treatments: pseudoscalar (PS) or pseudovector (PV) couplings, and static (F_s) or covariant (F_c) types of form factors (see text)

Thus, the cross section is written as

$$\frac{d\sigma_\Theta}{d\Omega} = k_{C,F}\,(p_\pi, m_\Theta)\;\; \Gamma_\Theta, \tag{5.10}$$

where the coefficient k is obtained in each coupling scheme (C), PS or PV, and form factor (F), F_s or F_c. k is a function of the incident momentum p_π and the Θ^+ mass m_Θ. The differential cross section was calculated at the incident momenta of 1.92 and 2.00 GeV/c and at the Θ^+ masses between 1510 and 1550 MeV/c^2 at 10 MeV/c^2 intervals.

5.1.2 *Upper Limit Estimation*

From the E19 experimental results, two structureless missing-mass spectra at the incident momenta of 1.92 and 2.01 GeV/c were obtained. The upper limit of the Θ^+ width was estimated by using the two spectra comparing with the theoretical calculation described above including the incident momentum dependence of the cross section. This incident momentum dependence provides an useful information in addition to the increased statistics, when we estimate the upper limit of the width by a simultaneous fitting of the 2010 and 2012 data.

For a direct comparison with the experimental data, the differential cross section averaged over the scattering angles of 2°–15° in the laboratory frame was calculated according to the above calculation. The calculated coefficient k in Eq. (5.10) for each momentum and mass was an input of the following fitting. As shown in

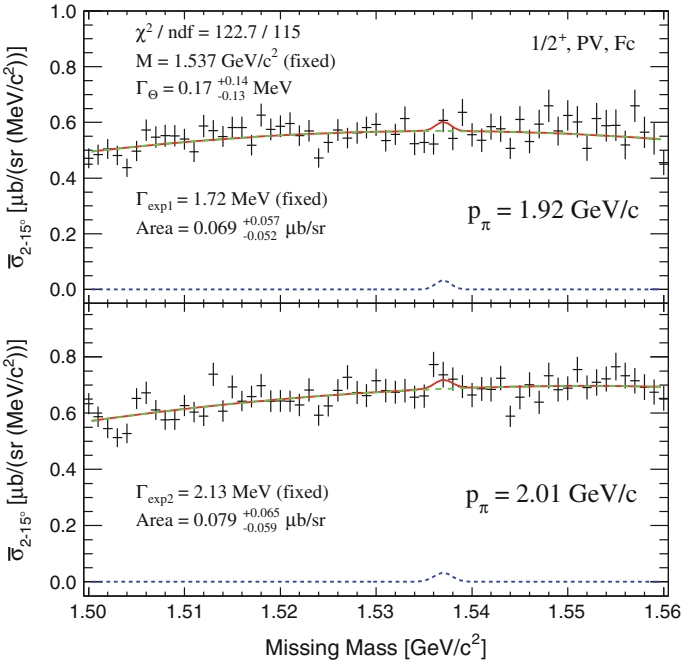

Fig. 5.3 Missing mass spectra of the $\pi^- p \to K^- X$ reaction at 1.92 (*top*) and 2.01 GeV/c (*bottom*) in the mass region of the Θ^+ width fitting. The quoted errors of the data are statistical. The fitting was simultaneously applied to the both spectra with respect to a common width parameter Γ_Θ. A fitting result at the mass of 1537 MeV/c^2 for $J^P = 1/2^+$, the PV scheme and the F_c form factor case is shown. The fitting function (*red solid*) is defined as second-order polynomials (*green dashed*) with the Breit–Wigner peak convoluted by a Gaussian (*blue dotted*) whose width is fixed at the experimental resolution of 1.72 or 2.13 MeV

Fig. 5.3, both experimental data of 1.92 and 2.01 GeV/c were simultaneously fitted with respect to a common width parameter Γ_Θ. The top panel shows the 2010 data at 1.92 GeV/c, while the bottom panel shows the 2012 data at 2.01 GeV/c. A signal function is the Breit–Wigner distribution convoluted by a Gaussian distribution. The Breit–Wigner width represents the parameter Γ_Θ, which is common for each data. The Gaussian width represents the experimental resolutions, which were fixed at 1.72 and 2.13 MeV (FWHM) for the 1.92- and 2.01-GeV/c data, respectively. The signal cross section for each data is a function of the common parameter Γ_Θ, as given in Eq. (5.10). We allowed both positive and negative cross sections in fitting the spectra. In case of the negative cross section, the signal function was a Gaussian with the experimental resolution and negative height. A background function is a second-order polynomial function defined in a mass range of 1500–1560 MeV/c^2, whose coefficients are independently determined in each data.

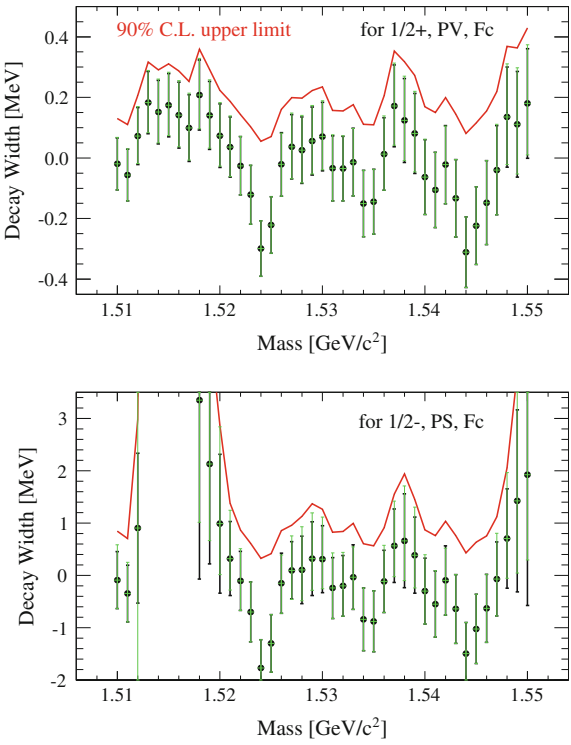

Fig. 5.4 Results of the Θ^+ width fitting for $J^P = 1/2^+$, the PV scheme and the F_c form factor case (*top*), and for $J^P = 1/2^-$, the PS scheme and the F_c form factor case (*bottom*). The *black points* with symmetric error bars are the obtained widths with approximate errors estimated by the parabolic assumption, while the *green* asymmetric error bars denote the 1σ errors estimated in an accurate way. The *red line* indicates the upper limit at the 90 % C.L. based on the approximate errors

Considering the narrower mass range of the 2010 data, the search range was determined as 1510–1550 MeV/c^2. The fitting was carried out for every assumed peak position from 1510 to 1550 MeV/c^2 with 1-MeV step. Figure 5.4 (top) shows the fitting result of the Θ^+ width for $J^P = 1/2^+$, the PV scheme and the F_c form factor case, while Fig. 5.4 (bottom) shows the fitting result for $J^P = 1/2^-$, the PS scheme and the F_c form factor case. Since the fitting is nonlinear due to the constraint of Eq. (5.10), the estimated errors of the fitting are asymmetric as shown with green error bars in the figure. This asymmetry is enhanced when the fitting result of the width become larger. It is not negligible especially outside a range around 1530 or 1540 MeV/c^2 in the $1/2^-$ case. However, in the $1/2^+$ case and in the mass region around 1530 and 1540 MeV/c^2 for the $1/2^-$ case, the deviation from the approximate errors estimated by the parabolic assumption,[1] which is symmetric as shown with black error bars in the figure, is small: <0.013 MeV for the $1/2^+$ case, and <0.15 MeV for the $1/2^-$ case. Therefore, the upper limit at the 90 % C.L. was simply estimated by using the approximate errors in the same manner as described in Sect. 4.3, excluding an unphysical region of negative width.

[1]The approximate error is estimated by using the curvature at the minimum of the χ^2 function and assuming a parabolic shape [7].

The above procedure was carried out for every case of the spin-parity ($1/2^{\pm}$), coupling scheme (PS or PV) and form factor (F_s or F_c). Figure 5.5 shows the obtained upper limits on the Θ^+ width for each theoretical scheme and spin-parity. The width upper limit curves are placed in reverse order to the cross sections shown in Fig. 5.2, where the width is being fixed. Since the difference among each scheme is a theoretical uncertainty, we took the most conservative one, where the result gives the largest upper limit. In the $1/2^+$ case (Fig. 5.5 top), the PV scheme with the F_c form factor gives the largest upper limits. The upper limits of the width are less than 0.36 MeV in almost the entire mass region of 1510–1550 MeV/c^2. The $1/2^-$ case (Fig. 5.5 bottom) shows relatively larger widths than the $1/2^+$ case. This can be understood by the relation between the width and the cross section (Eq. 5.3) described in Sect. 5.1.1. Equation (5.3) allows the width to become larger keeping a small cross section especially in the $1/2^-$ case. The PS scheme with the F_c form factor gives the largest upper limits in the $1/2^-$ case. The upper limits of the width are less than 1.9 MeV in the mass region around 1530 or 1540 MeV/c^2, whereas the sensitivity is not sufficient outside this region.

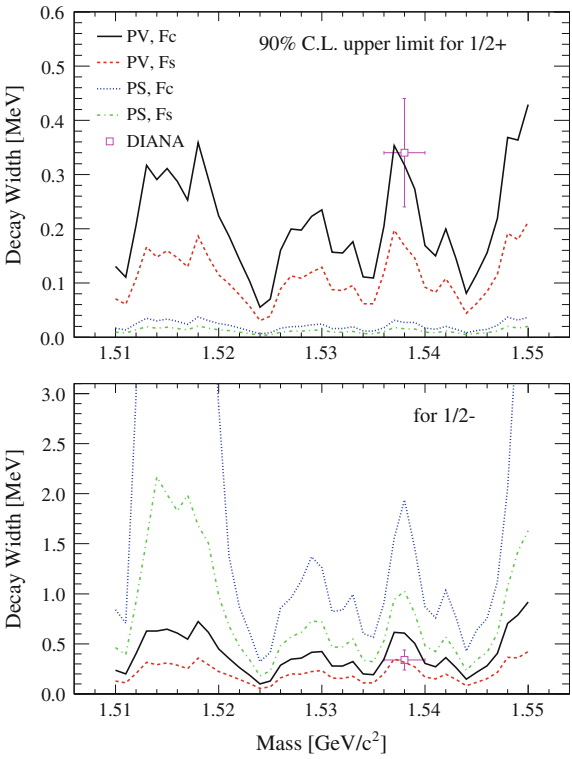

Fig. 5.5 Upper limits at the 90 % C.L. on the Θ^+ decay width for the spin-parity of $1/2^+$ (*top*) and $1/2^-$ (*bottom*) case. Each line indicates the different theoretical treatments: pseudoscalar (PS) or pseudovector (PV) couplings, and static (F_s) or covariant (F_c) types of form factors. The DIANA result [2] is also indicated by the *open square* (*magenta*)

5.1.2.1 Systematic Uncertainty

The systematic uncertainties on the upper limit of the width caused by the spectrum fitting was examined. The missing mass has a systematic uncertainty due to the mass scale calibration. As described in Sect. 3.6.4, the missing mass scale uncertainty was estimated to be 1.4 MeV for the 2.01-GeV/c data. The corresponding value for the 1.92-GeV/c data is 1.7 MeV [8, 9]. These values were assumed to be independent, because the 2010 and 2012 run are independent experiments. The missing mass scales were shifted by δm_1 and δm_2 in the 1.92- and 2.01-GeV/c data, respectively. Figure 5.6 shows the upper limits of the width when the mass scale was shifted by ± 1.5 MeV. The upper limits could vary by ± 30 and $^{+10}_{-30}$ % in the $1/2^+$ and $1/2^-$ cases, respectively.

5.1.3 *Discussion on the Present Upper Limit*

As described above, the upper limits of the Θ^+ width at the 90 % C.L. were estimated to be 0.36 and 1.9 MeV for the spin-parity of $1/2^+$ and $1/2^-$, respectively. The upper

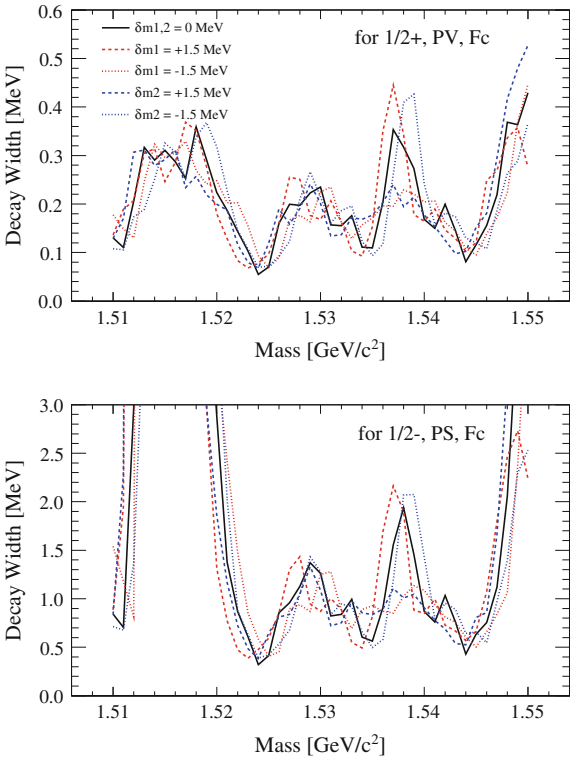

Fig. 5.6 Investigation of the systematic uncertainty of the upper limit of the Θ^+ width from the missing mass scale uncertainties. The *top figure* shows the $1/2^+$ case with the PV scheme and the F_c form factor, while the *bottom figure* the $1/2^-$ case with the PS scheme and the F_c form factor. Shifts for the missing mass scales, δm_1 and δm_2, were introduced in the 1.92- and 2.01-GeV/c data, respectively. The *black solid line* represents the no-shift case. The *red dashed* and *dotted lines* represent $\delta m_1 = \pm 1.5$ MeV, while the *blue dashed* and *dotted lines* represent $\delta m_2 = \pm 1.5$ MeV

limits were improved to about 1/2 from the previous limits of 0.72 and 3.1 MeV for $1/2^+$ and $1/2^-$, respectively, obtained with the 2010 data [8]. The 2010 and 2012 data have almost the same statistics, but different incident momenta. It was confirmed that the incident momentum dependence of the cross section in the theoretical calculation was more effective to improve the upper limit of the width.

The present upper limit depends on the parity of Θ^+. It is natural for the $1/2^-$ state to have a larger upper limit of the width, because the $1/2^-$ state is an *s*-wave resonance. This is a reason why the negative parity state is disfavored from a theoretical point of view, as described in Sect. 1.3. The width of 1.9 MeV is quite narrow as for an *s*-wave resonance. However, the widths reported in the DIANA and Belle experiments do not depend on the parity, and smaller than 1.9 MeV. If the Θ^+ is really a $1/2^-$ state with such a narrow width, the production cross section can be below our sensitivity on the basis of the above theoretical calculation. The present measurement is not sensitive to the $1/2^-$ state with a very narrow width, although such a state is difficult to understand theoretically.

We discuss the spin-parity of $1/2^+$ case, next. The present upper limit of 0.36 MeV is much smaller than a few MeV constrained from the past K^+d scattering data [10–14], described in Sect. 1.2. It is also more stringent than the upper limit from the Belle Collaboration, e.g., $<$0.64 MeV at 1539 MeV/c^2 [1]. The latest DIANA result is indicated with a magenta square in Fig. 5.5; they claimed that the Θ^+ was observed at 1538 ± 2 MeV/c^2 and the width is 0.34 ± 0.10 MeV [2]. The present upper limit at the 90 % C.L. for the PV-F_c case are comparable to their value. Considering that we adopted the most conservative case in the four variation, the consistency between our result and DIANA is subtle, but the present result does not completely contradict the DIANA claim. Since the present upper limit is predominantly determined by the statistics of the experimental data, several times more statistics are needed to exclude the DIANA result.

References

1. R. Mizuk et al., Belle Collaboration. Phys. Lett. B **632**, 173 (2006)
2. V.V. Barmin et al., DIANA Collaboration. Phys. Rev. C **89**, 045204 (2014)
3. T. Hyodo, A. Hosaka, M. Oka, Prog. Theor. Phys. **128**, 523 (2012)
4. K. Miwa et al., KEK-PS E559 Collaboration. Phys. Rev. C **77**, 045203 (2008)
5. S.-I. Nam, A. Hosaka, H.-C. Kim, Phys. Lett. B **579**, 43 (2004)
6. T. Hyodo (private communication)
7. F. James, MINUIT—Function minimization and error analysis, CERN-D506 (1994)
8. K. Shirotori et al., J-PARC E19 Collaboration. Phys. Rev. Lett. **109**, 132002 (2012)
9. K. Shirotori, Ph.D. thesis, Tohoku University (2011)
10. R.A. Arndt, I.I. Strakovsky, R.L. Workman, Phys. Rev. C **68**, 042201(R) (2003); **69**, 019901(E) (2004)
11. J. Haidenbauer, G. Krein, Phys. Rev. C **68**, 052201(R) (2003)
12. A. Sibirtsev, J. Haidenbauer, S. Krewald, Ulf-G. Meißner, Phys. Lett. B **599**, 230 (2004)
13. R.N. Cahn, G.H. Trilling, Phys. Rev. D **69**, 011501(R) (2004)
14. W.R. Gibbs, Phys. Rev. C **70**, 045208 (2004)

Chapter 6
Conclusion

Study of exotic hadrons, which cannot be interpreted as ordinary three-quark baryons or quark-antiquark mesons, would offer us a good opportunity to investigate low-energy quark dyanmics. The pentaquark Θ^+ has a strangeness quantum number $S = +1$ with its minimal quark configuration of $uudd\bar{s}$. The distinct features of the Θ^+ are a light mass of about 1540 MeV and a narrow width of a few MeV or less. If such an exotic pentaquark exits, it is quite interesting from a viewpoint of the hadron structure. Many experiments searched for the Θ^+ so far, but the experimental situation was still controversial. For further investigation, a high-statistics and high-resolution experiment has been required.

The differential cross section of the $\pi^- p \to K^- X$ reaction was measured in forward scattering angles to search for the Θ^+ pentaquark with the missing-mass technique. The experiment was performed in 2012 using a beam momentum of 2.01 GeV/c at the K1.8 beam line in the J-PARC hadron facility. A liquid hydrogen target with a thickness of 0.85 g/cm^2 was exposed to 8.1×10^{10} π^- beams with a typical intensity of 1.7×10^6 per 2.2-s spill. We constructed a high-resolution spectrometer system. The beam pions were measured with the beam spectrometer with a momentum resolution of 1×10^{-3} (FWHM). The outgoing kaons were identified with the SKS spectrometer with a momentum resolution of 2×10^{-3} (FWHM). We measured the missing mass of the $\pi^- p \to K^- X$ reaction at forward scattering angles of 2–15° in the laboratory frame. The missing-mass resolution for the Θ^+ was estimated to be 2.13 ± 0.15 MeV (FWHM). Using the $\Sigma^\pm$ production data and the beam-through data, the absolute scale of the missing mass for the Θ^+ production data was calibrated with an uncertainty of 1.4 MeV/c^2. Thus, it was demonstrated that we are able to observe a sharp missing-mass peak and determine the mass and, possibly, width with a good precision, if the Θ^+ is produced. The cross section was calculated by correcting the data for the experimental efficiency and acceptance with an uncertainty of 7 %. The measured differential cross sections of the $\pi^\pm p \to K^+ \Sigma^\pm$ reactions were in good agreement with the past experimental data.

No sharp peak structure was observed in the missing-mass spectrum of the $\pi^- p \to K^- X$ reaction. The missing-mass acceptance was wider than the previous 2010 data owing to the improved experimental setup. The upper limit on the Θ^+

M. Moritsu, *Search for the Pentaquark Θ^+ via the $\pi^- p \to K^- X$ Reaction at J-PARC*, Springer Theses, DOI 10.1007/978-981-10-0012-6_6

production cross section averaged over scattering angles from 2° to 15° in the laboratory frame was obtained as a function of the Θ^+ mass, and found to be less than 0.28 μb/sr at the 90 % C.L. in a mass region of 1500–1560 MeV/c^2. Note that we assumed the intrinsic width of Θ^+ is negligibly smaller than the experimental resolution. If the width of Θ^+ is 1 MeV, the above upper limit rises by 0.10 μb/sr. The systematic uncertainty of the upper limit was controlled within 10 %. Hence, the present upper limit is predominantly determined by the statistical uncertainty. The present upper limit is as small as the previous 2010 result of 0.28 μb/sr. This is attributed to almost the same statistics of the data.

The narrowness of the width is the most peculiar property to the Θ^+ pentaquark. The mechanism of the $\pi^- p \to K^- \Theta^+$ reaction was theoretically discussed using the KEK-E522 and E559 results. Knowing that the t-channel and contact term contributions are very small, the s-channel contribution is important in the $\pi^- p \to K^- \Theta^+$ reaction. Since the s-channel amplitude is related to the Θ^+ decay width through the $KN\Theta$ coupling constant, we can estimate the upper limit of the width from the cross section measured in the experiment. Using both the 2010 and 2012 data together with a theoretical calculation using the effective Lagrangian approach, the upper limit of the Θ^+ width was estimated as a function of the Θ^+ mass. Considering the theoretical uncertainty, we adopted the most conservative theoretical scheme that gives the largest upper limit. The upper limits of the width were estimated to be 0.36 and 1.9 MeV for the Θ^+ spin-parity of $1/2^+$ and $1/2^-$, respectively. The upper limits of the width were improved by half of the previous limits of 0.72 and 3.1 MeV for $1/2^+$ and $1/2^-$, respectively, obtained in the 2010 data [1]. The present upper limit of the width is not sensitive enough to the $1/2^-$ state with a very narrow width in this theoretical model. For the $1/2^+$ case, the present limit is more stringent than the upper limit of 0.64 MeV reported from the Belle Collaboration [2]. The present limit is comparable to the width of 0.34 ± 0.10 MeV reported by the DIANA Collaboration [3]. The consistency is subtle but the present result does not completely contradict the DIANA claim.

References

1. K. Shirotori et al., J-PARC E19 collaboration. Phys. Rev. Lett. **109**, 132002 (2012)
2. R. Mizuk et al., Belle collaboration. Phys. Lett. B **632**, 173 (2006)
3. V.V. Barmin et al., DIANA collaboration. Phys. Rev. C **89**, 045204 (2014)

Appendix A
AC Efficiency

The efficiency of the AC counter is described in this appendix. AC was replaced with a new large-size detector with a sensitive area of $2040^W \times 1200^H$ mm^2 before the 2012 run. The specification of the new AC counter is found in Sect. 2.4.2. AC is required to have a good efficiency of ∼99.9 % for pion veto at the trigger level.

The AC efficiency was estimated for pions with 0.8–1.2 GeV/c in the 2012 data. The position dependence of the efficiency is shown in Fig. A.1, where apparent efficiency drops are observed. In the horizontal position dependence, the drop at $X >$ 1000 mm is ascribed to an edge of the silica aerogel radiator. In the vertical position dependence, the drops at $Y = \pm 200$ mm are ascribed to 2-mm thick aluminum plates which support the stack of aerogel tiles. The 2-mm thick regions are insensitive to the Cherenkov radiation. Note that, since SKS is a horizontally bending magnet, the X-position is related to the particle momentum, whereas the Y-position is not related to the momentum. The momentum dependence of the AC efficiency is shown in Fig. A.2, where significant dependence is not observed. The efficiency drops at the Y positions does not affect the missing mass distribution. In addition, kaons are well discriminated from pions in the offline analysis using particle trajectories and time of flight, as described in Sect. 3.3.2. The inefficiency of AC is not a problem of the offline analysis but of the trigger.

The AC efficiency was 98–99 % even except for the local efficiency drops. This might be attributed to gaps among the aerogel tiles. After this experiment, the support plates were removed, and the aerogel tiles were stacked up again. The efficiency was improved to 99.7 % in a subsequent experiment [1].

M. Moritsu, *Search for the Pentaquark Θ^+ via the $\pi^- p \to K^- X$ Reaction at J-PARC*, Springer Theses, DOI 10.1007/978-981-10-0012-6

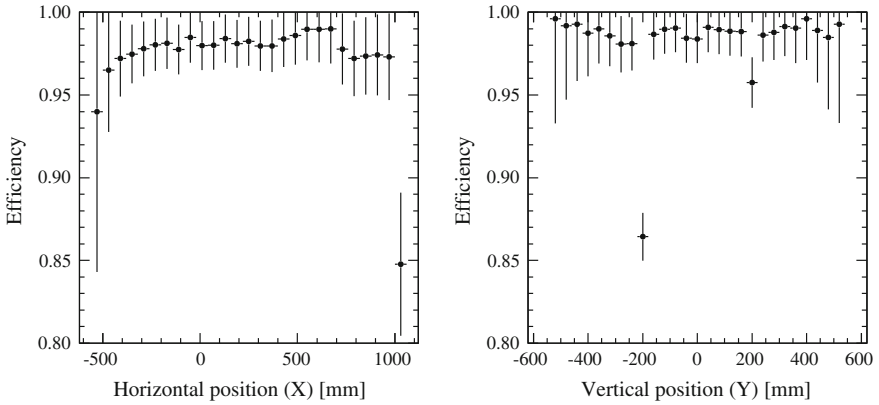

Fig. A.1 Position dependence of the AC efficiency. (*Left*) Horizontal position (X) dependence for an interval of 60 mm. (*Right*) Vertical position (Y) dependence for an interval of 40 mm

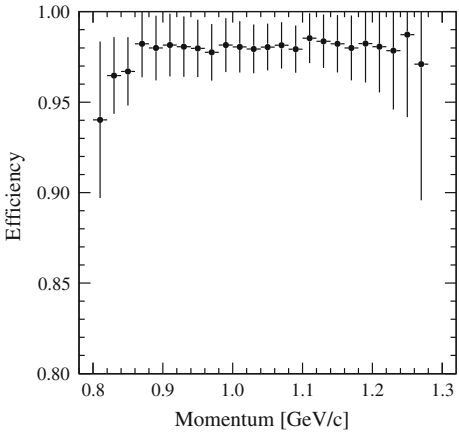

Fig. A.2 Momentum dependence of the AC efficiency for an interval of 20 MeV/c

Reference

1. R. Ota, Master Thesis (in Japanese), Osaka University, 2013

Appendix B
Miscellaneous Vertex Analyses

The analysis of the vertex reconstruction was described in Sect. 3.4. Miscellaneous vertex analyses which were not included in the main text are given in this appendix.

B.1 *Z*-Vertex Resolution

The (beam direction) z-vertex resolution was estimated using the empty target data where the scattering events at the target vessel and the vacuum chamber windows were observed. Both the end caps of the vessel and the chamber windows were made of a 0.25-mm thick mylar, which were positioned at $z = \pm 60$ and ± 135 mm. Figure B.1 shows the z-vertex distributions for different scattering angle regions in the empty target data. One can see that the z-vertex resolution deteriorates with decrease of the scattering angles. The target image could not recognize in events with the scattering angle less than 2°. Contribution from the four mylar windows are clearly identified in events with the large scattering angle. The z-vertex resolution was estimated to be 10–20 mm (σ) for the scattering angles from 2° to 15°.

B.2 *X*-Vertex Resolution

The (horizontal) x-vertex resolution was estimated in the same manner as for the z-vertex resolution. The target vessel was a cylinder with a 33.9-mm radius and the side surface was made of a 0.3-mm thick PET. Figure B.2 shows the x-vertex distribution in the empty target data. To observe contribution from the side surface

M. Moritsu, *Search for the Pentaquark Θ^+ via the $\pi^- p \to K^- X$ Reaction at J-PARC*, Springer Theses, DOI 10.1007/978-981-10-0012-6

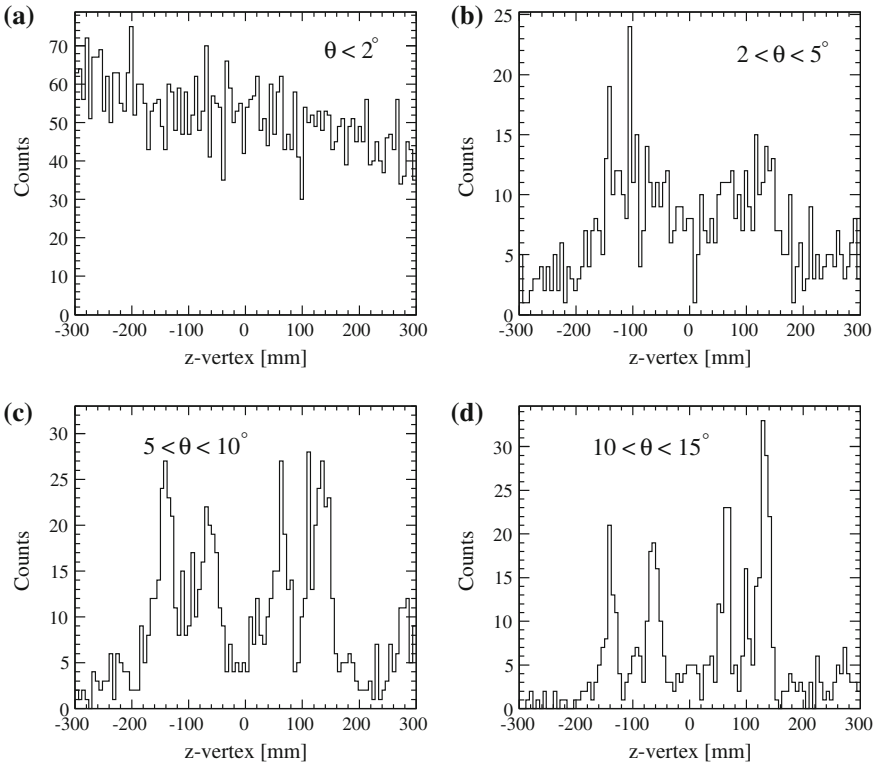

Fig. B.1 Z-vertex distributions in the empty target data. The scattering angle θ is selected as **a** $\theta < 2°$, **b** $2 < \theta < 5°$, **c** $5 < \theta < 10°$, or **d** $10 < \theta < 15°$. The mylar windows were positioned at $z = \pm 60$ and ± 135 mm

clearly, the z-vertex from -50 to 50 mm were selected. The x-vertex resolution was estimated to be 2 mm (σ) for the scattering angles from 2° to 15°.[1]

B.3 Vertex Distribution Difference Between (π^-, K^-) and (π^-, π^-) Events

As for the (π^-, K^-) reaction from a proton at 2 GeV/c, the following processes are known:

$$\pi^- p \rightarrow \phi\, n \rightarrow K^- K^+ n, \tag{B.1}$$

[1]The (vertical) y-vertex resolution could not be estimated since the beam profile at the target was a horizontally oblate shape and the beam hit neither the upside nor downside of the vessel.

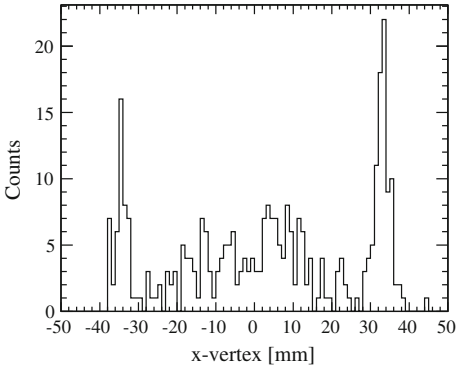

Fig. B.2 X-vertex distribution in the empty target data. Events with the scattering angles of 2–15° and the z-vertex from −50 to 50 mm are selected. The target vessel had a cylindrical shape with a 33.9-mm radius

$$\pi^- p \rightarrow \Lambda(1520)\ K^0 \rightarrow K^- K^0 p, \tag{B.2}$$

$$\pi^- p \rightarrow K^- K^+ n \text{ or } K^- K^0 p \text{ (nonresonant)}. \tag{B.3}$$

As for the (π^-, K^-) reaction from a neutron at 2 GeV/c, only one process is possible:

$$\pi^- n \rightarrow K^- K^0 n \text{ (nonresonant)}. \tag{B.4}$$

Hence, the cross section of the (π^-, K^-) reaction from a neutron is expected to be smaller than that from a proton. On the other hand, the cross section of the (π^-, π^-) reaction from a neutron is the same as that from a proton.

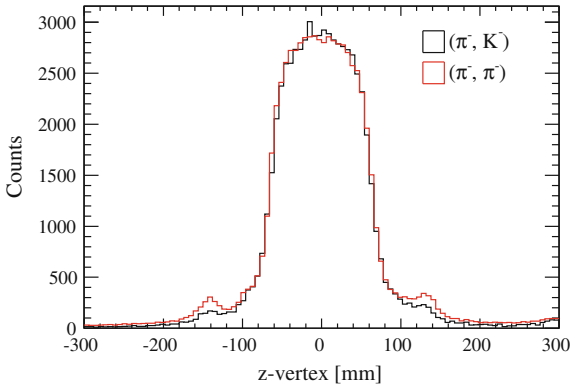

Fig. B.3 Comparison of z-vertex distributions between (π^-, K^-) and (π^-, π^-) events. The *black* histogram shows a z-vertex distribution for (π^-, K^-) events, while the *red* histogram shows that for (π^-, π^-) events normalized by the number of contribution from the LH_2 ($-60 < z < 60$ mm). Enhancements around the mylar window positions are seen in the (π^-, π^-) events

The z-vertex distribution for the (π^-, K^-) events was compared to that for the (π^-, π^-) events in Fig. B.3. The histogram for the (π^-, π^-) events was normalized by the number of contribution from the LH_2. The mylar window are composed by Hydrogen, Carbon and Oxygen; therefore, the (π^-, K^-) events from the mylar window are smaller than the (π^-, π^-) events. This is the reason why the contamination fraction estimated by using (π^-, π^-) events in Sect. 3.4 are slightly larger than that of (π^-, K^-) events.

Appendix C
Stability of Magnetic Field

C.1 Field of the Beam Spectrometer

The magnetic field of the D4 magnet was monitored by the Hall probe with the precision of 0.01 % [1]. The probe was set at 75-mm upside of the central plane of the D4 magnet. The field was recorded every 1 s during the experiment. Figure C.1 shows the magnetic field of the D4 magnet in the Θ^+ search data. The gradual fluctuation in the long-term period may be attributed to the stability of the power supply. The spikes were coincident with temporary shutdowns of the D3 and D2 magnets to enter the experimental area; therefore, they have no problem since the data acquisition was stopped at that time. The stability of the magnetic field was found to be within 2.4×10^{-4} in the whole of the period, which is small enough comparing with the beam momentum resolution. The stability in the calibration data was also investigated and found to be better than that of the Θ^+ search data.

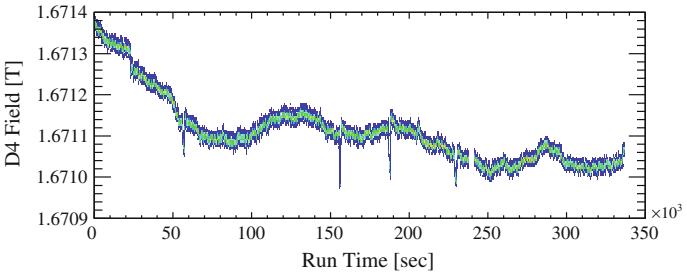

Fig. C.1 Magnetic field of the D4 magnet in the Θ^+ search data

M. Moritsu, *Search for the Pentaquark Θ^+ via the $\pi^- p \to K^- X$ Reaction at J-PARC*, Springer Theses, DOI 10.1007/978-981-10-0012-6

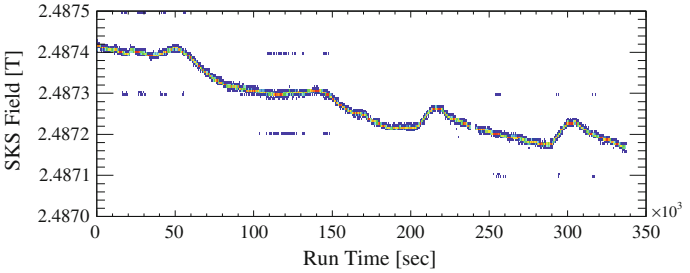

Fig. C.2 Magnetic field of the SKS magnet in the Θ^+ search data

C.2 Field of the SKS Spectrometer

The magnetic field of the SKS magnet was monitored by the NMR probe with the precision of 1 μT [2]. The probe was set on the bottom pole of the magnet. The field was recorded every 1 s during the experiment. Figure C.2 shows the magnetic field of the SKS magnet in the Θ^+ search data. The gradual fluctuation in the long-term period may be attributed to the stability of the power supply. The sudden fluctuations of ± 0.1 mT in 1 s may be caused by the readout electronics of the probe. The stability of the magnetic field was found to be within 9.6×10^{-5} in the whole of the period, which is small enough comparing with the momentum resolution for scattered particles. The stability in the calibration data was also investigated and found to be better than that of the Θ^+ search data.

References

1. Digital Teslameter 151 (DTM-151), Group3 Technology. http://www.group3technology.com/index.php/products/product/digital-teslameter-151
2. EFM-3000AX, Echo Electronics. http://echo-denshi.co.jp/nmr_magnetic.htm

Appendix D
Summary of Σ Production Cross Section

The $\Sigma^{\pm}$ production cross sections were presented in Sect. 3.9. In this appendix, the cross sections are tabulated and the cross sections in the center-of-mass (c.m.) frame are presented for convenience of other use.

Table D.1 shows the differential cross sections in the laboratory frame which were plotted in Fig. 3.27 or 3.28. Figure D.1 and Table D.2 show the differential cross sections in the c.m. frame. It should be noticed that the present Σ production cross sections have the systematic uncertainty of 6 % described in Sect. 3.8.3.

Table D.1 Differential cross sections in the laboratory frame for $\pi^+ p \to K^+ \Sigma^+$ at 1.38 GeV/c, $\pi^- p \to K^+ \Sigma^-$ at 1.38 and 1.46 GeV/c obtained in the E19-2012 data

θ_{Lab} (deg)	Σ^+ at 1.38 GeV/c		Σ^- at 1.38 GeV/c		Σ^- at 1.46 GeV/c	
	$d\sigma/d\Omega$	Error	$d\sigma/d\Omega$	Error	$d\sigma/d\Omega$	Error
3	601.0	32.0	95.7	7.4	74.7	3.1
5	452.0	22.0	83.3	5.5	63.8	2.2
7	464.0	23.0	69.8	5.2	62.3	2.3
9	289.0	19.0	60.4	5.0	47.0	2.0
11	199.0	17.0	39.9	4.8	38.0	1.9
13	143.0	17.0	37.5	5.2	20.4	1.5
15	139.0	18.0	29.9	4.9	18.0	1.8

The quoted cross sections were derived from the average between $\theta_{\mathrm{Lab}} \pm 1$ deg and are presented in a unit of μb/sr. The errors are statistical only. The data points are plotted in Fig. 3.27 or 3.28

M. Moritsu, *Search for the Pentaquark Θ^+ via the $\pi^- p \to K^- X$ Reaction at J-PARC*, Springer Theses, DOI 10.1007/978-981-10-0012-6

Table D.2 Differential cross sections in the c.m. frame for $\pi^+ p \to K^+ \Sigma^+$ at 1.38 GeV/c, $\pi^- p \to K^+ \Sigma^-$ at 1.38 and 1.46 GeV/c obtained in the E19-2012 data

$\cos\theta_{\rm cm}$	Σ^+ at 1.38 GeV/c		Σ^- at 1.38 GeV/c		Σ^- at 1.46 GeV/c	
	$d\sigma/d\Omega$	Error	$d\sigma/d\Omega$	Error	$d\sigma/d\Omega$	Error
0.975	77.6	2.4	12.75	0.56	10.50	0.24
0.925	51.4	2.6	9.56	0.66	8.35	0.29
0.875	33.3	2.9	6.64	0.77	4.98	0.27
0.825	25.1	3.2	5.95	0.88	3.79	0.32
0.775	19.2	3.2	5.97	1.05	2.77	0.35

The quoted cross sections were derived from the average between $\cos\theta_{\rm cm} \pm 0.025$ and are presented in a unit of μb/sr. The errors are statistical only. The data points are plotted in Fig. D.1

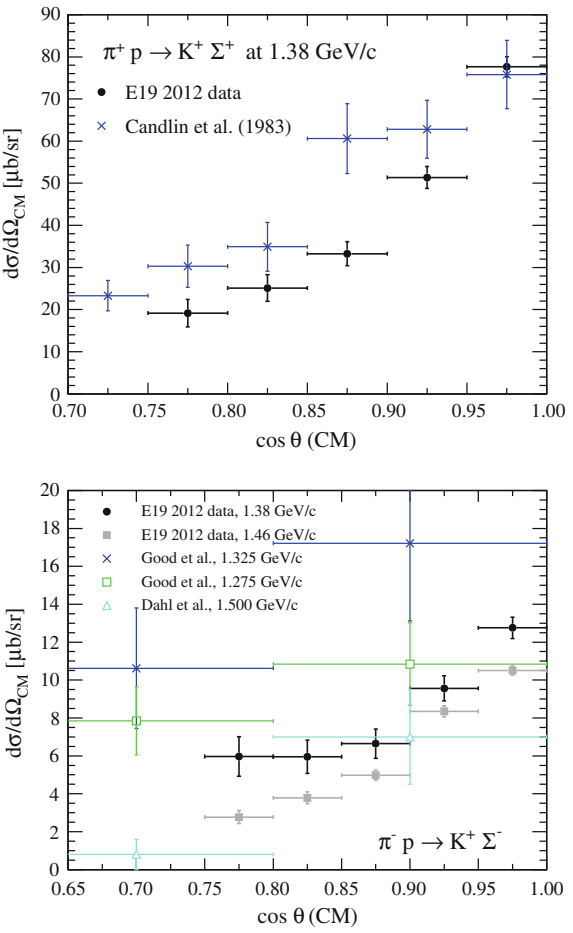

Fig. D.1 (*Top*) Differential cross sections in the c.m. frame for the $\pi^+ p \to K^+ \Sigma^+$ reaction. The *black solid circles* are the present E19-2012 data at 1.38 GeV/c. The *blue crosses* are the data from Candlin et al. [1] at 1.377 GeV/c. (*Bottom*) Differential cross sections in the c.m. frame for the $\pi^- p \to K^+ \Sigma^-$ reaction. The *black solid circles* and the *gray solid squares* are the present E19-2012 data at 1.38 and 1.46 GeV/c, respectively. The *blue crosses* and the *green open squares* are the data from Good et al. [2] at 1.325 and 1.275 GeV/c, respectively. The *cyan open triangles* are the data from Dahl et al. [3] at 1.500 GeV/c. The scattering angle is defined as the one between the outgoing kaon and the incoming pion. The quoted errors are statistical only. The present data are tabulated in Table D.2

References

1. D.J. Candlin et al., Nucl. Phys. B **226**, 1 (1983)
2. M.L. Good, R.R. Kofler, Phys. Rev. **183**, 1142 (1969)
3. O.I. Dahl et al., Phys. Rev. **163**, 1430 (1967)

Appendix E
Additional Study of Background Processes

The background processes associated with the Θ^+ production in the $\pi^- p \to K^- X$ reaction were discussed in Sect. 4.2, where only the three reactions (4.1–4.3) were considered. In this appendix, other higher excited Λ^* and Σ^* resonances, which were neglected in the main text, are reconsidered.

In addition to the reactions (4.1–4.3), following reactions potentially contribute to the background:

$$\pi^- p \to Y^{*-} K^+ \to K^- K^+ n, \tag{E.1}$$
$$\pi^- p \to Y^{*0} K^0 \to K^- K^0 p, \tag{E.2}$$

where Y^* represents Λ^* or Σ^* resonances above the $\bar{K}N$ threshold except for $\Lambda(1520)$. The beam momentum of 2.01 GeV/c in the present experiment corresponds to the total c.m. energy of 2164 MeV, which is near the production threshold of $\Lambda(1600, 1670, 1690)$ and $\Sigma(1660, 1670)$. These Y^* resonances are summarized in Table E.1.

Figure E.1 shows simulated missing mass spectra of the $\pi^- p \to K^- X$ reaction for the background reactions (E.1 and E.2). Since the angular distributions of the production and decay of the Y^*s are not known, an isotropic distribution was assumed

Table E.1 Λ^* and Σ^* resonances which potentially contribute to the background [1]

Particle	J^P	Γ (MeV)	Status
$\Lambda(1600)$	$1/2^+$	150	***
$\Sigma(1660)$	$1/2^+$	100	***
$\Lambda(1670)$	$1/2^-$	35	****
$\Sigma(1670)$	$3/2^-$	60	****
$\Lambda(1690)$	$3/2^-$	60	****

Unestablished resonances with a status of * or ** are neglected ($\Sigma(1480, 1560, 1580, 1620)$ are reported as resonances with * or ** status in [1])

M. Moritsu, *Search for the Pentaquark Θ^+ via the $\pi^- p \to K^- X$ Reaction at J-PARC*, Springer Theses, DOI 10.1007/978-981-10-0012-6

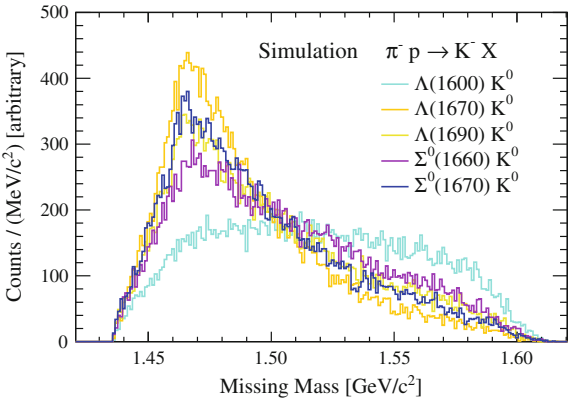

Fig. E.1 Simulated missing mass spectra of the $\pi^- p \to K^- X$ reaction for the background reactions (E.1 and E.2). The angular distributions of the production and decay of all the Y^*s are assumed to be isotropic. The production cross section of all the Y^*s are assumed to be the same

in the simulation. The Y^* resonances contribute to the relatively low mass region. The $\Lambda(1670, 1690)$ and $\Sigma(1660, 1670)$ contributions make similar spectrum shapes.

These Y^* resonances were not observed in Ref. [2]. Considering that ϕ and $\Lambda(1520)$ were clearly identified in their data, the Y^* resonances are expected to have smaller cross sections than ϕ or $\Lambda(1520)$. Figure E.2 shows simulated missing mass spectra of the $\pi^- p \to K^- X$ reaction including the $\Lambda(1600)$ and $\Lambda(1670)$ contributions in addition to (4.1–4.3). The $\Lambda(1670)$ represents an unified contribution of $\Lambda(1670, 1690)$ and $\Sigma(1660, 1670)$ because of the similar spectrum shapes. Both cross sections of $\Lambda(1600)$ and $\Lambda(1670)$ were assumed to be a half of $\Lambda(1520)$ and the scale of the nonresonant $\bar{K}KN$ was normalized to the experimental data. The overall spectrum shape are in better agreement with the present data than Fig. 4.2, owing to the Y^* contributions to the low mass region.

As discussed above, the Y^* contributions have a possibility to reproduce the spectrum shape better. However, as long as the cross sections and the angular distributions for the Y^*s are not known, we can not make a definite statement from the present data. Finally, it should be noted that the reproducibility of the overall spectrum shape is not directly related to the conclusion, because polynomial functions in 1500–1560 MeV/c^2 were used as the background shape in the upper limit estimation.

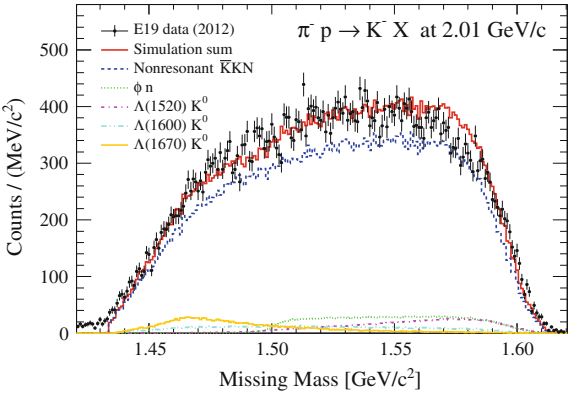

Fig. E.2 Missing mass spectrum of the $\pi^- p \to K^- X$ reaction at 2.01 GeV/c. The experimental data are indicated by the *black points* with statistical errors. The *red* histogram represents the total background shape obtained by the MC simulation including five processes: nonresonant $\bar{K}KN$ (*blue dashed*), ϕ (*green dotted*), $\Lambda(1520)$ (*magenta dashed-dotted*), $\Lambda(1600)$ (*cyan dashed-two-dotted*) and $\Lambda(1670)$ (*orange dashed-three-dotted*). Both cross sections of $\Lambda(1600)$ and $\Lambda(1670)$ were assumed to be a half of $\Lambda(1520)$. The scale of the nonresonant components was normalized to the experimental data

References

1. J. Beringer et al. (Particle Data Group), Phys. Rev. D **86**, 010001 (2012)
2. O.I. Dahl et al., Phys. Rev. **163**, 1377 (1967)

Curriculum Vitae

Manabu Moritsu
Current affiliation address:
Department of Physics, Osaka University
1-1, Machikaneyama-cho, Toyonaka, Osaka 560-0043, Japan
e-mail: moritsu@kuno-g.phys.sci.osaka-u.ac.jp
Web: http://www-kuno.phys.sci.osaka-u.ac.jp/en/index.html

Appointments

- Specially Appointed Assistant Professor, Department of Physics, Osaka University (Feb. 2015–)
- Collaborative Researcher, Research Center for Nuclear Physics, Osaka University (Apr 2014–Jan 2015)
- Research Assistant, Research Center for Nuclear Physics, Osaka University (Apr 2013–Mar 2014)
- JSPS Research Fellow (DC2) (Apr 2010–Mar 2013)

Education

- Doctor of Philosophy (Ph.D.) in Physics, Kyoto University (2009–2013), advisor Prof. Tomofumi Nagae
- Master of Science (MSc) in Physics, Kyoto University (2007–2009)
- Bachelor of Sciences in Physics, Kyoto University (2003–2007)

Research Statement

My research in this thesis aims to explore deep understanding of the Strong Interaction in hadrons by searching for exotic hadrons. The work had been accomplished with both elaborative analysis and construction of our new experimental instruments in the new facility, J-PARC.

My recent interest is to explore physics beyond the Standard Model of elementary particles, especially by using a lepton-flavor-violating muon decay.

M. Moritsu, *Search for the Pentaquark Θ^+ via the $\pi^- p \to K^- X$ Reaction at J-PARC*, Springer Theses, DOI 10.1007/978-981-10-0012-6